



TECHNISCHE
UNIVERSITÄT
WIEN
Vienna | Austria

Dissertation

Modelling Deposit Formation in Automotive SCR Systems

A Thesis Submitted in Partial Fulfillment of the Requirements for the Degree of
Doktor der Technischen Wissenschaften under the Direction of

Assoc. Prof. Dr. Thomas Lauer

Institute for Powertrains & Automotive Technology E315

and

Univ. Prof. Dr. Franz Winter

Institute of Chemical Engineering E166

submitted to the Vienna University of Technology
Faculty of Mechanical and Industrial Engineering

by

Dipl.-Ing. Univ. Henrik Smith

Matriculation Number 1128774
Ungargasse 25/2/13, 1030 Wien

Copyright Notice

This work uses the font **Utopia**[®], which has been released by *Adobe* for the usage by the *TeX Users Group (TUG)* and is subject to copyright. The mathematical typeset is provided by the *Comprehensive TeX Archive Network (CTAN)* in the form of the **Fourier-GUTenberg** package.

Copyright 1989, 1991 Adobe Systems Incorporated. All rights reserved.

Utopia[®]

Utopia is either a registered trademark or trademark of Adobe Systems Incorporated in the United States and/or other countries. Used under license.

Acknowledgements

The present work was conducted during my employment as a university assistant at the Institute for Powertrains and Automotive Technology at the Vienna University of Technology.

I would like to thank the head of the institute, Univ. Prof. Dr. Bernhard Geringer, for providing an environment which allowed great autonomy to realise own ideas and concepts, and for the opportunity to carry out experimental work at the test bench. I would also like to thank the head of the simulation group, Assoc. Prof. Dr. Thomas Lauer, for providing an interesting and challenging topic, his support, and the supervision of this work. Moreover, I would like to gratefully mention Univ. Prof. Dr. Franz Winter for taking an interest in the subject and for agreeing to act as a second examiner of this thesis.

I would like to express my sincere gratitude to my all of my colleagues at the institute for the wonderful working atmosphere and the great collegiality. I would particularly like to thank Markus Zöchbauer, Michael Heiß and Werner Holly for the enjoyable time at the office. The great mutual support, even during tough times during our PhD studies, is what made work fun and built friendships. I am especially grateful for the friendly collaboration with Markus, for the continuous and constructive debates, for the constant review and feedback on presentations, papers and my thesis. Your encouragement and steady support is what had the greatest influence on my time at the institute.

I would also like to thank our predecessor in the SCR department, Simon Fischer, for sharing his enormous experience with us, and our colleagues from the test bench, in particular René Bitto and Thomas Hofherr, for their great support in the laboratory. Moreover, I would like to gratefully mention our industry partners and in particular our contact persons, Dr. Steven Pierson (Jaguar Land Rover Limited), DI Christian Krenn (BMW Motoren GmbH) and Dr. Robert Fromm (Continental Automotive GmbH), for the kind collaboration and their support of our publications. Finally, sincere thanks go to Dr. Sarah Meyer (Institute for Materials Chemistry) and Ing. Josef Beiglböck (Zentraler Informatikdienst) for their support.

Meinen Eltern möchte ich für die stetige moralische Unterstützung und den Rückhalt in allen Lebenslagen danken. Das große Vertrauen, das sie mir entgegen gebracht haben, und die Freiheit, meinen eigenen Weg einschlagen zu können, sind nicht selbstverständlich. Ein ganz besonderer Dank gilt außerdem meiner Freundin Steffi, die mir in allen Phasen dieser Arbeit zur Seite stand – für die Geduld, ihr Verständnis und ihre Unterstützung. Auch sie haben damit ganz wesentlich zu dieser Arbeit beigetragen.

Vienna, August 2016

Henrik Smith

Abstract

Exhaust aftertreatment systems based on selective catalytic reduction (SCR) have been introduced on a broad scale to cope with nitrogen oxides (NO_x) emissions of diesel engines and to comply with emission legislation. In automotive SCR applications urea water solution (UWS) has been established as a carrier substance for the reducing agent ammonia, the preparation of which happens in the form of a multi-stage decomposition process. However, during decomposition urea may undergo a number of undesired secondary reactions, leading to the formation of solid deposits. In order to ensure robustness of SCR system designs against deposit formation, a profound knowledge of the underlying mechanisms is an imperative. In addition, efficient SCR system design calls for a method that allows to predict the deposit formation risk in the early design stages. The present work demonstrates the mechanisms of deposit formation and provides a methodology for the numerical assessment of the deposit formation risk with computational fluid dynamics (CFD).

Wall wetting was confirmed as a precursor of deposit formation. As primary impingement targets mixing elements show a high risk of deposit formation and therefore were put into the focus of this work. The critical injection rate, i.e. the maximum UWS mass the system was able to decompose without residue, increased exponentially with the mixing element temperature level. The consecutive steps of deposit formation were wall wetting, liquid film accumulation, deposit nucleus formation, and deposit accumulation. In areas of initial wall wetting continuous dilution and intense mixing of the film effectively impeded deposition regardless of the temperature. However, as soon as the film left these areas deposit formation had to be expected. Deposition was impeded only locally if wall films trickled with high velocities and/or were particularly thick, e.g. in areas of accumulation. Wall film was extensively distributed at geometric inconsistencies, such as edges, holes, or blade joints. Most frequently, deposits formed at rear blade edges. Once a deposit nucleus had formed it could act as a starting point for further deposit accumulation both at its upstream and peripheral borders. Deposits formed over a wide range of operating conditions corresponding to mixer temperatures in the range 180...310 °C. The deposition temperature rose with the exhaust enthalpy flux and laid within a narrow temperature band. The area of solidification was determined by the balance between exhaust enthalpy flux and injection rate without altering the general liquid film pathways. Solidification occurred rapidly and deposits grew especially fast if the temperature level exceeded 290 °C. Deposits formed up to a temperature of 250 °C maintained a low and constant amount of temperature-stable components. Above 250 °C their fraction increased with temperature. Systematic decomposition experiments showed that the former required a moderate temperature increase to at least 350 °C whereas the latter needed temperatures exceeding 600 °C (DPF regeneration) to decompose fast.

The evolution of the wall film pathways on the mixing element was simulated using a validated CFD model. Based on the experimental results a model was derived to assess the local deposit formation risk based on the interpretation of the combined impact of wall film pathways, impingement, wall film dynamics, thickness, velocity, and temperature level together with the local urea and HNCO concentration. Similarity principles were applied to lower the timescales of solid cooling. The model can predict the deposit formation risk as a function of the operating conditions and of fundamental design features, such as spray and mixing element geometry. The presented methodology can easily be implemented as an extension of state-of-the-art simulations of the ammonia homogenisation in realistic SCR system geometries.

Kurzfassung

Zur Absenkung der Stickoxidemissionen von Dieselmotoren und um die gesetzlich festgelegten Emissionsgrenzen einzuhalten, wurden in den vergangenen Jahren Abgasnachbehandlungssysteme auf Basis der SCR-Technologie (Selektive Katalytische Reduktion) eingeführt. Im Bereich automobiler Anwendungen hat sich die Verwendung einer Harnstoff-Wasser-Lösung (HWL) als Trägersubstanz für das Reduktionsmittel Ammoniak bewährt. Die Aufbereitung der HWL läuft im Rahmen eines mehrstufigen Zersetzungsprozesses ab. Während der Zersetzung des Harnstoffs können jedoch eine Reihe unerwünschter Sekundärreaktionen auftreten, die in der Folge zur Bildung fester Ablagerungen führen. Um sicherzustellen, dass Systeme nicht zur Bildung von Ablagerungen neigen, ist es notwendig ein Verständnis über die zugrundeliegenden Mechanismen aufzubauen. Darüber hinaus trägt die Verfügbarkeit von Methoden, die die Vorhersage von Ablagerungsbildung bereits in einem frühen Stadium des Entwicklungsprozesses ermöglichen, sehr zu einer effizienten Systemauslegung bei. Die vorliegende Arbeit zeigt die Mechanismen der Ablagerungsbildung auf und beschreibt eine Methode, um das Ablagerungsrisiko mit Hilfe numerischer Strömungssimulation (CFD) beurteilen zu können.

Die Ergebnisse bestätigen, dass Wandfilm ein Vorläufer von Ablagerungsbildung ist. In der vorliegenden Arbeit wurde ein besonderes Augenmerk auf die Untersuchung von Mischelementen gelegt, da diese als primäres Tropfenaufprallziel einem hohen Risiko für Ablagerungsbildung ausgesetzt sind. Die kritische Injektionsmenge, d.h. die maximale HWL-Menge, die vom System rückstandsfrei aufbereitet werden konnte, stieg mit steigender Mischertemperatur exponentiell an. Die aufeinanderfolgenden Schritte der Ablagerungsbildung waren Wandfilmbildung, Wandfilmmakkumulation, Ablagerungskeimbildung und Ablagerungsakkumulation. Auf Flächen, die bereits beim ersten Tropfenaufprall benetzt wurden, wurde die Bildung von Ablagerungen durch kontinuierliche Verdünnung und intensive Durchmischung des Films unabhängig von der Temperatur verhindert. Sobald der Film diese Bereiche jedoch verließ, musste mit der Bildung von Ablagerungen gerechnet werden. Wenn der Wandfilm mit hoher Geschwindigkeit rann und/oder besonders dick war, dann verhinderte dies lokal die Ablagerungsbildung. An geometrischen Störungen, wie z.B. Kanten, Löchern oder Schaufelverbindungen, kam es zu einer starken Verteilung des Wandfilms. Ablagerungen bildeten sich in der Regel ausgehend von Schaufelhinterkanten. Sobald sich ein Ablagerungskeim gebildet hatte, konnte es sowohl stromaufwärts, als auch an seinen seitlichen Rändern zu einer weiteren Akkumulation kommen. Ablagerungen bildeten sich über einen weiten Bereich von Betriebsbedingungen, entsprechend Mischertemperaturen im Bereich 180...310 °C. Der genaue Ablagerungsort ergab sich aus der Balance zwischen Abgasenthalpiestrom und Injektionsrate, ohne dass sich dabei die grundsätzlichen Flüssigfilmpfade veränderten. Wenn das Temperaturniveau 290 °C überschritt, kam es rasch zur Solidifikation des Wandfilms und gebildete Ablagerungen wuchsen besonders schnell. Ablagerungen, die bei Temperaturen von bis zu 250 °C gebildet wurden, enthielten einen konstant niedrigen Anteil von temperaturstabilen Komponenten. Oberhalb von 250 °C stieg deren Anteil mit der Temperatur an. Systematische Zersetzungsexperimente zeigten, dass erstere einen moderaten Temperatursprung auf mindestens 350 °C benötigten, während letztere Temperaturen oberhalb von 600 °C (DPF Regeneration) benötigten, um sich schnell zu zersetzen.

Die Ausbildung der Wandfilmpfade auf dem Mischelement wurde mit Hilfe eines validierten CFD-Modells simuliert. Auf Basis der experimentellen Ergebnisse wurde ein Modell abgeleitet, mit dem das lokale Ablagerungsrisiko bewertet werden kann. Um das Risiko zu bestimmen, wurden sowohl Wandfilmpfade, als auch Tropfenaufprall, Wandfilmdynamik, -dicke, -geschwindigkeit und -temperaturniveau, als auch die lokalen Harnstoff- und HNCO-Konzentration miteinbezogen. Die Zeitskalen der Wandkühlung wurden mit Hilfe von Ähnlichkeitsprinzipien reduziert. Das Modell ist in der Lage das Ablagerungsrisiko als Funktion der Betriebsbedingungen sowie in Abhängigkeit von grundsätzlichen Designmerkmalen, wie dem Spray und der Mischergeometrie, vorherzusagen. Die vorgestellte Methodik kann als Erweiterung von Ammoniak-Gleichverteilungsberechnungen implementiert werden und eignet sich zur Simulation realistischer SCR-Systemgeometrien.

Contents

1	Introduction	1
2	Literature Review	5
2.1	Impact of Operation and Design on Deposit Formation	5
2.1.1	Operating Conditions and System Insulation	6
2.1.2	System Layout and Doser Integration	7
2.1.3	Mixing Element Design	9
2.1.4	Mixing Section Design	10
2.1.5	Spray and Doser Characteristics	11
2.2	Chemistry and Physics of Deposit Formation	14
2.2.1	Urea Decomposition Pathways	14
2.2.2	Boundary Conditions and Catalysis	19
2.2.3	Fluid Film and Crystallisation	21
2.3	Prediction of Deposit Formation	24
2.3.1	Reaction Kinetics Modelling	24
2.3.2	CFD based Modelling Approaches	25
3	Research Objectives	29
4	Analysis Methodology	31
4.1	Experimental Setups and Procedures	31
4.1.1	Test Bench Setups and Equipment	31
4.1.2	Series Exhaust Systems	32
4.1.3	Surrogate Mixing Element Geometry	34
4.1.4	Deposit Content and Decomposition	37
4.2	Simulation Models and Procedures	38
4.2.1	Numerical Framework	38
4.2.2	Gaseous Phase	40
4.2.3	Liquid Phase	41
4.2.4	Solid Walls	48
5	Mechanisms of Deposit Formation	49
5.1	Deposit Formation in a Series SCR System	49
5.2	Deposit Formation on Mixer Blades	52
5.2.1	Wall Film Transport and Deposition	52
5.2.2	Deposit Growth and Prevention	56
5.3	Deposit Formation Boundaries and Conditions	58
5.3.1	Deposition Limit	58
5.3.2	Solidification Conditions	59
5.3.3	Solidification Timescales	62
5.3.4	Deposit Accumulation	63
5.4	Deposit Content and Decomposition	63
5.4.1	Chemical Content Analysis	64

5.4.2	Decomposition Behaviour	66
5.5	Deposit Severity	66
6	Modelling Deposit Formation	69
6.1	Modelling Concept	69
6.2	Assessment of the Deposit Formation Risk	70
6.2.1	Identification of Potential Deposit Locations	70
6.2.2	Analysis of the Wall Film Dynamics	72
6.2.3	Evaluation of the Deposit Formation Risk	74
6.2.4	Acceleration of Solid Cooling	78
6.3	Validation of the Prediction Methodology	80
6.3.1	Exhaust Temperature	80
6.3.2	Injection Rate	83
6.3.3	Mixing Element and Spray	84
7	Summary and Conclusions	89
	Bibliography	93
	Nomenclature	103
	List of Figures	107
	List of Tables	109
	Curriculum Vitae	111

Chapter 1

Introduction

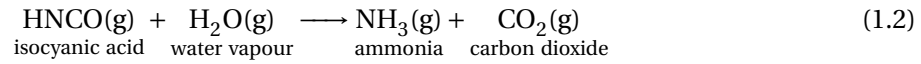
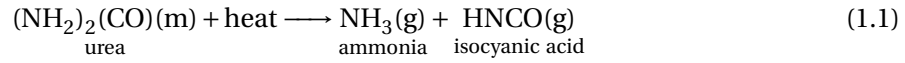
Diesel engines continue to dominate the worldwide market for light and heavy duty commercial vehicles as well as for off-road and marine applications. In Europe they have also found widespread acceptance among passenger car customers. This is reflected for example in the market share of newly registered, diesel powered passenger car vehicles, which on average exceeded 50 % in Western Europe during the past decade [1].

Theoretically, ideal combustion of (sulphur-free) diesel fuel yields carbon dioxide (CO_2) and water (H_2O) as reaction products. However, as a consequence of the imperfection of real combustion processes, undesired by-products are generated. Among these are unburned hydrocarbons (HC), carbon monoxide (CO), nitrogen oxides (NO_x), and particulate matter (PM). The latter can be significantly reduced with the application of a diesel particulate filter (DPF). In order to cope with HC and CO emissions, a diesel oxidation catalyst (DOC) is used. Unfortunately, the availability of excess oxygen in the diesel exhaust impedes the use of three-way-catalytic converters, as applied in gasoline fuelled SI engines. Therefore, a number of engine-based measures were implemented, such as exhaust gas recirculation (EGR), high pressure injection, and multiple injection techniques. In addition, exhaust aftertreatment systems, such as lean- NO_x traps (LNT) or the urea-based selective catalytic reduction (SCR or urea-SCR), have been developed [2–4]. It is widely recognised that NO_x emissions impose a considerable risk for human health and for the environment. Therefore, legislative emission standards are continuously tightened in and outside of Europe [5–7]. Initially, engine-based measures were sufficient to meet these emission requirements. When Euro IV and Euro V became applicable in Europe, urea-based SCR systems were introduced on a broad scale in the heavy-duty sector. Euro 5 and 6 made the use of exhaust aftertreatment technologies in the light-duty sector a necessity. However, since cost and packaging constraints limit the profitability of LNT systems to small diesel engines, urea-based SCR systems or combinations of LNT and SCR systems have become the standard solution to cope with NO_x emissions [4, 8–11].

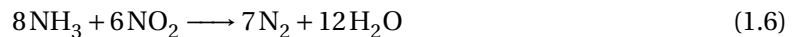
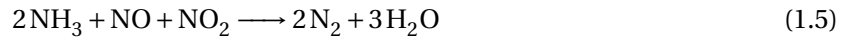
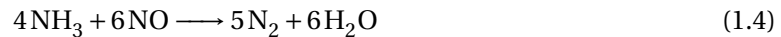
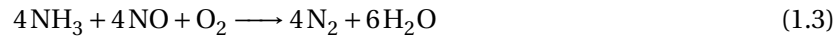
The reduction of nitrogen oxides using selective catalytic reduction has been available for commercial use for decades. In the stationary sector gaseous ammonia is used as a reductant [8, 12]. However, the transport of gaseous or liquefied NH_3 is not feasible for mobile applications due to its high toxicity [13]. Hence, the use of a 32.5 wt % urea water solution (UWS)¹ as a carrier substance has been established for automotive SCR applications. UWS preparation proceeds in the form of a multi-stage decomposition process. Initially, the water content is evaporated. At temperatures above 133 °C, urea melts and decomposes into equal amounts of gaseous ammonia and isocyanic acid in a thermolysis

¹Commercial names for UWS include AdBlue and DEF (diesel exhaust fluid).

reaction, Eq. (1.1) [14–18]. Isocyanic acid is fairly stable in the gaseous phase but can easily be converted into ammonia on typical SCR catalysts in a hydrolysis reaction, Eq. (1.2) [19].



In the SCR catalyst and under the presence of ammonia the nitrogen oxides are converted into elementary nitrogen and water, Eqs. (1.3)-(1.6) [20–22]. The overall conversion rate is highly dependent on the actual NO_2/NO ratio: while an equimolar ratio is considered optimal, excess amounts of NO_2 may even promote undesired side reactions leading to the formation of nitrous oxide (N_2O) [23]. In addition, the temperature-dependency of UWS preparation, catalytic activity including light-off, and the NH_3 storage behaviour affect the conversion efficiency and call for sophisticated control strategies [9, 20, 24–26]. Evidently, the reduction of nitrogen oxides is subject to a complex interaction between physical and chemical processes in the DOC, mixing section and the SCR catalyst. Aside from the selection of appropriate catalyst formulations and control strategies, it is therefore necessary to achieve fast and reliable urea decomposition and ammonia homogenisation in the mixing section.



The major steps of UWS preparation are illustrated in Fig. 1.1. Urea water solution is injected into the hot exhaust upstream the SCR catalyst. Primary breakup yields a polydisperse spray which then interacts with the exhaust flow and the hot system walls. Droplet wall interaction provokes the formation of wall film and/or secondary droplets. In a first step, water evaporates from the liquid phase. Subsequently, urea melts, evaporates and decomposes into ammonia and isocyanic acid in a thermolysis reaction, Eq. (1.1). The produced vaporous and gaseous species are then mixed with the exhaust by convective and diffusive transport processes. Isocyanic acid is rapidly hydrolysed in the SCR catalyst, Eq. (1.2), and the nitrogen oxides are reduced to elementary nitrogen and water vapour, Eqs. (1.3)-(1.6). Typically, mixing elements are employed as a primary impingement target in order to enhance the preparation process [27–29]. Apart from promoting droplet breakup effects, mixers absorb exhaust enthalpy more efficiently than outer system walls [30], which is what raises their temperature level and accelerates liquid film evaporation. Moreover, the diversion of the exhaust flow and the increase of the turbulence level promote convective and turbulent species mixing [31, 32].

During decomposition urea may undergo a number of undesired secondary reactions leading to the formation of solid deposits. Such deposits have been found in virtually any location between the point of injection and the SCR catalyst [16, 30, 33–39]. Their formation and accumulation is undesirable for a number of obvious reasons: ammonia cannot readily participate in the NO_x reduction process if stored into urea-based deposits, liquid, or crystallised urea [20, 29, 40, 41]. Reducing agent which has been stored may be uncontrolledly released during temperature sweeps, which renders precise system control impossible and results in NH_3 slip [40]. Furthermore, deposit formation on the injector can alter spray characteristics and targeting. In a similar way, the modification of system surfaces through the deposition of urea decomposition residue may affect UWS preparation and thus deteriorate the ammonia homogenisation performance. In addition, deposits on the SCR catalyst, pipe walls, or the mixing element will reduce the cross section and hence increase the engine backpressure, which in turn lowers engine efficiency and emissions performance [30]. Equally, block-

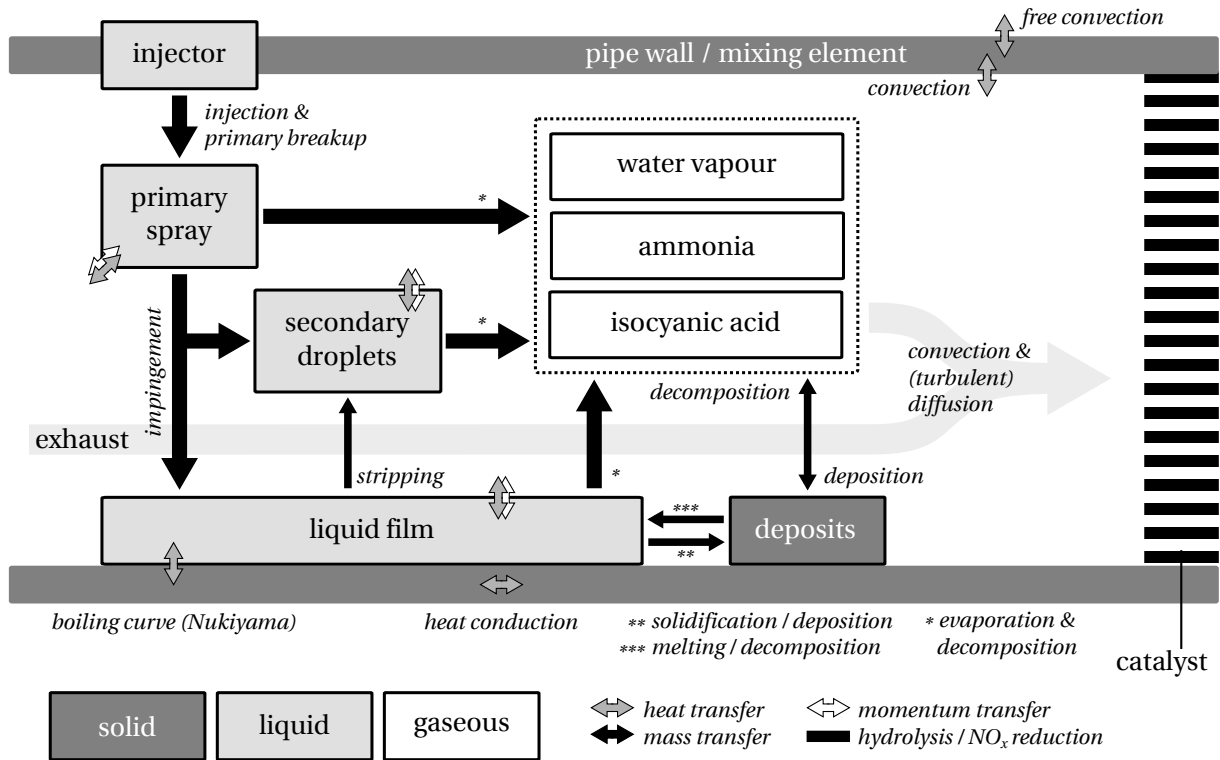


Figure 1.1: Schematic overview of the major UWS preparation steps. Adapted from Fischer [32].

age or misuse of active catalyst surface reduces the area available for NO_x reduction and NH_3 storage [20, 42, 43], increases the risk for ammonia slip, and may cause material deterioration, in particular washcoat loss [40], which may lead to a decrease of the catalyst lifetime [43]. All effects described above eventually cause a higher NO_x output, either by increasing the emissions level or by compromising the conversion efficiency of the catalyst. Moreover, system blockage resulting from deposit accumulation can lead to engine failure [44] and waste of the reducing agent may trigger early service events [37].

Despite the fact that SCR systems have been successfully applied in diesel exhaust aftertreatment, their design remains a major challenge. Increasingly tightened emission legislations put high requirements on the NO_x reduction performance of future SCR systems. At the same time, it is necessary to minimise UWS consumption while maximising system reliability in order to maintain customer acceptance. In order to ensure robustness of SCR system designs against deposit formation, a profound knowledge of the underlying mechanisms is an imperative. A number of questions arise: first, under which circumstances are deposits formed? Second, what are the relevant impact factors? Third, how can the formation of urea-based deposits be prevented? Fourth, which kinds of deposits are critical with respect to reliable system operation, if deposit formation cannot completely be prevented? In addition, efficient SCR system design calls for a method that allows to predict the deposit formation risk in the early stages of the design process.

In the present work, a detailed literature study was conducted with a focus on the impact of SCR system design on deposit formation as well as the chemistry and physics of urea decomposition. A review of available modelling approaches concluded the survey. In a first step, the formation of solid deposits was examined on a series exhaust system to determine crucial deposition locations under common conditions. Subsequently, deposit formation and accumulation were studied under a wide range of operating conditions in order to gain a deeper understanding of the mechanisms which provoke or prevent deposition. The deposit content and the decomposition behaviour of individual components

were analysed in order to determine their temperature-stability. Eventually, the data was combined to assess the severity of the individual deposits with respect to their impact on reliable system operation. In a second step, the evolution of wall film pathways was simulated using an existing CFD model for the prediction of ammonia homogenisation, as proposed by Fischer [32] and extended by Smith et al. [45]. Using the experimental and literature data a model was derived which assesses the deposit formation risk based on the properties of the simulated wall film. Finally, the ability of the model to accurately predict the risk of deposit formation was verified with measurement data.

Chapter 2

Literature Review

The impact of individual design parameters on deposit formation is well understood. Despite this, a major problem lays in the limited transferability of these findings from one setup to another. The complex interaction of the involved components and the strong dependency on the operating and boundary conditions renders the derivation of universal relationships difficult. This literature review aims at clarifying the dependency of deposit formation in SCR systems on temperature and design aspects, such as system layout and insulation, mixing element and mixing section design as well as doser integration and characteristics. Relevant works are reviewed and the uncertainties are identified. Furthermore, this literature review sheds light on the complex chemical and physical processes involved in deposit formation, including the pathways of urea decomposition, their dependency on the boundary conditions, and the most important deposit components as well as the formation of fluid film as a precursor of deposit formation. Finally, a survey is conducted on available methods for the prediction of deposit formation, which includes a discussion of both applicability and limitations of approaches based on reaction kinetics and CFD.

2.1 Impact of Operation and Design on Deposit Formation

Various works consistently reported deposits at the injector tip and inside the injector dome, on the mixing element and pipe walls as well as down to the catalyst inlet cone and frontal surface [16, 30, 33–37]. These results prove that deposit formation may occur in virtually any location between the point of injection and the SCR catalyst. The process of deposit formation is affected by a multitude of influence factors, which can be categorised as follows [30, 37]:

- **thermal and flow-related factors**, such as flow field, heat transport, temperature level, system insulation, ambient conditions as well as deposit formation chemistry
- **geometry-related factors**, such as exhaust pipe design, injector dome geometry, mixer type, orientation and location as well as SCR catalyst inlet geometry
- **engine-related factors**, such as operating conditions and raw emissions
- **injector-related factors**, such as spray characteristics and production quality
- **control-related factors**, such as dosing strategy, injection pulse width and frequency

The influence of single parameters is often measured based on the amount of generated deposits. In order to quantify the severity of deposit formation, Strots et al. [34] introduced the *deposit yield*

$$\eta_d = \frac{m_d}{32.5 \% t_{UWS} \dot{m}_{UWS}} \quad (2.1)$$

where m_d represents the deposit weight, t_{UWS} the dosing time and \dot{m}_{UWS} the UWS injection rate. It describes the fraction of the injected urea that is converted into deposits.

2.1.1 Operating Conditions and System Insulation

Strots et al. [34] investigated the influence of temperature and injection rate on deposit formation, based on experiments with a heavy-duty SCR system. The authors varied one parameter at a time while maintaining all other boundary conditions constant. An increase of the exhaust or ambient temperature reduced the deposit yield significantly, Fig. 2.1 (columns 1 and 2). Raising the injection rate promoted deposit formation at all temperatures. As expected, the tolerance against high injection rates was much more pronounced at elevated exhaust temperatures, Fig. 2.1 (columns 3 and 4). In a similar manner, Becker et al. [44] studied the impact of the injection rate by gradually increasing \dot{m}_{UWS} from 201 mg/s to 229 mg/s while maintaining the exhaust temperature constant at 326 °C. Although deposit formation was observed from 215 mg/s, the overall deposit yield after 4 h of dosing showed that accumulation was very slow. The described results prove that deposit formation is strongly temperature-dependent. Among the influence factors, the exhaust enthalpy flux has the biggest impact. Systems readily suffer from urea deposition at low exhaust temperatures whereas excessive dosing is necessary to provoke the latter at elevated temperatures. Low ambient temperatures and high injection rates both lower the temperature of system walls and therefore promote deposition.

Schütte [35] argued that deposits formed at constant load conditions do not resemble those formed during realistic long-term test cycles with respect to type, consistency and the location of their initial formation. The author compared the amount of deposits formed during long-term test cycles of a vehicle operated at low load (urban traffic) against high load conditions. While the former showed considerable deposit formation, the latter was practically deposit free. Besides, deposits which were formed during low load cycles could be degenerated on high load cycles. These observations underline the temperature dependency of deposit formation and confirm that an increase of the temperature level reduces the deposit formation risk. Cycle-based experiments might be more realistic but complicate the isolation of single influence factors and impair the comparability of experimental results.

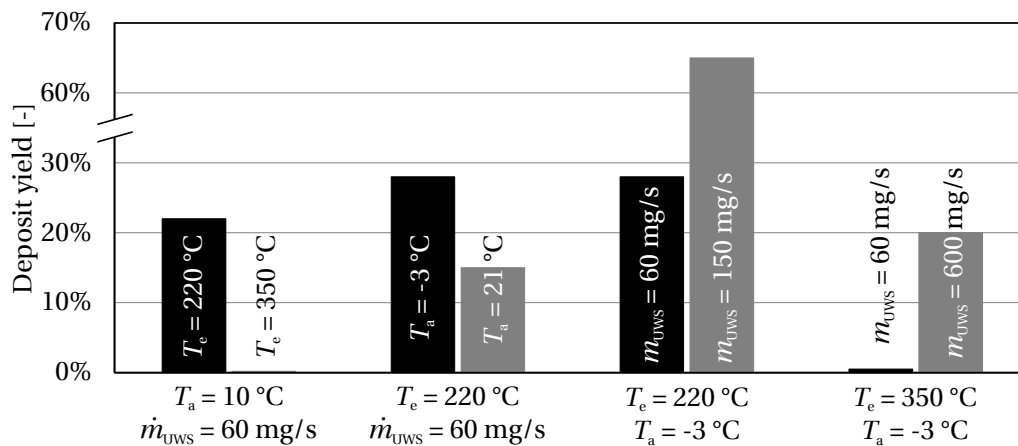


Figure 2.1: Deposit yield as a function of the exhaust temperature T_e , ambient temperature T_a , and UWS injection rate \dot{m}_{UWS} . Investigated parameter documented on the individual bars, (constant) boundary conditions specified below, total amount of injected UWS was 720 g in all experiments. Data taken from Strots et al. [34].

In order to limit the drop of the temperature level within the exhaust system, various authors have investigated the influence of an additional insulation on deposit formation. Strots et al. [34] wrapped the pipe section containing the mixing element with an additional insulation and Munnannur et al. [37] mounted a ceramic fibre insulator between injector and injector dome. Both works observed a further reduction of the deposit yield as a result of the local system wall temperature increase. As a consequence, Munnannur et al. [37] considered active injector tip cooling as a substantial contributor to deposit formation. Zheng et al. [30] concluded that "skin temperature largely affects deposit formation" and therefore recommend heat retention mechanisms, such as pipe insulation or air gap, in order to minimise heat loss.

Aside from insulation measures, the development of close-coupled type SCR systems has contributed to an increase in the temperature level [46]. In comparison to the classic underbody type setups these systems are shifted closer to the engine, and typically entail shorter mixing lengths as well as the integration of DPF and SCR catalyst, the so-called SDPF or SCR on filter (SCRoF) [46–52]. This trend compensates at least to some extent the continued reduction of diesel exhaust temperatures downstream the turbocharger during the last decade [5].

In summary, most authors come to the conclusion that deposits are formed on surfaces with emphasised wall wetting and on particularly cold surfaces of the exhaust system, e.g. [35]. However, the investigations of Strots et al. [34] and Becker et al. [44] prove that deposit formation is not necessarily limited to low temperatures. In fact, the considered range has to cover temperatures between start of injection (SOI) and at least 350 °C. Deposit formation is often studied over timescales of several hours, e.g. [37, 44]. Although this provides insights into deposit accumulation, the investigation of shorter timescales, e.g. [30], might be more realistic as mobile diesel engine operation is usually highly transient. Aside from that a direct correlation between deposit formation and exhaust temperature appears to be unfeasible as it does not allow a conclusion as to the actual surface temperature in the deposition area. In fact, this temperature will depend on the balance between exhaust temperature, mass flow, and UWS injection rate as well as the overall SCR system setup. Hence, there is no alternative to the direct measurement of such temperatures. Moreover, even though weighing was shown to be an excellent way of quantifying deposit formation, its optical assessment appears to be essential to clarify both mechanisms and timescales of deposit formation.

2.1.2 System Layout and Doser Integration

Zheng et al. [30] further investigated the influence of injector mounting and mixing elements on deposit formation. Common doser integration schemes have been compiled in Fig. 2.2. The baseline setup featured a 45° injector mounting and no mixing element. A deposit yield of 58 % was obtained in a worst case scenario at $T_e = 200$ °C, Fig. 2.3 (first column). Raising the exhaust temperature to 320 °C gradually reduced the deposit yield to negligible amounts. Adding a mixer to this setup reduced the amount of formed deposits significantly and lowered the depletion temperature to 280 °C, Fig. 2.3 (second column). It was interesting to notice that similar performance could be achieved using an S-bend type injection without mixing element, Fig. 2.3 (third column). Adding a mixer further reduced the deposit yield to a maximum of just above 10 % at $T_e = 200$ °C, Fig. 2.3 (fourth column). In addition, Zheng et al. [30] found that the temperature of the outer wall was increased by 20 °C if a mixing element was installed. Compared to the 45° injection, the S-bend type injection combined with a mixer yielded the advantage of less spray wall interaction with the (cooler) outer pipe walls. Even if a mixing device was not applied, the tangential injection still increased the surface area which was used for spray wall interaction. The results confirm the fundamental temperature-dependency and demonstrate the sensitivity of deposit formation towards the geometrical implementation of the UWS preparation section. The usage of mixing elements reduced the amount of deposit formation in all cases. Two major reasons contribute to this fact: mixers effectively increase the surface area

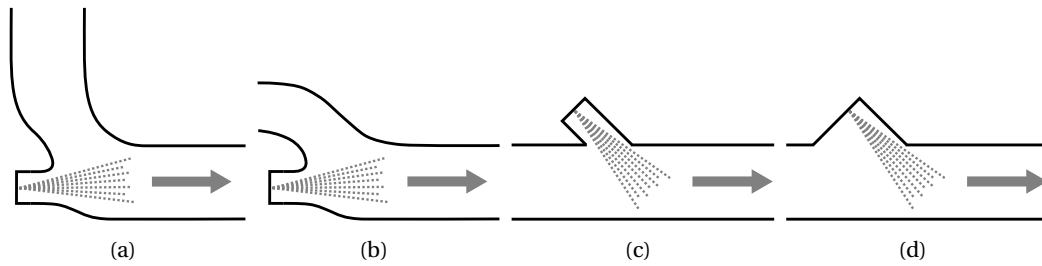


Figure 2.2: Rough classification of common doser integration schemes: elbow injection (a), S-bend injection (b), 45° injection/cross-flow injection (c). Modified doser integration: 45° injection with open injector dome geometry (d).

available for spray wall interaction and accelerate UWS preparation as they absorb exhaust enthalpy more efficiently than the outer pipe walls. As a result, the temperature level is increased not only on the mixing element itself but also on the adjacent pipe walls.

Munnannur et al. [37] investigated the influence of the injector mounting geometry on deposit formation, based on an SCR system with cross-flow injection and inclination angles of approx. 30°. Deposit formation was reported in the area of the injector dome. It was initiated at the injector gasket and accumulated to a total amount of 160 g within 16 h. Subsequent CFD calculations revealed that a recirculation zone was formed inside the dome which was capable of trapping small droplets. The authors inferred that these droplets may have deposited in the area of the injector tip, thus initiating deposit formation. In a second step, the injector dome was enlarged in order to permit the upstream flow to enter the cavity and eliminate the recirculation zone, compare Figs. 2.2(c) and 2.2(d). Munnannur et al. [37] were able to reduce the amount of deposits to one fourth of the original value. The results are consistent with the findings of Way et al. [33]. Seo [36] moreover suggested that gaps between injector dome and pipe could be a starting point for deposit formation since they are likely to be isolated from heat sources. The author also proposed an optimised injector dome geometry and demonstrated the reduction of the recirculation zone size using CFD. These results corroborate that injector domes are commonly prone to deposit formation. Recirculation zones consolidate the thermal isolation of the cavities as well as poor exhaust and species exchange with the main flow. However, they can be suppressed if the injector dome geometry is adapted in order to allow a continuous supply with fresh exhaust. The latter effectively reduces the risk for deposit formation. In order to avoid overheating the

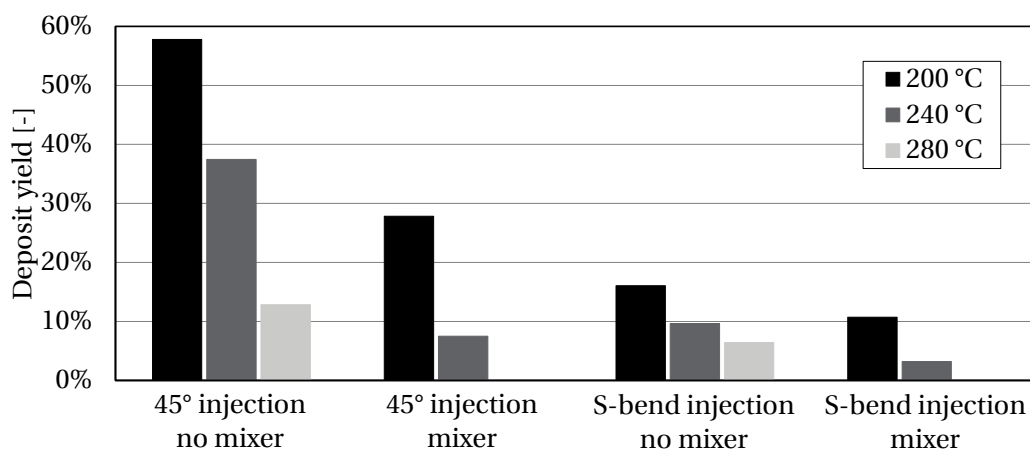


Figure 2.3: Deposit yield as a function of the exhaust temperature T_e for different doser integration schemes, with and without mixing element. Exhaust mass flow $\dot{m}_e = 120$ kg/h, UWS injection rate $\dot{m}_{UWS} \approx 32$ mg/s, experiment duration 30 min. Data taken from Zheng et al. [30].

injector tip, actively cooled injectors may have to be used and/or the injector tip protrusion adjusted. Investigations by Smith et al. [53] furthermore indicate that the findings of Way et al. [33], Seo [36] and Munnannur et al. [37] may easily be transferred to SCR systems with S-bend injection. In fact, CFD results revealed the formation of a double vortex which must further deteriorate species exchange and heat transfer, see Fig. 2.4. Munnannur et al. further concluded that recirculation zones in the direct vicinity of spray cones should be avoided to prevent small droplets from getting trapped.

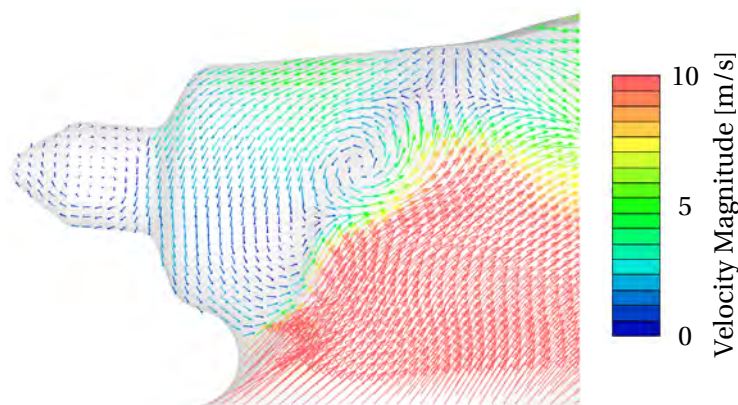


Figure 2.4: Exhaust flow recirculation on a central cross section in the injector dome in an underbody type SCR system, $T_e = 200\text{ }^\circ\text{C}$, $\dot{m}_e = 100\text{ kg/h}$. Adapted from Smith et al. [53].

Concludingly, both deposit yield and location can be manipulated extensively by modifying the system layout. Geometric imperfections of system walls, such as recesses, seams, or elevations, are especially prone to deposit formation [35]. Common injector dome geometries often cause recirculation zones which increase the deposition risk due to the deterioration of gaseous species exchange. Spray targeting onto system walls and in particular the application of mixing elements usually contribute significantly to UWS preparation. In all experiments specific design features were identified as major reason for deposit formation. However, the diversity of the impact factors and the complexity of their interaction also reveal that such correlations can hardly be generalised. In fact, a reasonable analysis of the deposit formation risk must consider all aspects of their interaction.

2.1.3 Mixing Element Design

Conflicting optimisation criteria, such as backpressure increase, reductant mixing performance and resistance against deposit formation, have led to the development of a broad variety of mixers, e.g. [27–29, 53–55], see Fig. 2.5. It has been established in Section 2.1.2 that the usage of mixing elements can substantially contribute to a reduction of the deposit yield. A number of works have aimed at identifying mixer types and features which yield a high resistance against deposit formation. Zheng et al. [30] demonstrated a reduction of the deposit yield with both a butterfly mixer and a grid mixer. They concluded that the large surface area of the latter contributed to its good performance, similar to a wiremesh mixer. Way et al. [33] compared different exhaust system configurations with swirl as well as flapper type mixers and observed that only the supplementary application of a wiremesh disc completely eliminated deposit formation. Schütte [35] minimised deposit formation by adapting the mixing element in a manner which reduced the amount of wall film formation. In a qualitative study, Schiller et al. [55] found that swirl mixers outperformed flapper mixers with respect to what they called *deposit performance*, i.e. the resistance of the system against deposit formation. By optimising their baseline wiremesh, the authors were able to reduce the amount of formed deposits to a negligible level. In contrast, the flapper-type mixer exhibited a noticeably higher deposit yield.

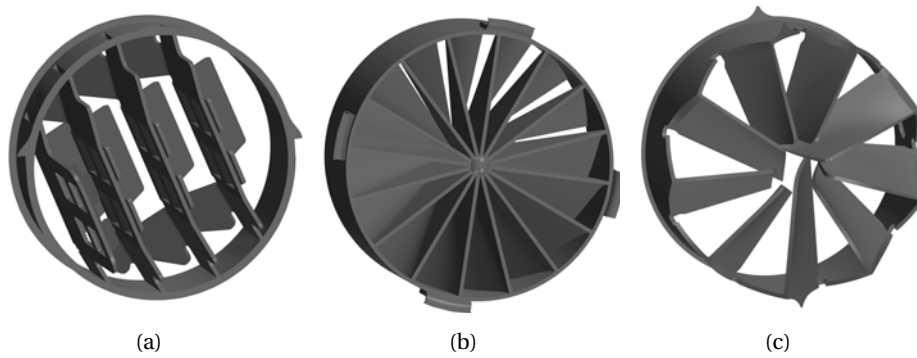


Figure 2.5: Overview of typical mixing element geometries: two-stage blade mixer (a), swirl mixer (b), and plate mixer (c). Adapted from Smith et al. [45, 53].

It is evident that it is not possible to provide a definitive answer to the question as to what kind of mixer design yields the highest resistance against deposit formation. Two major reasons contribute to this circumstance: firstly, system performance is not solely determined by the mixing element but by the combination of mixer, mixing section and doser integration. Secondly, a comparative study, which evaluates the deposit yield for a multitude of different mixing elements or single design parameters thereof, is not available to this date. Typically, only two or three models are compared against each other [30, 55], operating conditions are inconsistent [30] or the studies fail to provide complete data on the deposit yield [33, 55]. Furthermore, manufacturers are protective of the technical details of their designs which makes it virtually impossible to identify single parameters improving the deposit performance, e.g. Schiller et al. [55]. Nevertheless, the findings confirm the previous conclusion that the usage of mixing elements can substantially contribute to a reduction of the deposit yield, see Section 2.1.2. Moreover, wiremesh mixers may be applied in addition to common mixing elements in order to further reduce or eliminate the formation of deposits. In general, it appears that authors agree on the fact that mixer designs with large surface areas mitigate the risk of deposit formation, e.g. [30, 33]. This can most probably be attributed to the distribution of the wall film over a larger area. In such cases both the surface to volume ratio of the wall film as well as the local ratio between available exhaust enthalpy flux and wall film mass are increased which effectively accelerates UWS preparation.

2.1.4 Mixing Section Design

In order to reduce the amount of deposits formed on outer pipe walls opposite to the injector or on mixing elements, various authors have experimented with a local reduction of the exhaust pipe cross section. Based on CFD calculations of a straight pipe geometry with cross-flow injection and a number of splash plates, Munnannur et al. [37] found that a diameter reduction of the mixing section effectively reduced the amount of wall film formation, compare Figs. 2.6(a) and 2.6(b). Experimental results on a similar geometry confirmed that this measure can help to eliminate the formation of deposits. The results are consistent with the findings of Seo [36] who conducted CFD calculations and test bench measurements based on a similar geometry without mixer. By reducing the pipe cross section in the injection area, he was able to considerably reduce the amount of formed deposits. Brück et al. [56] avoided a complete redesign of the mixing section by simply adding a nozzle-shaped insert upstream the mixing element to focus the enthalpy flux, compare Figs. 2.6(a) and 2.6(c). The observations clearly show that a reduction of the cross section is closely related to a reduction of the deposit formation risk. Munnannur et al. [37] mainly ascribed this to the local velocity increase which in return increments the shear stresses and hence further spreads the liquid film. It can further

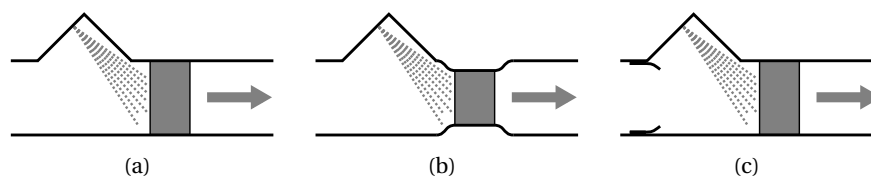


Figure 2.6: Modification of the mixing section design: 45° injection reference design with open injector dome geometry and mixing element (a), diameter reduction in the mixing section (b), and integration of a nozzle-shaped insert upstream the mixing element (c). Mixing elements shown in grey.

be concluded that owing to the constriction of the flow, the exhaust enthalpy flux is concentrated and thus the local heat input enhanced. As a result, wall film evaporation is promoted which diminishes the probability of secondary reactions.

Oesterle et al. [28, 29] found that the application of a mixing element can be complemented or at least rudimentarily compensated by providing additional impingement surfaces. Evidence for this behaviour can also be found in a recent work by Smith et al. [45]. The authors observed that droplets which passed the mixing element easily reached the catalyst intake surface due to the lack of further impingement surfaces. As a result, noticeable NH_3 hot spots were formed which can be related to the formation of deposits [16, 28, 40].

Again, the observations point out that both an increase of the wall film surface to volume ratio and the local ratio between available exhaust enthalpy flux and wall film mass contribute to UWS preparation. In any case, the mixing section should provide sufficient impingement surfaces to realise liquid phase decomposition upstream of the catalyst substrate.

2.1.5 Spray and Doser Characteristics

During the injection process, UWS is atomised and a polydisperse spray is produced. The major spray parameters can be adjusted through the design of the nozzle hole disc or the nozzle shape, in case of hollow cone injectors. Single and multi-hole dosers can be realised with a large variety of injection (cone) angles. The characteristics of the spray are determined by the nozzle shape(s) and diameter(s), and can be modified by means of the injection pressure. Typically, the Sauter mean diameter (SMD or d_{32}) is specified in order to describe the droplet spectrum [57]. It relates the surface area of all droplets to their volume and is therefore a characteristic quantity of the spray, especially in terms of its evaporation behaviour. An increase of the injection pressure effects a reduction of the SMD while the droplet injection velocity is increased [58]. The same behaviour can be observed for a reduction of the nozzle diameter. On the one hand, droplets of smaller size evaporate more quickly [32, 59]. On the other hand, their trajectories are manipulated by the exhaust flow more easily, which may significantly affect the spray targeting and can lead to droplet trapping within recirculation zones [37]. The term *spray targeting* may therefore not be reduced solely to the orientation of the spray cone axes. It also includes the ability of the spray to resist a deflection by the flow field sufficiently in order to guarantee that the desired target surfaces are hit, e.g. on the mixing element. Both Schütte [35] and Smith et al. [53] documented deposit formation on the nozzle hole disc and inside the injector dome. However, both areas are undesired as spray targets and a number of investigations has been conducted to shed light on the mechanisms of their formation as well as the dominant impact factors.

Smith et al. [53] found caldera-shaped deposits on the nozzle hole disc throughout their entire study, compare Figs. 5.2(a), 5.2(e) and 5.2(i). In contrast, Schütte [35] observed that such deposits were periodically dissolved and purged or transported to adjacent surfaces. In his experiments, he was able to

provoke dome-shaped deposits only by excessively increasing the temperature. This is plausible given the fact that, at identical exhaust temperatures of 200 °C, Smith et al. [53] measured injector dome wall temperatures around 140 °C while Schütte [35] reported average temperatures around 108 °C. The author also documented that a further reduction of the temperature level caused a linear increase of the deposit yield from just under 10 % at 101.5 °C to roughly 55 % at 50.3 °C. On the one hand, the temperature drop of the wall below approx. 133 °C (urea melting temperature) shifted the dominance of deposit formation pathways from chemical reaction products to crystallised urea, see Section 2.2.1. On the other hand, the temperature drop further reduced the evaporation rate of the water content and therefore promoted the continuous removal of deposits from the nozzle hole disc by mitigating urea crystallisation locally. Potential deposits must have been continuously dissolved and shifted further inside the system. The results underline the fundamental temperature-dependency of deposit formation and confirm that the injector dome geometry has significant impact on the actual heat exchange.

Four major mechanisms have been proposed in order to explain the relevant wall wetting mechanisms inside the injector dome. **Droplet injection outside the spray cone (1)** may not only be observed during injector opening and closing but has to be considered as common for UWS injectors. Real spray cones cannot be delimited sharply and are usually specified by optically determining the cone angle which contains 90 % of the actual droplet mass. In case the distance between this core spray cone and the injector dome walls is chosen too small, they may easily be wetted, see Fig. 2.7 (hypothesis I). **Droplet deflection by recirculation zones (2)** occurs as the flow field inside the injector dome is usually characterised by an exhaust recirculation which is driven by the main flow, see Section 2.1.2 and Fig. 2.4. In addition, small recirculation zones may be generated through entrainment of the exhaust by the injection bursts. Small droplets are decelerated rapidly after injection and may easily remain inside the dome until the next injection event. Such droplets may easily be caught in recirculation zones and impinge on adjacent injector dome walls, see Fig. 2.7 (hypothesis II). **Trickling of wall films originating from a permanently wetted nozzle hole disc (3)** triggers the wetting of adjacent injector dome walls, and has been attributed to injector leakage and UWS remainders from previous injection events [53, 60, 61], see Figs. 2.7 (hypothesis III) and 2.8. **Delayed droplet release (4)** may be caused by rebound effects of the injector needle and can lead to the release of (large size)

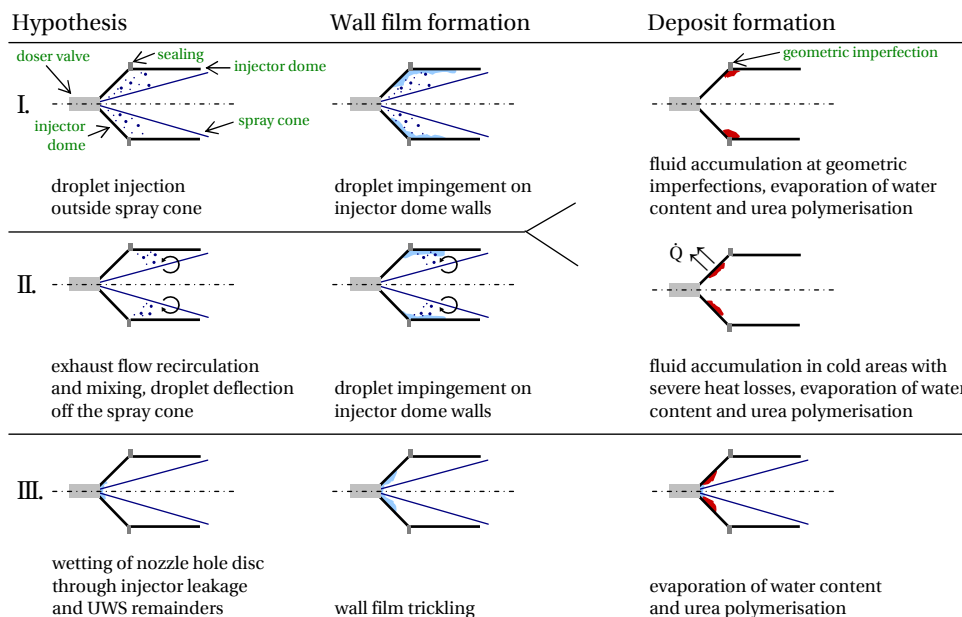


Figure 2.7: Schematic overview of hypotheses about the deposit formation mechanisms inside the injector dome. Adapted from Schütte [35].

droplets after injector closing [53, 60–62]. Such droplets are usually characterised by arbitrary trajectories and low injection velocities. Therefore, they may easily be diverted towards the injector dome walls by the local flow field or, in case of heavy droplets, by gravitation.

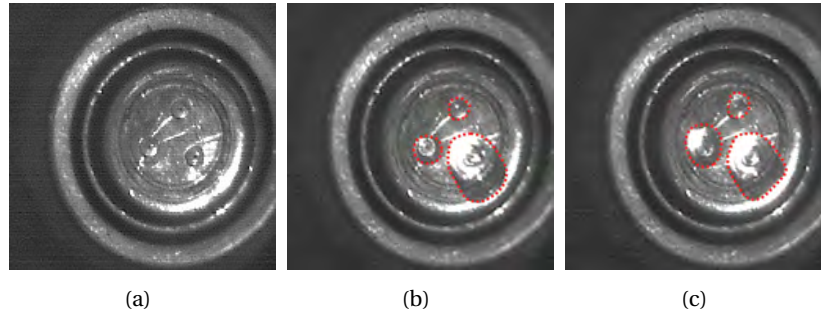


Figure 2.8: Gradual wetting of the nozzle hole disc by UWS leakage after injector closing: clean injector prior to first injection event (a), and wetted nozzle hole disc prior to second (b) and third (c) injection event. 3-hole injector, injector tip temperature 140 °C, UWS injection rate $\dot{m}_{\text{UWS}} = 13$ mg/s. Wetted areas marked in red.

Dong et al. [16] and Schütte [35] experimentally assessed the impact of a number of operating parameters and doser characteristics on the formation of deposits in the injector dome. Schütte found that a variation of the injection frequency at constant injection rate did not affect the deposit yield up to 6 Hz. However, a considerable increase was observed at 8 Hz and may be attributed mainly to amplification of phenomena related to injector opening and closing (mechanisms 1, 3, and 4) but also to a more consistent excitation of recirculation zones by the spray bursts (mechanism 2). Besides, the cooling efficiency of the evaporating wall film is also determined by its distribution, i.e. by its surface to volume (or area to thickness) ratio. Injection with higher frequencies on average leads to thinner films as the introduction of the liquid phase is more evenly distributed over time. As a result the evaporation rate increases which in turn promotes the cooling efficiency. Eventually, the local temperature drops to lower levels which correlates with higher deposit yields, see Section 2.1.1. Both Dong et al. [16] and Schütte [35] also investigated the impact of the injection pressure on deposit formation and documented opposing trends. Schütte [35] observed emphasised wall wetting and an exponential increase of the deposit yield if the pressure was raised from 3 bar to 7 bar. The entailed reduction of the spray SMD facilitates droplet deflection by recirculation zones (mechanism 2). Moreover, the pressure increase probably also brought along an increase of the spray cone angle and might have led to direct droplet impingement or at least to an amplification of indirect wall wetting by droplets injected outside the major spray cone (mechanism 1). In contrast, Dong et al. [16] showed that injector operation with 8 bar instead of 2 bar eliminated deposit formation both on the pipe walls and the SCR catalyst inlet. The pressure increase, in combination with a modified nozzle hole disc, must have impeded deposit formation by improving liquid phase atomisation and by spreading the spray targeting onto a larger surface. In separate measurement campaigns Schütte also quantified the deposit yield as a function of the spray cone angle (at approx. constant SMD) and the SMD (at constant spray angle). In line with previous findings the evidence suggests that, although an intensified spray atomisation may theoretically help to mitigate deposit formation, the impact of the spray targeting dominates the potentially accelerated droplet evaporation in finer sprays. This is due to the fact that in typical SCR systems the timescales between droplet injection and impingement are very short in comparison with the droplet depletion timescales [31, 32, 63]. The results confirm the importance of optimising the combination of mixer, mixing section and doser integration in order to prevent local areas of wall film accumulation.

Altogether, the four hypotheses provide a comprehensive outline of the mechanisms of deposit form-

ation specific to the environment of the injector, which go beyond direct wall wetting: droplet injection outside the spray cone (I), droplet deflection off the spray cone by recirculation zones (II), as well as irregular dosing in the form of injector leakage (III), and delayed droplet release (IV). While the behaviour and impact of single injector parameters and doser characteristics appears to be well understood, generalised correlations cannot be derived. As in the case of the overall system layout, a reasonable analysis of the deposit formation risk must consider all spray characteristics and their interaction with other system components. A comparison of the findings described in Sections 2.1.1-2.1.5 yields that deposits have to be classified into two categories: injector-related deposits and wall wetting-related deposits. While the former can be linked to parasitic effects or malfunctioning of the injector itself, such as leakage, the latter can be attributed to droplet impingement at the wall.

2.2 Chemistry and Physics of Deposit Formation

The review of deposit formation in Section 2.1 helps to understand general trends and the influence of single design aspects. However, many underlying mechanisms cannot be identified in complete SCR systems as chemical and physical subprocesses superimpose. The relevance and impact of these subprocesses shall be clarified in this section and help to understand the root causes and mechanisms of deposit formation. A comprehensive reaction scheme of urea decomposition is provided alongside with crucial temperatures, components and off-gases. The influence of boundary conditions on the outcome of the decomposition process are reviewed as well as the formation of wall film as a precursor of deposits and crystallisation. Individual mechanisms which promote or impede deposit formation are pointed out.

2.2.1 Urea Decomposition Pathways

The chemistry of urea decomposition has been investigated under laboratory conditions in numerous works [14, 16, 17, 43, 64–68]. However, the most comprehensive outline of the urea decomposition chemistry has been presented by Schaber et al. [14, 67]. Based on thermogravimetric analyses (TGA) the authors identified three major urea decomposition steps: room temperature to 250 °C, 250...360 °C and above 360 °C, associated with mass losses of approximately 72 %, 24 % and 4 % [14], see blue curve in Fig. 2.9. Moreover, high performance liquid chromatography (HPLC) and Fourier transform infrared spectroscopy (FTIR) were applied to determine the contents of urea decomposition residue and pyrolysis off-gases. Based on the combined experimental data and a review of possible chemical pathways, Schaber et al. [14] classified the pyrolysis process into four reaction or temperature regimes. In the present work, this scheme will be adopted, complemented wherever appropriate, and extended to include the chemistry of even more temperature-stable deposit components. The present section shall provide a general outline of urea decomposition, which has also been summarised in a schematic overview, Fig. 2.10. The subsequent Section 2.2.2 will discuss the impact of the experimental boundary conditions and draw a conclusion on the relevance of the individual decomposition by-products.

Reaction Regimes

The urea melting and decomposition temperature has been reported around 133 °C [14, 69, 70]. It can be seen as the onset of the **first reaction regime** even though urea does not exhibit noticeable mass loss below approx. 152 °C [14]. Decomposition proceeds in the form of a thermolysis reaction, Eq. (1.1), via ammonium cyanate [$\text{NH}_4^+\text{NCO}^-$] as an intermediate [14, 71, 72] and eventually yields

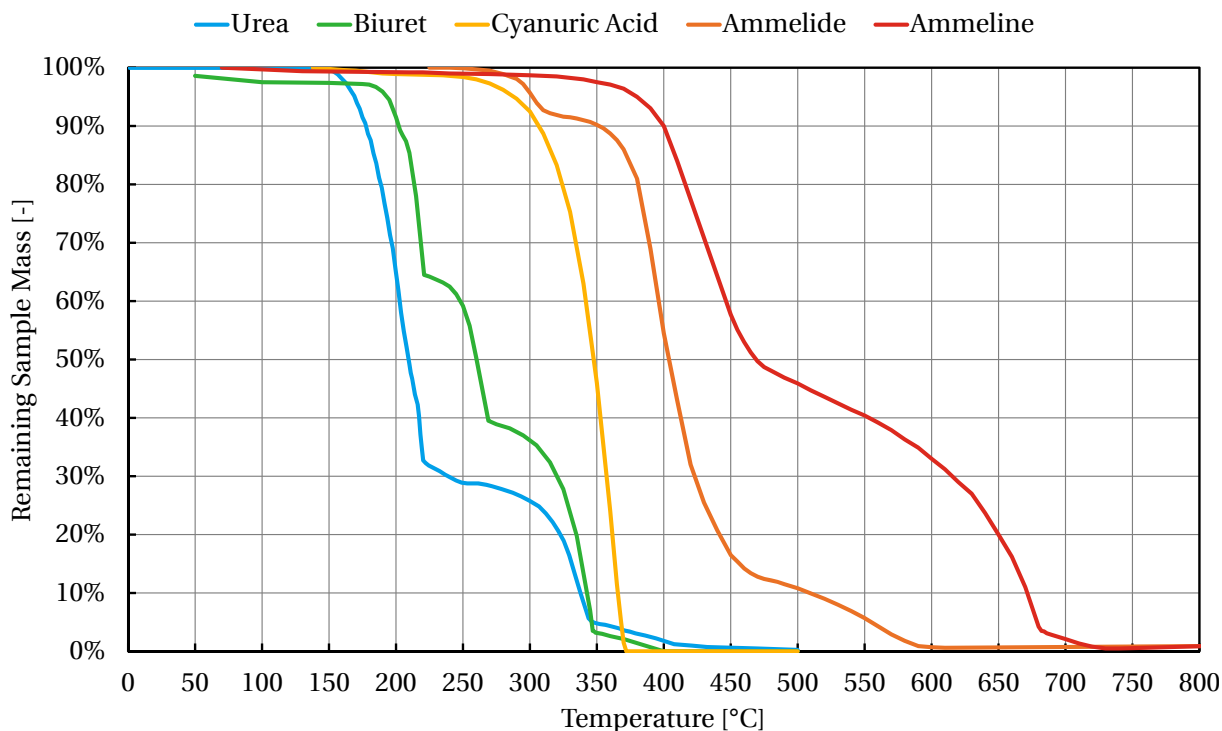


Figure 2.9: Thermogravimetric analysis of urea, biuret, cyanuric acid, ammelide and ammeline decomposition. Heating rate 10 °C/min, purge gas N₂, sample mass 30 mg. Data taken from Schaber et al. [14].

gaseous ammonia and isocyanic acid. It has been established that isocyanic acid can easily be hydrolysed on a typical SCR catalyst according to Eq. (1.2) [19, 73, 74]. However, in the absence of a suitable catalyst, it remains stable in the gaseous phase up to temperatures in the range 700...1000 °C for several seconds [19, 75]. The very high reactivity of isocyanic acid [71, 76] and its availability in close proximity to the urea melt are the root causes for undesired secondary reactions. As a consequence, biuret formation is initiated around 160 °C through reaction of intact urea with gaseous isocyanic acid [14, 43, 68, 70, 77]. It is paralleled by small amounts of cyanuric acid as well as ammelide formation from 175 °C [14, 43, 64, 66, 68, 70, 78]. Essentially, the first reaction regime is dominated by the conversion of urea into biuret [14, 70].

The **second reaction regime** commences at temperatures exceeding 190 °C, when alternative chemical pathways gain in importance. The onset of biuret melting and simultaneous decomposition has been documented at approx. 193 °C [14, 33, 64, 79], see Fig. 2.9. Its decomposition proceeds via urea, which is unstable at this temperature and rapidly undergoes thermolysis [14, 64, 68]. However, biuret may also react to yield cyanuric acid and ammelide, which exhibit increased production in this temperature range [14, 43, 64, 68]. The second reaction regime also marks the onset of ammeline and triuret formation [14, 17, 64, 70, 71, 80]. Moreover, the direct trimerisation of isocyanic acid has been documented in the literature [14, 43, 64, 68], although the produced cyanuric acid will rather be dispersed in the gas phase than deposited on system walls. Between 210 °C and 225 °C the urea and biuret decomposition residue precipitate in the form of a sticky solid matrix [14, 64, 70]. This phenomenon becomes visible in the form of a narrow plateau region during urea decomposition and is even more prominent during biuret decomposition [14, 33, 37, 64–66, 70], see Fig. 2.9. At this point, urea decomposition has left cyanuric acid and ammelide as the major components of the residue [14, 70]. Due to the solidification of the melt, ammonia and isocyanic acid can hardly diffuse from the system but get trapped in the matrix or are stored in the form of ammonium cyanate or hydronium cyanate [14].

Likewise, urea and biuret can interact with cyanuric acid and be stored within the solid matrix. At temperatures as low as 220 °C the decomposition of triuret is initiated and mainly yields cyanuric acid [64, 70, 81]. Moreover, cyanamide formation might act as an intermediate during the production of melamine [14]. Essentially, the second reaction regime is dominated by the conversion of urea and biuret into cyanuric acid and ammelide [14, 70].

Another transition between the dominating chemical pathways marks the onset of the **third reaction regime** at temperatures in excess of 250 °C. With temperatures approaching 275 °C the decomposition of cyanuric acid and the cyanates into the gas phase becomes noticeable [14]. Above 300 °C, amination reactions contribute to the decomposition of cyanuric acid, ammelide and ammeline [14, 43, 68, 78]. Ammelide and ammeline sublimation commence at 340 °C and 310 °C [14]. Around 350 °C, urea, biuret and stored cyanates are practically depleted and the major part of the cyanuric acid is decomposed [14, 70]. At this point, cyanuric acid, ammelide, ammeline and melamine are the major components within the decomposition residue. Essentially, the third reaction regime is characterised by the decomposition of cyanuric acid. Depending on the boundary conditions, the immediate decomposition into the gas phase competes with the conversion into the more temperature stable components ammelide and ammeline.

Around 350 °C the dominant chemical pathways exhibit another change. The mass plateau in the urea TGA indicates the onset of the **fourth reaction regime** [14, 33, 37, 43, 70], see Fig. 2.9. Above this temperature, the residue gradually continues to decompose. Ammelide and ammeline melt with decomposition at approximately 410 °C and 435 °C [64], respectively. Urea depletion can be completed at temperatures around 450 °C, indicating that minor residual amounts of ammelide, ammeline and melamine easily decompose or sublime into the gas phase. However, the comparison of the final urea decomposition stage with the pyrolysis of pure ammelide and ammeline clearly shows that below 450 °C neither sublimation nor decomposition of the latter occurs at sufficient rates to decompose larger amounts of these components, Fig. 2.9. In fact, temperatures in the range 600...725 °C were required to deplete the samples [14]. Moreover, both ammelide and ammeline exhibit mass plateaus during decomposition at roughly 475 °C [14, 64], suggesting the formation of even more complex molecules as intermediates during their decomposition. Supporting evidence for this conclusion can be found in the work of Koryakin et al. [64], who identified melon as the final pyrolysis product. This is also in line with results of Eichelbaum et al. [43] who found that urea decomposition could be delayed up to temperatures around 750 °C and identified the decomposition residue at 500 °C as a mixture of melem and melon. Essentially, the fourth reaction regime is characterised by the decomposition of ammelide and ammeline. Depending on the boundary conditions, the immediate decomposition into the gas phase competes with the conversion into the more temperature stable components melem and melon.

If urea decomposition is not completed between 400 °C and 450 °C, the formation of melamine condensates gains in importance and starts to compete with the sublimation and decomposition of the residual triazines cyanuric acid, ammelide, ammeline and melamine. Melamine sublimation is initiated below 250 °C and peaks around 345 °C [14, 82]. In a parallel process melamine may, however, be converted into melem starting from around 367...380 °C [82], most probably via the rather unstable intermediate melam [80, 82–86]. It is likely that the conversion of residual triazines into melem is completed around 475 °C where both ammelide and ammeline decomposition exhibit another mass plateau, see Fig. 2.9. Melem conversion into the most stable melamine condensate melon is expected to commence in the range 420...425 °C [64, 80, 82, 84, 86, 87]. Eventually, melon decomposition becomes effective above 500...520 °C [83, 88, 89] and may continue to temperatures up to 850 °C [83, 87]. Possible decomposition pathways include reverse reactions via melem, melam, melamine, ammeline and ammelide back to cyanuric acid [68, 80]. As the reaction products are unstable at this temperature level they continue to decompose via sublimation [14, 18, 43, 87, 90] or further chemical conversion. Cyanuric acid decomposes into gaseous isocyanic acid. Ammelide, ammeline and melamine may

also decompose into ammonia and isocyanic acid via the formation of cyanamide [78]. This is in line with the results of Jones et al. [91] who found that even in the range 450...750 °C the urea decomposition off-gases were composed of varying ratios of ammonia, isocyanic acid and carbon dioxide. Eichelbaum et al. [43] observed that above 625 °C the decomposition residue were converted into (CN)₂ (cyanogen) and HNCO. Other possible decomposition products include HCN (hydrogen cyanide) and N₂ [18, 83, 87, 90]. Due to their high formation temperatures (\approx 365 °C) the formation of melamine condensation products such as melam, melem and melon will be relevant rather for the decomposition of present deposits than for their formation.

Summary

In summary, urea decomposition can be divided into four reaction regimes which are characterised by the dominance of different chemical pathways, see Fig. 2.10. Urea melts at 133 °C but does not exhibit noticeable decomposition below roughly 150 °C. Biuret decomposition commences around 160 °C and is paralleled by small amounts of cyanuric acid and ammelide formation from 175 °C. Above 190 °C, biuret decomposition is initiated and accompanied by increased production of cyanuric acid, ammelide and ammeline. Cyanuric acid decomposition contributes to further mass losses from 250 °C and is paralleled by gradual conversion into ammelide, ammeline and melamine above 300 °C. The experimental data shows that, if the decomposition of the triazines cyanuric acid, ammelide, ammeline and melamine is not completed up to approx. 450 °C, the accumulation of melamine condensation products, such as melem and melon, may be triggered. Melem is formed from roughly 365 °C and its conversion into melon starts around 420 °C. Temperatures in excess of 500 °C are required for melon decomposition to become effective. Fast decomposition may even require temperatures exceeding 600 °C.

Ammonium cyanate acts as an intermediate during urea decomposition, just as melem formation proceeds via the intermediate melam. In a similar manner, gaseous cyanamide is believed to act as an intermediate during the production and decomposition of melamine production. Furthermore, the evidence suggests that gaseous species can either get trapped or interact with each other and be stored in ionic form in the matrix of solidified decomposition residue. In a similar manner, small amounts of urea and biuret might get bound in the form of ionic cyanurates by interacting with cyanuric acid.

In terms of solid phase components urea decomposition residue are dominated by the presence of urea, biuret and cyanuric acid, ammelide and ammeline. While the former three constitute the major components with respect to deposit mass, the latter two are crucial because of their temperature-stability. Urea, biuret and cyanuric acid may easily be identified and distinguished with thermogravimetric analysis. In contrast, ammelide and ammeline cannot safely be differentiated. However, the identification of mixtures thereof is deemed sufficient to determine the severity of the deposit composition. Common deposits will hardly contain any melamine condensation products, assuming wall film as a precursor for deposit formation and a maximum wall wetting temperature below 350 °C. Above, their formation can easily be triggered, e.g. during deposit decomposition. In terms of gaseous species NH₃, HNCO, H₂O and CO₂ have to be considered as the major components involved in urea decomposition. In particular up to around 190 °C the decomposition chemistry is mainly dependent on the availability of isocyanic acid. While the consumption of isocyanic acid is gradually omitted above 190 °C, ammonia begins to play a major role starting from approx. 300 °C. Both H₂O and CO₂ will be available in diesel exhaust in any case, besides the fact that noticeable amounts of water vapour are produced during the initial phase of UWS decomposition as well.

2.2.2 Boundary Conditions and Catalysis

A review of thermogravimetric experiments of urea and its decomposition by-products yields that the experimental boundary conditions have a significant impact on the respective decomposition processes [14,16,33,37,40,43,64–66,70]. Direct comparisons are usually problematic if measurements differ in more than one parameter. Common influence factors include the crucible geometry, sample mass and consistency, purge gas and flow rate as well as boundary conditions which may directly affect the chemistry, such as the presence of moisture or a catalyst.

Brack et al. [70] showed that urea depletion was delayed if the sample mass was increased. The completion of the cyanuric acid decomposition stage (third reaction regime, see Section 2.2.1) was shifted by more than 50 °C for a twentyfold increase of the sample mass, see Fig. 2.11(a). The amount of residual by-products at 260 °C increased more than twofold. Besides, the lighter sample was depleted around 375 °C whereas nearly 9 % of the heavier sample were left undecomposed at this temperature. Given the very low heating rate of 2 °C/min it is unlikely that thermal inertia noticeably contributed to the delayed sample depletion. However, the increase in mass results in a lower surface to volume ratio and thus prolongs both decomposition and evolution of gaseous species. The gas phase concentrations are maintained on a higher level which in turn promotes undesired secondary reactions. In conclusion, both the temperature-stability and the depletion time of a deposit increase with its mass, even if the initial composition remains unchanged.

Brack et al. [70] also documented that an increase of the heating rate shifted the depletion temperatures of urea, biuret and cyanuric acid towards higher values, see Fig. 2.11(b) (data for biuret and cyanuric acid not shown). The intensification of by-product formation primarily affected urea. Both the increase of thermal inertia and the lowered residence times in given temperature windows defer the decomposition process towards higher temperatures where secondary reactions are more probable and/or proceeded at higher rates. This is in line with experimental results of Lundström et al. [92]. The authors decomposed UWS from an impregnated monolith and found that the increase of the heating rate intensified biuret production. Despite this, less time may be required for the decomposition with higher heating rates, as the increased depletion temperatures will usually still be reached

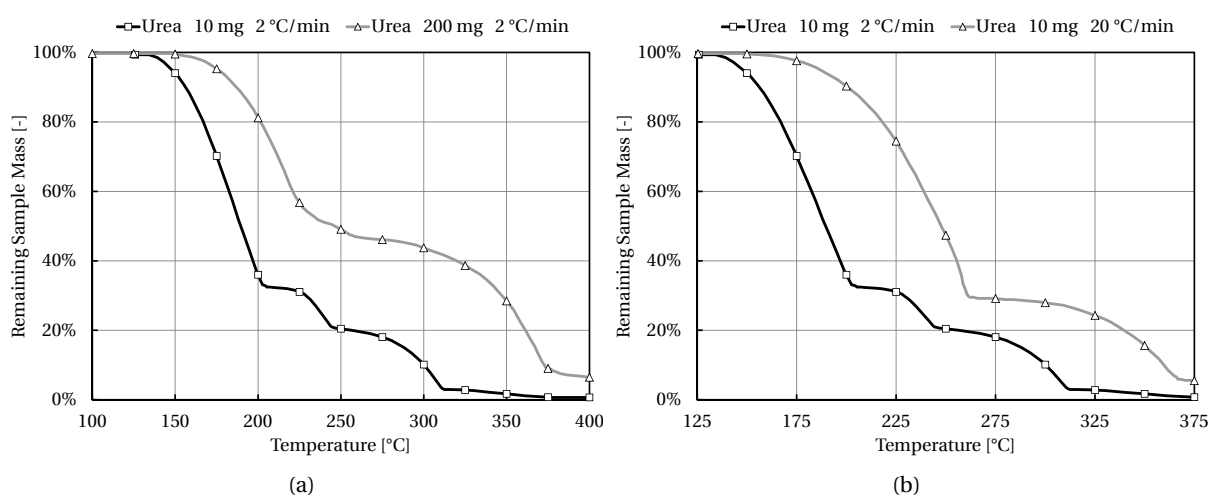


Figure 2.11: Thermogravimetric analysis of urea decomposition for different sample masses (a) and heating rates (b). Purge gas N_2 , cylinder-like crucible. Data taken from Brack et al. [70]. Residual weight of the samples marked with symbols every 50 °C in order to facilitate identification and comparison.

faster. In the context of a deposit this means that higher heating rates are always desirable if the target temperature is high enough to allow sample depletion. In all other cases decomposition at low heating rates is preferable as it involves less by-product formation.

Multiple authors demonstrated that sample decomposition was delayed and by-product formation increased if an open crucible was covered with a lid [43, 64, 70], see Fig. 2.12(a) (data for biuret and cyanuric acid not shown). The slower removal of gaseous species by the purge gas effect higher local gas phase concentrations [43, 64, 92]. The increase in concentration does not only promote undesired secondary reactions but also delays decomposition into gaseous components by shifting the equilibrium of the individual reactions towards the liquid/solid phase [64, 78, 92]. In conclusion, less deposits will be formed during UWS preparation in locations which allow quick removal of reaction off-gases. Equally, present deposits will decompose faster and with less by-product formation.

Multiple works investigated the impact of moisture on the decomposition process of urea [17, 43, 70], as it is required for the hydrolysis of HNCO, Eq. (1.2). The presence of water vapour accelerated the completion of individual decomposition stages [70], see Fig. 2.12(b), reduced the formation of by-products, and contributed to the decomposition of temperature-stable triazines, such as ammelide and ammeline [43]. The actual concentration of the moisture did not appear to affect the process [70]. The experiments clearly indicate that moisture can accelerate urea decomposition over the whole temperature range if the boundary conditions do not impede or inhibit a direct contact between sample and water vapour. Below 300 °C, moisture may help to reduce deposition by hydrolytically lowering the amount of isocyanic acid available for secondary reactions. However, the effect should be limited to deposit formation locations with very poor gas exchange as isocyanic acid is quite stable in the gas phase [19, 75] and noticeable gas phase hydrolysis requires residence times exceeding those expected for SCR systems [15]. Above 300 °C, moisture can contribute to the decomposition of ammelide, ammeline and melamine by promoting desamination reactions, see Section 2.2.1.

The question arose whether or not catalysts could accelerate urea decomposition. Eichelbaum et al. [43] observed that both urea thermolysis and hydrolysis were initiated and completed earlier, and

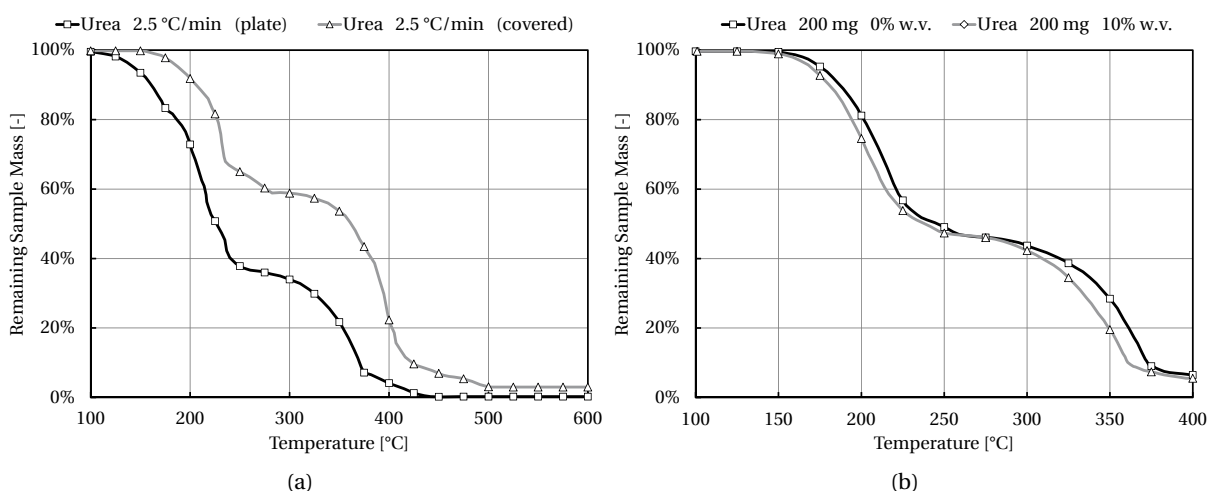


Figure 2.12: Thermogravimetric analysis of urea decomposition for different crucible configurations (a) and water vapour concentrations (b). (a): comparison of plate crucible and crucible covered with lid. Data taken from Koryakin et al. [64]. (b): purge gas N₂ with specified water vapour content (w.v.), heating rate 2 °C/min, cylinder-like crucible. Data taken from Brack et al. [70]. Residual weight of the samples marked with symbols every 50 °C in order to facilitate identification and comparison.

with less by-product formation under the presence of zeolite-catalysts, such as Fe-Beta, H-Beta, H-Y, or Cu-Y. Bernhard et al. [68] found that the presence of a TiO_2 -coated cordierite catalyst promoted the hydrolysis of urea, biuret, cyanuric acid, and melamine. The authors recommended the usage of TiO_2 as a coating for mixing elements, as realised e.g. in [34, 56], and pipe walls to impede deposit formation. As without catalytic substrates, urea decomposition was promoted if the samples exhibited higher surface-to-volume [43] ratios and under the presence of water vapour [17, 43, 68].

During deposit formation the conditions inside a typical SCR system will be more similar to experimental setups using plate crucibles or monoliths. As UWS is atomised into the system in the form of a fine spray, liquid films will be rather widespread on the mixing element and the system walls, i.e. they will exhibit high surface to volume ratios. Catalytically active coatings are rarely applied upstream of the SCR catalyst and heating rates are in the range of $20^\circ\text{C}/\text{min}$ [70], or higher. However, if present deposits decompose these boundary conditions may be different. Not only will the surface to volume ratio be lower but also the temperature level will remain on a rather constant level, leaving more time for undesired secondary reactions in the particular temperature window. While deposit formation and decomposition will qualitatively proceed according to the chemical pathways described in Section 2.2.1, the amount of formed by-products and the relevance of individual pathways will be altered depending on the boundary conditions, as described in the present section. Concludingly, differences between the reported chemical schemes and formed by-products may not be seen as inconsistencies. In fact, they reflect the dependency of deposit formation and decomposition on the boundary conditions. However, from this perspective, the specification of exact temperature thresholds appears questionable. The temperatures given in Section 2.2.1 represent reasonable values. However, decomposition may commence at lower temperatures, if heating rates are low or if samples are maintained on a certain temperature level, see e.g. [14, 64, 68, 70, 78].

2.2.3 Fluid Film and Crystallisation

It has been established that liquid film is a precursor for deposit formation, e.g. [30, 33, 36, 37, 93] and Section 2.2.1. However, impingement of UWS droplets on system walls can hardly be prevented. In fact, it is usually welcomed in order to promote UWS preparation. Therefore, the question arises under which circumstances wall film formation can be observed and which properties it will have.

Start of injection is bound to sufficient catalyst activity and UWS preparation. Catalyst light-off is often characterised by a minimum of 50 % NO_x conversion [94] and can be achieved at temperatures as low as approx. 150°C [95–97], depending on substrate and coating. UWS decomposition requires minimum temperatures around 180°C to proceed at noticeable rates [92]. Therefore, a minimum exhaust temperature of 180°C upstream the SCR catalyst is frequently taken as a threshold for the start of injection, see e.g. [98]. Depending on the individual geometry of the SCR system, the mixing element will be located roughly 200...1000 mm further upstream. Taking into account heat conduction and heat losses, the temperature at its centre will be just above 180°C prior to start of injection.

The maximum temperature up to which a wall film will be formed is called the deposition limit [99, 100]. Bai and Gosman [99] indicated that the deposition limit does not necessarily coincide with the Leidenfrost temperature, i.e. the temperature that is characterised by minimum heat transfer between wall and liquid phase. However, Birkhold [101] observed that the onset of wall wetting practically coincided with the Leidenfrost temperature. The deposition limit was therefore equated with the Leidenfrost temperature in several works, e.g. Birkhold [101] and Fischer [32]. Although measurement data is available in the literature, the reported values appear to be inconsistent and range from wall temperatures in the range $T_w = 190\text{...}210^\circ\text{C}$ (deposition limit, [30]) to $T_w = 265\text{...}280^\circ\text{C}$ (Leidenfrost temperature, [102]). The work of Fischer [32] further confirmed the dependency of the

Leidenfrost temperature on the experimental setup. In addition, the deposition limit is not necessarily a sharp and constant boundary. On the one hand, the onset of wall wetting depends on whether or not the conditions during droplet impact permit the formation of a vapour cushion. On the other hand, it depends on whether or not the cooling efficiency of the Leidenfrost effect is sufficient to lower the wall temperature to the Leidenfrost point. A review of the literature yields that it rises not only with the specific impingement mass flow rate [58, 93, 103–106]

$$\dot{m}_{\text{imp},s} = \frac{m_{\text{imp}}}{A_{\text{imp}} t} \quad (2.2)$$

where m_{imp} is the impinging droplet mass and A_{imp} the impingement area, but also with the injection frequency [106], impact Weber number [107, 108] and velocity [104, 105], surface roughness [109], and with decreasing droplet diameters [108], see Fig. 2.13. In addition, interactions between neighbouring droplets have been found to affect the experimental outcome [100]. The compiled data clearly shows that the deposition limit is essentially determined by the operating conditions and the system setup. Minimum temperatures of 280 °C, or even higher, may be necessary to effectively prevent wall wetting following the onset of dosing. Yet, the knowledge about the major impact factors may also be used to stabilise the Leidenfrost effect and hence impede the formation of deposits from wall films.

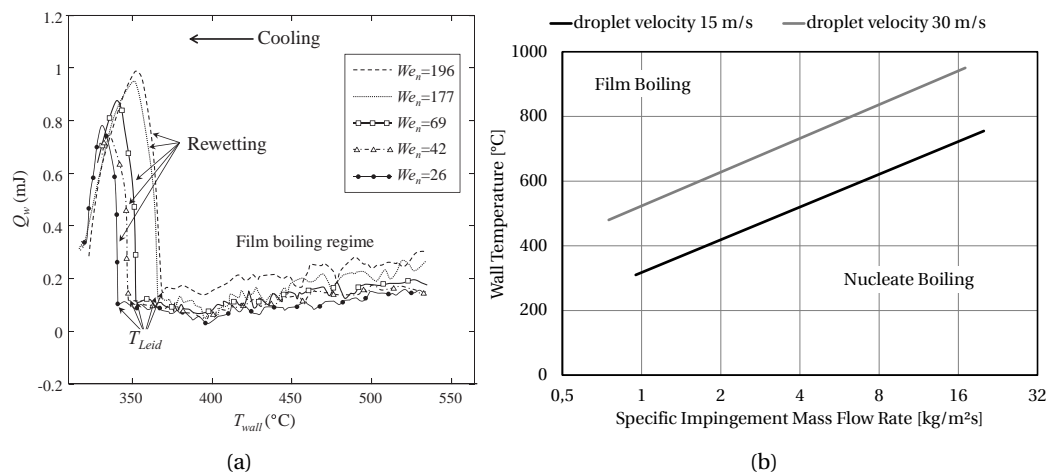


Figure 2.13: Heat removal upon droplet impact and Leidenfrost temperature as a function of the droplet impact Weber number. Water droplets on nickel plate, $d_d = 180 \mu\text{m}$. Figure taken from Dunand et al. [108] (a). Leidenfrost temperature as a function of the specific impingement mass flow rate and the droplet impact velocity. Water droplets on tool steel. Data taken from Czechowski [105] (b).

The lowest wall temperatures are typically observed in (primary) impingement areas as wall film evaporation cools system walls locally. Despite the minimum temperature requirements for the start of injection, the temperature in such areas and their vicinity may even drop below the urea melting temperature of 133 °C, see Section 2.2.1. While water continues to evaporate below 133 °C, urea decomposition is practically impeded. As a consequence the solution continuously concentrates and urea may partly recrystallise as its solubility is highly temperature-dependent, see phase diagram in Fig. 2.14. In case crystallised urea adheres to system walls this must also be referred to as deposit formation. As the process is reversible, this is primarily an undesired storage of reducing agent in the form of pure urea. However, if the conditions are unfavourable during a subsequent temperature increase, secondary reactions may be triggered and can effect a conversion into more temperature-stable deposits, see Section 2.2.2. Despite this, the major deposit formation risk appears to originate from wall film which trickles off the primary impingement areas and is gradually heated up to tem-

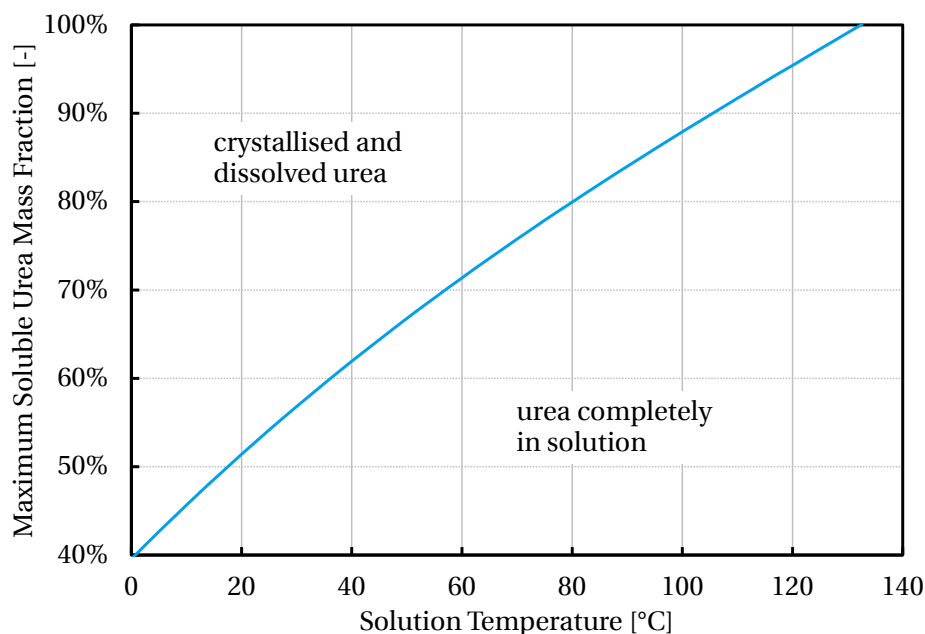


Figure 2.14: Solubility of urea in water versus temperature. Data taken from [110–113].

peratures above 160 °C, which marks the onset of secondary reactions, see Section 2.2.1. As in case of crystallisation, this process is paralleled by a continuous concentration of the film due to the ongoing evaporation and decomposition. Eventually, a deposit is formed if the exhaust enthalpy is not sufficient for complete UWS decomposition, see also Becker et al. [44].

Multiple authors attempted to correlate deposit formation with the presence of liquid film as a precursor of deposits [32, 44, 114–116]. However, the experimental data showed that, in the majority of the cases, deposits only formed in the direct vicinity of impingement areas if the exhaust temperatures were close to the deposition limit [44, 114–116]. Interestingly, primary impingement areas often remained visible despite the formation of deposits, see Figs. 2.16(a) and 2.16(c). The experimental data also proved that urea solidification occurred further downstream alongside the wall film trickling pathways if the temperature level was well below the deposition limit [37, 44, 114]. The trickling distance increased if the exhaust mass flow and/or temperature were reduced [114]. In the light of these observations the existence of a direct correlation between wall wetting and deposition remains questionable. Even though liquid film was confirmed as a precursor of deposit formation, it appears essential to capture the pathways and to consider the properties of the wall film. For this purpose, Becker et al. [44] analysed the spray surface load (SSL), i.e. the liquid film mass per unit area and time. While the approach certainly went beyond interpreting the mere presence of wall film, the authors did not find a universal correlation between the SSL and deposit formation. After all, the SSL appears to be rather a measure for the ability of the mixer to evaporate a certain amount of wall film at given operating conditions, than a direct measure for deposit formation. The available data shows that the mechanisms of deposit formation have not yet been clarified sufficiently. Further experimental backup is required to establish reliable correlations between wall wetting, wall film properties, and deposition.

2.3 Prediction of Deposit Formation

Currently available approaches for the prediction of deposit formation can be roughly classified into two categories. On the one hand, models were put forward which aimed at capturing the reaction kinetics of urea decomposition. These approaches are typically bound to reactor environments, but implement detailed chemical schemes. On the other hand, models were presented which aimed at detecting precursors of deposit formation. Commonly, these approaches can be applied on realistic SCR system geometries but vastly simplify the involved chemistry. The present section gives an overview of the available models, and points out strengths and weaknesses of the respective approaches.

2.3.1 Reaction Kinetics Modelling

Ebrahimian et al. [18] derived the first kinetic scheme to model urea decomposition chemistry. The semi-detailed scheme considered aqueous and solid urea, biuret, cyanuric acid, and ammelide alongside with intermediates such as ammonium and cyanate ions. The simulations were conducted using a (zero-dimensional) continuously stirred tank reactor (CSTR) model of the commercial software CHEMKIN AURORA. The model was calibrated and validated based on experimental results by Schaber et al. [14] and Lundström et al. [92]. The qualitative prediction of gaseous species release was acceptable both for urea and biuret pyrolysis in a crucible, as well as for UWS decomposition from an impregnated monolith. Urea mass loss was represented with good accuracy up to approx. 200 °C, see Fig. 2.15(a). However, the simulation of biuret, cyanuric acid and ammelide decomposition still lacked individual details, as in particular the ammelide decomposition chemistry was heavily simplified. In summary, the model captured fundamental trends attributed to changes of the boundary conditions, such as the sample mass, heating rate, purge gas flow rate, and different ways of sample administration (cup, pan, monolith). However, a verification of the universal applicability of the model would require the simultaneous validation of both gas phase and liquid/solid phase response to thermal decomposition, as well as a systematic variation of single parameters. Although the respective data was not shown, the authors claimed that the model had also been successfully implemented into the IFP-C3D CFD code [117].

A similar semi-detailed kinetic scheme was developed by Brack et al. [70]. The premise of the authors was to provide a framework which was able to reliably capture the impact of sample mass, heating rate, gas phase concentrations, and surface to volume ratio of the sample on the decomposition process. The scheme considered urea, biuret, triuret, cyanuric acid, and ammelide alongside with urea melting and the reversible conversion of biuret into a solid matrix. The simulations were conducted using a (zero-dimensional) CSTR model of the DETCHEM software package [118]. The model was calibrated and validated based on thermogravimetric decomposition experiments and quantitative HPLC analyses. An excellent prediction was achieved for the decomposition of cyanuric acid under different heating rates and isocyanic acid concentrations. Equally, the dependency of the mass losses of biuret and urea were predicted with good accuracy for varying heating rates. The mass fractions of biuret and its decomposition products were in good agreement with measurement results, see Fig. 2.15(b). Furthermore, the model qualitatively captured the impact of the surface to volume ratio and sample mass on urea decomposition. As in case of the model presented by Ebrahimian et al. [18], ammelide decomposition chemistry was vastly simplified. Despite this, the model appears to be suitable for coupling with CFD, as it captures the impact of the most important boundary conditions which are relevant for the formation of deposits in SCR systems. However, such an implementation would have to go along with a significant increase of the simulated time, to cover timescales in the minute to hour range.

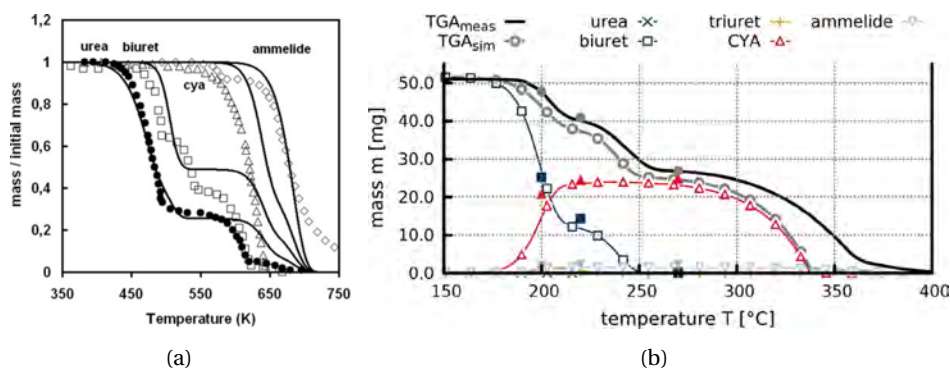


Figure 2.15: Comparison of simulation results (lines) with TGA measurements (symbols). Decomposition of 30 mg urea, biuret, cyanuric acid, and ammelide at 10 °C/min. Figure taken from Ebrahimian et al. [18] (a). Comparison of simulation results (empty symbols) with TGA and HPLC measurements (black line and filled symbols). Decomposition of 50 mg biuret at 2 °C/min. Filled symbols indicate residual masses from TGA experiments which have been analysed with HPLC in terms of their composition. Figure taken from Brack et al. [70] (b).

The approaches of Ebrahimian et al. [18] and Brack et al. [70] primarily covered components which were involved in the urea decomposition process in significant quantities. In both cases, ammelide was the most temperature-stable component which was considered. Among the authors, Brack et al. [70] managed best to systematically verify that their model captured the most relevant impact factors for the application in SCR systems, namely sample mass, heating rate, isocyanic acid concentration, and surface to volume ratio of the sample. The influence of the heating rate was captured very well, whereas at least the tendencies were represented correctly for all other impact factors. Accurate modelling of temperature-stable components would require improvements in the consideration of the decomposition chemistry of ammelide and its pyrolysis products. While a coupling of the zero-dimensional reactor models with CFD appears to be possible, its practical applicability remains closely linked to a large increase of the captured timescales.

2.3.2 CFD based Modelling Approaches

Chauvy et al. [114] made an attempt to predict deposit formation on a mixing element based on steady-state simulations using the commercial CFD code AVL FIRE. The model considered UWS injection, wall film formation, and liquid phase evaporation. Droplet wall interaction was modelled using the Kuhnke model, chemical reactions were not considered. The authors aimed at qualitatively and quantitatively correlating wall wetting with deposit formation, based on the location and extent of wall wetting. The comparison against 8 h measurements at three different operating points yielded an acceptable correlation for operation at $T_e = 300$ °C. However, the authors did not obtain neither a qualitative nor a quantitative correlation between wall wetting and deposit formation for $T_e = 170$ °C. In fact, the variation of the exhaust mass flow yielded inverse trends for simulations and measurements. The authors concluded that the deviations were due to shortcomings of the applied evaporation model and negligence of the deposition chemistry, in particular of the phase transformation. In fact, modelling liquid phase dynamics in a steady-state manner appears to be questionable, considering the strongly transient nature of droplet wall interaction, see Section 2.2.3. The results can be seen as proof that a reliable prediction of deposit formation is not feasible without the consideration of wall film properties and the coverage of the trickling pathways. Moreover, efficient model validation calls for operating conditions which yield noticeable amounts of deposits within short timescales.

Rudek [115] used a model for the simulation of ammonia homogenisation to predict deposit formation on a mixing element. The method was based on transient simulations using the commercial CFD code ANSYS Fluent. The model considered UWS injection, droplet wall interaction, wall film formation, liquid phase evaporation, as well as heat conduction and thermal mass on the outer shell and the mixing element. Urea decomposition was modelled using an Arrhenius approach. The authors tried to correlate wall film accumulation and temperature with deposit formation. No information was given about the covered timescale other than that the simulated time was short. The 3 h measurements at $T_e \approx 300^\circ\text{C}$ yielded deposits on both the front, see Fig. 2.16(a), and the reverse side of the mixing element. In contrast, the simulation predicted wall wetting only on the front side, see Fig. 2.16(b). The spray targeting was slightly displaced, and the approach failed to explain why deposit formation was impeded in primary impingement areas. Rudek concluded that improvements were required in the area of chemistry and wall film modelling, in order to enhance the prediction accuracy. The results confirm that deposit locations can be predicted only if the simulation captures the wall film trickling pathways. Generally, however, the consideration of solid cooling is expected to improve the prediction accuracy as evaporation is highly temperature-dependent.

An extension to the model of Rudek [115] was presented by Jäger [116], and additionally considered the formation of biuret in the gas phase. However, the author did not substantially verify the benefit of this modification. Moreover, the approach contradicts the prevalent assumption that biuret forms in the liquid phase, and decomposes upon reaching its melting temperature, see Section 2.2.1. Likewise, biuret sublimation would require solid biuret as a precursor, and its deposition on system walls is improbable in an environment with an average exhaust velocity of 30 m/s. Generally, the consideration of the local concentrations of the involved species, however, appears essential as deposit formation rates are highly concentration-dependent [18, 70].

Among the available methods, Becker et al. [44] presented the most elaborate approach. The authors aimed at predicting deposit formation on a mixing element, based on transient simulations using the commercial CFD code AVL Fire. The model was taken from Birkhold [101, 102] and considered UWS injection, droplet wall interaction, wall film formation, liquid phase evaporation, as well as heat conduction and thermal mass on the outer shell and the mixing element. The covered time was limited to one second, as the authors deemed the timescales of solid cooling too long to be captured by the simulation. The spray surface load (SSL), i.e. the liquid film mass per unit area and time, was adopted to reduce the required simulation time, and taken as a measure for deposit formation. Comparison against measurements at $T_e = 326^\circ\text{C}$ yielded a correlation between deposit formation and the SSL on one out of two blades, compare Figs. 2.16(c) and 2.16(d). The authors concluded that the SSL helped to identify potential deposition locations, although the correlation between the SSL magnitude and deposit formation remained unclear. It was not discussed why the areas with the highest SSL, for the most part, remained free of deposit formation. Equally, it appears questionable whether the method is applicable at temperatures well below the deposition limit, if deposits do not form in the vicinity of primary impingement areas, but further downstream.

In contrast to the comprehensive models described in Section 2.3.1, CFD based approaches are characterised by a massive simplification of the underlying reaction kinetics. Instead, they rely on the identification of precursors of deposit formation and, in return, allow the assessment of actual SCR system geometries. All works acknowledge liquid film as a precursor of deposit formation. The fact that they have been implemented based on existent simulation models for the simulation of ammonia homogenisation facilitates their adoption in an industrial development environment. All models consider UWS injection, droplet wall interaction, wall film formation, as well as evaporation and decomposition approaches for water and urea, respectively. In addition, Rudek [115], Jäger [116] and Becker et al. [44] account for heat conduction, as well as for the thermal mass of the mixer and the outer shell. The described approaches can be seen as a first step in the development of models for the prediction of deposit formation in realistic SCR system geometries. However, the analysis of

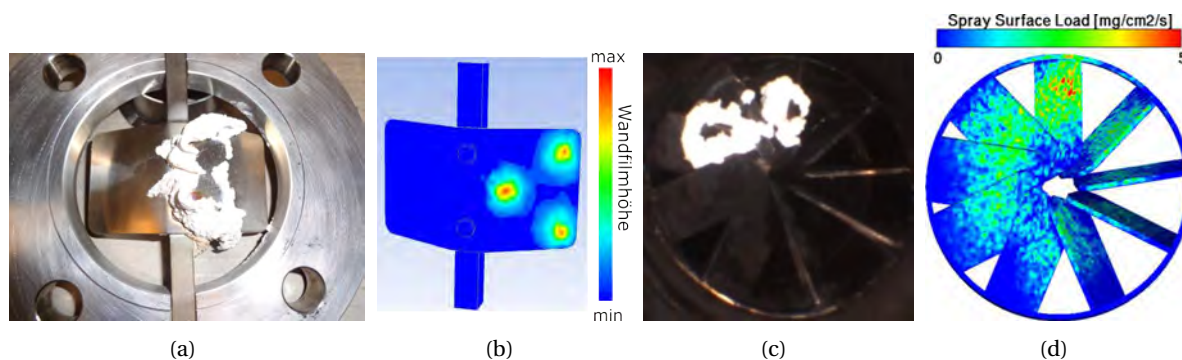


Figure 2.16: Deposit formation after 3 h (a), and simulated wall film thickness (b). $T_e = 300^\circ\text{C}$, $c_e = 30\text{ m/s}$, injection rate \dot{m}_{UWS} not specified. Figures taken from Rudek [115]. Deposit formation after 12 h (c), and simulated surface spray load after 1 s (d). $T_e = 326^\circ\text{C}$, $\dot{m}_e = 340\text{ kg/s}$, injection rate gradually increased to $\dot{m}_{\text{UWS}} = 215\text{ mg/s}$. Figures taken from Becker et al. [44].

weaknesses yields a number of key factors, which will have to be addressed in order to extend the applicability of such models to a broader range of operating conditions. For the correct prediction of deposit formation locations the fluid film pathways need to be captured beyond the single second range. Besides, the realistic development of fluid film pathways and the temperatures at deposit locations depend on the accurate simulation of solid cooling. In order to clarify why deposit formation is impeded in certain areas, further experimental work is necessary to investigate the underlying mechanisms. The correct distinction of such mechanisms will require the interpretation of wall film properties, other than its mere presence. Wall film temperatures and gas phase concentrations of the involved species will be crucial to assess whether a potential deposit could be critical to reliable system operation. Finally, the accurate representation of both UWS spray and spray targeting is a basic requirement to avoid incorrect predictions of the deposit formation risk.

Chapter 3

Research Objectives

Although a number of fundamental correlations between single impact factors and deposit formation have been found, their generalisation and application for the prediction of deposit formation remains a fundamental challenge. The transfer of single correlations from one system to another is impeded not only due to the different experimental boundary conditions but also because of the complex interaction of system design, operating, and boundary conditions. Even though the individual steps between wall wetting and deposit formation are known, their influence on the actual deposition process appears to be neglected for the most part. Often, a lack or limitation of the optical accessibility of areas of interest limits studies to the sole evaluation of whether a deposit has been formed or not. Available methods for the prediction of the deposit formation risk either work with realistic SCR system geometries but oversimplify the underlying physics and chemistry, or they model the chemistry of deposit formation with a decent degree of accuracy but are restricted to reactor environments.

It is the goal of the present work to provide a simulation method which is capable of predicting the deposit formation risk in an automotive SCR system. The method should be capable of capturing the impact of mixing element and mixing section geometry, injector characteristics as well as operating conditions, such as exhaust temperature and injection rate. The simulation of deposit formation in realistic SCR systems under consideration of detailed chemistry still has to be regarded as unfeasible as the timescales which would have to be captured (minutes to hours) are too large to allow their calculation within acceptable timeframes. Therefore, the deposit formation risk shall be determined based on the distribution and the properties of the wall film, which is regarded as a precursor of deposit formation. In order to guarantee straightforward applicability in an industrial environment, the model should be an extension to an existent and validated CFD model for the prediction of ammonia homogenisation. The model has to capture the underlying physics and chemistry in sufficient detail to allow a reliable evaluation of the deposit formation risk within an acceptable timeframe. In this way, it shall support an efficient development and design process of SCR systems by spotlighting areas with high deposition risk and critical operating conditions.

In the first part of this work, the typical locations of deposit formation will be identified based on a typical series SCR system. The obtained data will be used for the verification of simulation results and will help to set up a test rig with versatile optical accessibility which allows the identification of individual mechanisms that promote or impede deposit formation. In addition, the process of deposit formation shall be quantified with respect to deposition temperatures, solidification timescales, growth rates, deposit content and decomposition. The obtained knowledge shall be combined to evaluate the actual severity of individual deposits, i.e. to assess whether a specific deposit can put reliable system operation at risk. This will also imply strategies on how to manipulate the deposit formation risk on a design level.

In the second part of this work, the validated CFD model of Fischer [31, 32], which has been extended and verified in a number of follow-up works by Smith et al. [45, 53, 119] and Zöchbauer et al. [120], is to be used to simulate the preparation of UWS in a set of representative SCR systems. The findings about the mechanisms of deposit formation shall be compiled into a model which can predict the deposition risk based on the physical properties of the wall film. In addition, strategies to speed up the evolution of the wall film pathways will be assessed and applied in order to extend the captured timescales. Eventually, the calibration of the model and its ability to assess the impact of the operating conditions, injector characteristics, as well as the geometry of the mixing element and mixing section, are to be verified.

Chapter 4

Analysis Methodology

4.1 Experimental Setups and Procedures

In order to investigate the mechanisms of deposit formation, the accumulation of deposits was studied under realistic conditions. In addition, chemical analyses were carried out to determine the deposit content and the decomposition behaviour of single deposit components. Operating conditions, measurement equipment and procedures, as well as the individual test bench setups are described in the following sections.

4.1.1 Test Bench Setups and Equipment

Experimental investigations on the formation of deposits were carried out on an engine test bench using a turbocharged 4 cylinder 2.1 l series diesel engine. The engine was equipped with a DOC and a DPF. It was possible to attach and exchange different measurement volumes, using a flange connection. In every case, a DPF was mounted upstream of the respective measurement volume in order to prevent the deposition of soot particles, which was necessary to maintain optical accessibility. The reference exhaust temperature T_e was measured in the centre of the exhaust flow upstream of the point of UWS injection. Deposition was studied in an underbody type exhaust system, an optical volume and a modified close-coupled type exhaust system. A description of the individual experimental setups can be found in Sections 4.1.2 and 4.1.3, which also include detailed information about the applied operating conditions and injector characteristics. The chemical analysis method is described in Section 4.1.4.

Two optical volumes were used throughout the studies presented in this work. Both were realised as welded boxes and manufactured from stainless steel sheets (X5CrNi1810) with a thickness of 2 mm, see e.g. Fig. 4.4(c). Both the front and the back ends of the boxes were equipped with flanges to attach the exhaust piping. All other sides featured large rectangular openings to provide versatile optical accessibility to the measurement volume and to allow sufficient illumination of the investigated blade surfaces. SCHOTT BOROFLOAT[®] 33 borosilicate glasses with a thickness of 5 mm were used to cover the openings. The glass was temperature-stable up to 500 °C and its optical transmission for visible light in the range 380...780 nm exceeded 90 % [121]. The windows were sealed using Würth SUPER-RTV-SILICONE adhesive and sealing compound. The compound was long-term and short-term temperature-stable up to 315 °C and 370 °C [122], respectively. This was sufficient to cover operating conditions in the entire wall wetting temperature range, see Section 2.2.3. Aside from its sealing function, the adhesive also held the windows in their designated position, and compensated

the difference in thermal expansion of the stainless steel body and the glasses. Additional stainless steel masks were attached from the outside, in order to avoid the windows slipping out of position, and against mechanical impacts. The application of spacers helped to avoid tension in the glass when the masks were screwed to the main body of the box. A direct contact between glass and metal was prevented by the silicone adhesive on the one side, and by inserting a (slightly compressible) graphite exhaust gasket on the other side. The upper window was attached to the box with screws and made removable, in order to allow mounting and cleaning of mixing elements, as well as to extract deposit samples. Design aspects specific to the individual experimental setups are discussed in Sections 4.1.2 and 4.1.3.

All experiments were started from a clean, deposit-free system. A steady-state exhaust temperature was maintained before start of injection (SOI) and during the experiments. The formation of deposits was documented using a customary Canon 650D DSLR equipped with a Tamron 28...300 mm zoom lens and an Olympus E-PL5 MILC equipped with a cooled endoscopy lens system. A circular polarising filter was applied in order to remove undesired reflections during recording. A planar LED array was used to illuminate mixing element rear sides, or individual blade elements, in the optical volumes. An endoscopic light source was installed whenever the upstream faces of mixers inside the exhaust piping were investigated.

Experiments were conducted under a broad range of operating conditions. The engine was used to generate exhaust and to control the exhaust temperature T_e and mass flow \dot{m}_e . A separate control unit was employed in order to realise the desired injection strategies, in particular to set the injection rate \dot{m}_{UWS} . Individual operating points were labelled according to the pattern OP $T_e / \dot{m}_e / \dot{m}_{UWS}$. Collected samples were denoted alike.

4.1.2 Series Exhaust Systems

Initial basic investigations on deposit formation were conducted on a passenger car underbody type series SCR system. The system was set up at the test bench according to Fig. 4.1. Injection was realised with an S-bend pipe injector mounting using a 16° 3-hole series injector with an SMD of $100\ \mu\text{m}$, Tab. 4.5 and Fig. 4.7. The injection rate was controlled by adapting the pulse length while the pulse frequency was maintained constant at 3 Hz. The mixing section was equipped with a static mixing element and an SCR catalyst, see Figs. 2.5(a), 4.4(a) and 4.6.

A series of separate measurements were undertaken in order to assess deposit growth as a function of time. The experiment duration was varied while maintaining exhaust temperature and mass flow as well as the injection rate constant, Tab. 4.1. After completing the specified experiment duration, injection was suspended, the system was shut down immediately, and the mixing pipe was dismounted for documentation. A second parameter study was carried out to document the temperature-dependency of both the deposit weight and locations. The exhaust temperature was varied while maintaining exhaust mass flow, injection rate and experiment duration constant, Tab. 4.1. When the

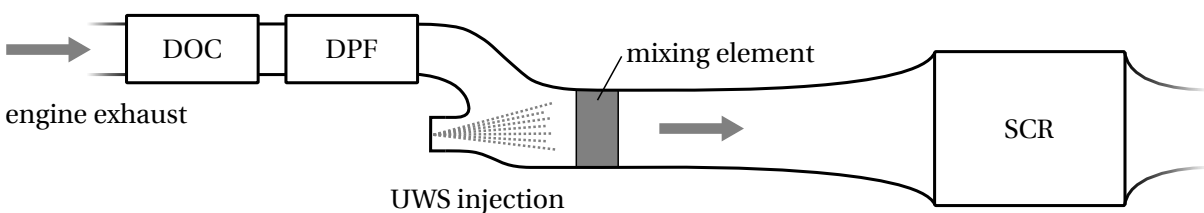


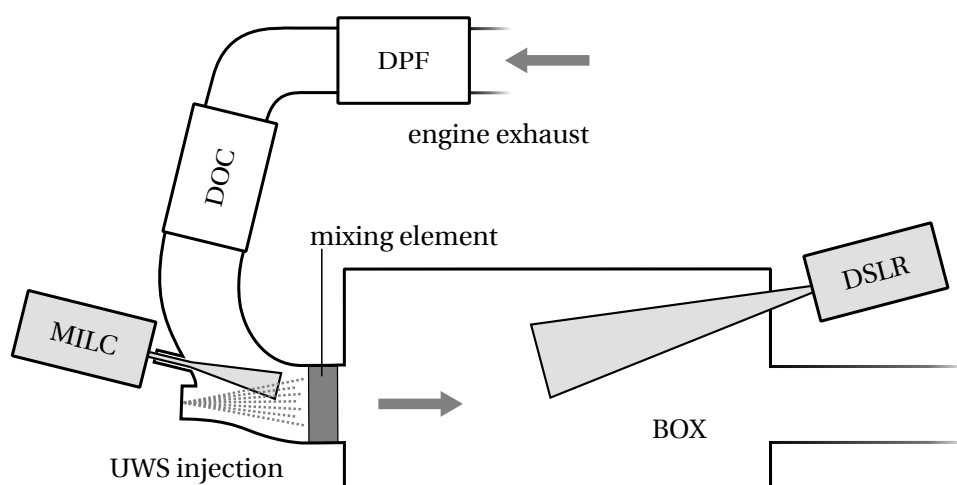
Figure 4.1: Simplified schematic of the test bench setup for the investigation of deposit formation in an underbody type SCR system.

Table 4.1: Operating conditions for the investigation of deposit formation in an underbody type and a close-coupled type SCR system.

Operating point	Unit	Underbody SCR	Underbody SCR	Close-coupled SCR
Exhaust temperature	[°C]	200	200, 220, 240	275
Exhaust mass flow	[kg/h]	100	100	170
UWS injection rate	[mg/s]	13	35	35, 60
Experiment duration	[min]	15, 30, 60, 120	240	90

predefined experiment duration had been completed, injection was suspended, the system was shut down immediately, and the mixing pipe was dismantled for documentation. Injector and mixing pipe were weighed separately on a Sartorius Master^{PRO} LA8200S precision balance. The balance featured a readability of 0.01 g and a repeatability of $\leq \pm 0.01$ g [123]. The deposit weight was obtained by comparing the difference in weight of the system before and after the experiments.

The impact of the spray characteristics and the mixing element geometry on deposit formation was studied on a passenger car close-coupled type SCR system. The system was investigated with two oval-shaped swirl mixers: mixer 1 was characterised by short rear blade elements with an inclination angle of approx. 50° whereas mixer 2 was characterised by long rear blade elements with an inclination angle of approx. 70°, Fig. 4.6. Both exhaust systems were truncated at the downstream end of their mixing elements, Fig. 4.2. An optical volume was attached in order to allow visual access to the rear side of the mixers, see Section 4.1.1. The inner dimensions of the box were chosen as large as necessary to incorporate the flanges, to maintain the windows virtually free of wall wetting, and to allow the observation of the downstream faces of the mixer blades from a flat angle. Endoscopy mounts were installed to provide visual access to the upstream side of the mixers. Endoscopic light sources and optics were applied to realise illumination and video recordings while minimising the impact on the exhaust flow. Injection was realised with either a 42° hollow cone injector with an SMD of 51 μm or a 26° 6-hole injector with an SMD of 97 μm , Tab. 4.5 and Fig. 4.7. The hollow-cone injector featured a constant pulse length of 1.6 ms and the injection rate was controlled by adapting the pulse frequency. In case of the 6-hole injector, the pulse frequency was maintained constant at 3 Hz and the injection rate was adjusted by adapting the pulse duration.

**Figure 4.2:** Simplified schematic of the test bench setup for the investigation of deposit formation in a close-coupled type SCR system.

A parameter study was carried out to document the dependency of deposit accumulation and location on the used mixer, injector and injection rate. The injection rate was varied while maintaining exhaust mass flow and temperature as well as the experiment duration constant, Tab. 4.1. All possible combinations of the two mixers and injectors were investigated.

4.1.3 Surrogate Mixing Element Geometry

The mechanisms of deposit formation were investigated on a mixing element geometry. A volume with optical access was built up in order to provide full optical access to the areas exposed to deposit formation. It was installed instead of the mixing element, mixing section and SCR catalyst, Fig. 4.3. The inner dimensions of the box were chosen as large as necessary to incorporate the flanges and an additional injector dome, a variable mounting for blade elements, to maintain the windows virtually free of wall wetting, and to allow the observation of the downstream faces of the blade elements from a flat angle. Single blade elements were manufactured from stainless steel (X5CrNi1810) sheets with a thickness of 1 mm, imitating the geometric features of the original mixing element geometry in terms of characteristic lengths, bend angles, and radii, as well as surface properties, compare Figs. 4.4(a) and 4.4(b). Both the inner and outer edges of the blade elements were gently deburred, but not chamfered, in order to imitate the sharp, laser-cut, edges of the original mixer. The elements were combined and mounted on threaded rods to yield a surrogate mixing element, Fig. 4.4(c). The individual elements were installed at a distance of approx. 13 mm to realise the blade spacing of the reference mixer. A realistic spray targeting, in particular realistic droplet impact incidence angles, was achieved by tilting the blades at an angle of approx. 22° to the central axis of the inlet flow pipe of the optical volume. The optical volume was connected to the original s-bend pipe, using a flange connection. Furthermore, it was rotated 30° around the central axis in order to realise incident flow conditions similar to the original mixing element. UWS was injected using a 16° 3-hole series injector with an SMD of $100\ \mu\text{m}$, Tab. 4.5 and Fig. 4.7. It was mounted on the optical box instead of the S-bend in order to maintain a distance of approx. 100 mm between the points of injection and impingement, as in the original setup, compare Figs. 4.1 and 4.3.

A parameter study was carried out to document the mechanisms of deposit formation and accumulation as well as to obtain deposit samples. The exhaust temperature was varied over the entire wall wetting temperature range, and experiments were conducted at two different exhaust mass flow rates, Tab. 4.2. The injection rates were varied in such a way that deposit formation occurred on the blades of the mixing element. Net injection duration was 65 min, after which injection was discontinued

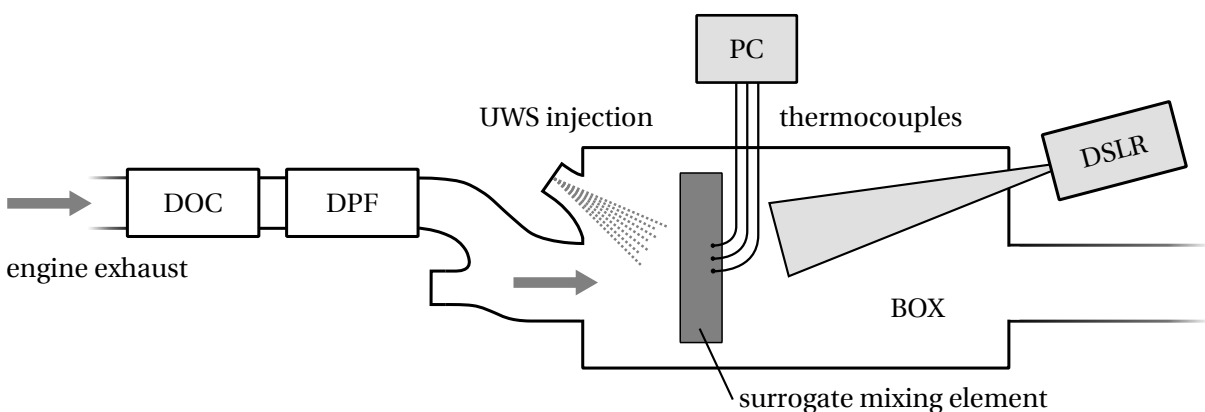


Figure 4.3: Simplified schematic of the test bench setup for the investigation of deposit formation on a surrogate mixing element geometry.

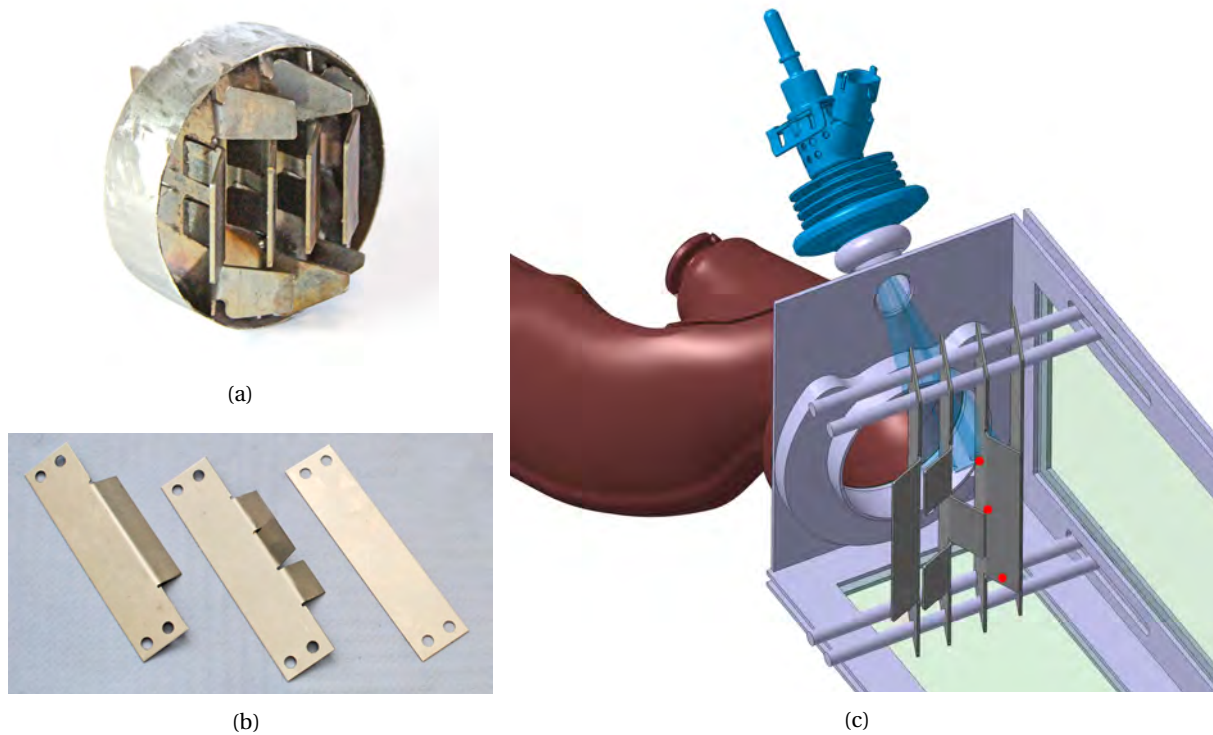


Figure 4.4: Mixing element of the underbody type series exhaust system (a, rear perspective), single blade elements (b), and optical volume created for the investigation of deposit formation on a surrogate mixing element geometry (c, simplified, top and left side hidden). Locations of thermocouples highlighted in red: area of impingement (1, top), UWS trickling path (2, middle), accumulation area (3, bottom). Thermocouples installed on reverse blade side.

and the engine was shut down immediately. Deposits were removed from the blades of the mixing element and stored in air-tight containers to prevent the absorption of ambient humidity.

Temperatures were measured at three different locations: the area of impingement (1), along the trickling path of the UWS (2) and at the wall film accumulation area (3). The thermocouples were mounted on the reverse sides of the blade element exposed to wall wetting as to avoid alteration of the liquid film pathways. Due to the low thickness and the high thermal conductivity of stainless steel, the temperature gradient between the two blade faces can be regarded as negligible on timescales in the single second range [32, 101, 124]. Using a measurement frequency of 2 Hz, the signal was expected to represent the average temperature at the measurement locations with good accuracy. The temperature of the impingement area was averaged over a 30 s period just before start of injection

Table 4.2: Operating conditions for the investigation of deposit formation on a surrogate mixing element geometry.

Operating point	Unit	OP T_e / \dot{m}_e / \dot{m}_{UWS}
Exhaust temperature	[°C]	200...335
Exhaust mass flow	[kg/h]	100, 200
UWS injection rate	[mg/s]	3.3...120
Experiment duration	[min]	65

(SOI) and was used as a reference for the temperature level of the mixing element. It was denoted $T_{m,SOI}$ and ranged between 185 °C and 310 °C. The steady-state injection temperature was averaged over a 300 s period just before the end of injection (EOI) and denoted $T_{m,EOI}$. The impact of minor temperature drifts on the calculation of temperature drops was eliminated by subtracting the deviation between the instantaneous and the reference exhaust temperature from the measured value. Deposits typically formed between the thermocouples (2) and (3). Their exact location was determined based on the video recordings. The temperature at the deposit location was linearly interpolated between the respective thermocouples.

The following wall wetting regimes were optically distinguished in the area of impingement during the measurement campaign:

- **Permanent wall wetting** was assumed if a non-zero fraction of the impinging UWS remained on the mixer blades permanently.
- **Intermittent wall wetting** was assumed if the impinging UWS evaporated prior to the next impingement event.
- **Leidenfrost effect** was assumed if the impinging UWS did not result in visible wall wetting. This regime was typically accompanied by a clearly visible burst of secondary droplets.
- **Transitional wall wetting** was assumed if the wall wetting behaviour periodically alternated between permanent and intermittent wall wetting.
- **Leidenfrost transition** was assumed if the wall wetting periodically alternated between intermittent wall wetting and Leidenfrost effect. In this case, the wetted area was smaller compared to pure intermittent wall wetting and the UWS spread in the form of small streaks rather than distinct areas, indicating its detachment from the wall. As in case of the pure Leidenfrost effect, this regime was typically accompanied by a clearly visible secondary droplet burst.

Impingement and other wall wetting areas were identified by image subtraction of the surface before and during UWS injection.

The solidification timescale t_s was defined as the time between SOI and the formation of a deposit nucleus. In case the Leidenfrost effect was observed at the beginning of the experiment, the point of initial wall wetting was taken as a reference instead of SOI. The actual Leidenfrost temperature, or Leidenfrost point, was assumed as the temperature at the point of inflection of the measured temperature curve after which a distinct (second) temperature drop was observed. The values were determined according to the method described by Fest-Santini [106]. Typically, a temporal offset was apparent between the formation of a deposit nucleus at t_s and the beginning of noticeable accumulation. Therefore, the solidification temperature T_s , at which the UWS was converted into a deposit, was averaged over a period of 240 s. If the process was exceptionally slow, the averaging period was extended to 1200 s.

Deposit accumulation was assessed optically 60 min after SOI by comparison against a reference. The dimensionless deposit growth number was introduced and denoted dg . Deposits were classified based on a scale with six levels, where 1 corresponded to slow growth resulting in a small deposit and 6 corresponded to intensive growth resulting in a deposit with a thickness exceeding half the distance between two blades (approx. 7 mm), Fig. 4.5. Only major deposits were used for the evaluation. This included deposits which were formed alongside the liquid film pathways, i.e. at or in between the thermocouple locations. Minor solidification frequently occurred at wall film pathway flanks, compare e.g. pathway above red circle in Fig. 4.5(d). However, as it did not grow over time, it was not taken into account.

Another measurement campaign was conducted in order to determine the deposition limit more precisely, i.e. the temperature above which wall wetting is omitted. Experiments were conducted at exhaust mass flows of 100 kg/h and 200 kg/h. Steady state temperatures of the area of impingement (1)

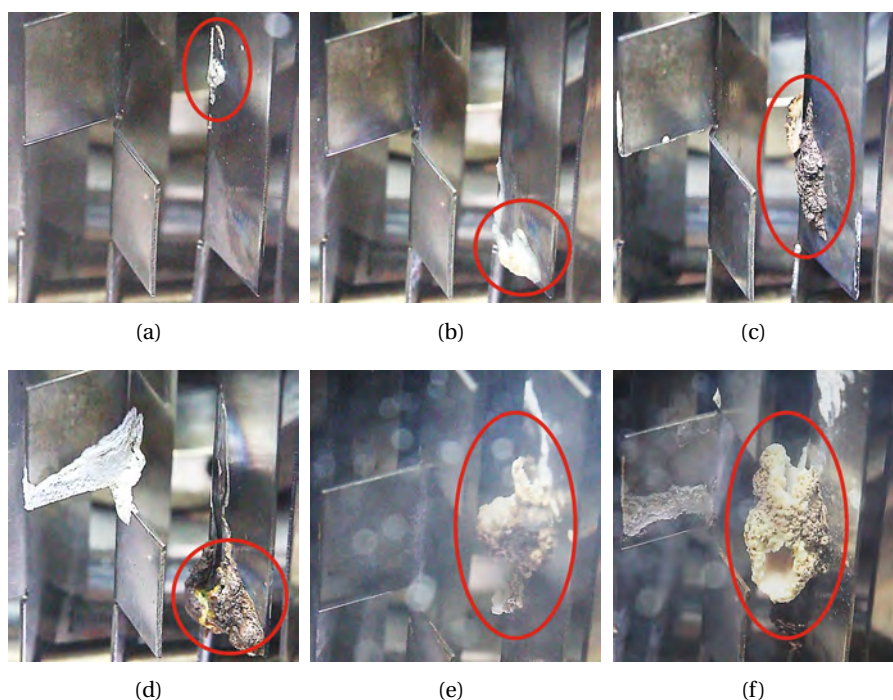


Figure 4.5: Reference measurements for the assessment of deposit accumulation based on a scale with six levels ranging from 1 (a, slow growth, OP 200/200/3.3) up to 6 (f, intensive growth, OP 315/205/75). Respective deposits highlighted in red.

Table 4.3: Operating conditions for the investigation of the deposition limit on a surrogate mixing element geometry.

Measurement series	Unit	Series 1	Series 2	Series 3	Series 4	Series 5	Series 6
Exhaust temperature	[°C]	163...323	173...353	173...351	185...333	185...332	195...330
Exhaust mass flow	[kg/h]	100	100	100	200	200	200
UWS injection rate	[mg/s]	13	25	35	13	25	35
Experiment duration	[s]	180	180	180	180	180	180

before SOI ranged from approx. 160 °C to 320 °C and 185 °C to 330 °C, respectively. Three different injection rates were investigated, Tab. 4.3, and 13 to 16 points were measured in each measurement series. The typical experiment duration was approx. 180 s. The temperatures $T_{m,SOI}$ and $T_{m,EOI}$ of the impingement plate before and during steady state injection were averaged over a 10 s period before SOI and EOI, respectively. The measured temperature drop ΔT_m was then determined as

$$\Delta T_m = T_{m,SOI} - T_{m,EOI} \quad (4.1)$$

and shall be representative for the cooling performance.

4.1.4 Deposit Content and Decomposition

The reference substances urea, biuret, cyanuric acid, ammelide, ammeline and melamine were obtained from Sigma-Aldrich Handels GmbH, Vienna, Austria, and used without further purification. The minimum reagent purity was $\geq 98\%$. Biuret, ammelide, ammeline and melamine were provided

in the form of powders. Urea, cyanuric acid, and deposits were grinded and mixed in order to yield homogeneous samples in powdery form. The samples were analysed on a Netzsch TG 209 C thermogravimetric analyser. Pure nitrogen was used as purge gas with a constant flow rate of 50 ml/min. An Al_2O_3 crucible was used for all experiments. During the respective measurement campaigns the sample weight was maintained within the range of $\pm 5\%$ of the average value in order to minimise an impact on the result.

The deposit content was analysed by comparing the decomposition behaviour of the samples against that of the reference substances, Fig. 5.16. 3.9 mg of sample were heated from room temperature to 800 °C at 10 °C/min. Several critical temperatures were identified based on the TGA measurements, Tab. 5.2. A mass loss of $\geq 2\%$ was used to identify the start of decomposition. In the case of urea, biuret, cyanuric acid, ammelide and melamine, the initial sample weight was used as a reference. In case of ammelide, the residual mass at 250 °C, prior to the beginning of the main decomposition stage, was taken as a basis. Any prior decomposition must have been due to a minor contamination of the sample (the purity of the reagent was specified as $\geq 98\%$). A mass loss of $\geq 8\%/^\circ\text{C}$ was assumed to identify decomposition at noticeable rates. Sample depletion was assumed when the residual weight had dropped to 1 % of the original mass. A representative set of deposit was analysed in order to obtain information about the entire solidification temperature range. Only such deposits were chosen that were formed on the reverse sides of the thermocouple locations in order to avoid uncertainties related to their formation temperature.

The decomposition timescales were analysed by pyrolysing a selection of the reference substances at varying temperature levels. 2.6 mg of sample were heated to the desired temperature with a heating rate of 100 °C/min. The target temperature was then maintained for 60 min. Sample depletion was assumed when the residual weight had dropped to 1 % of the original mass and the corresponding time was noted, Tab. 5.4. The heating period was excluded from the decomposition time. In case depletion was not achieved within less than 60 min, the residual weight was listed.

4.2 Simulation Models and Procedures

The preparation of the UWS inside the SCR systems was simulated with the commercial CFD code STAR-CD 4.16 [125]. A validated CFD model was used in this work as proposed by Fischer [31, 32] and extended by Smith et al. [45]. Both the model and the simulation procedure are described in the following sections.

4.2.1 Numerical Framework

Both the underbody type and the close-coupled type SCR system were simulated in this work, see Section 4.1.2. In the case of the underbody SCR system the DPF outlet was used as inlet boundary. The CFD domain included the S-bend injection pipe, mixer and mixing section as well as the SCR catalyst, Fig. 4.6. In analogy to the test bench setup the outlet boundary was set up at the end of the exhaust pipe downstream the catalyst. The close-coupled type SCR system was set up in an analogous manner. However, the DOC outlet was used as inlet boundary and the setup featured an elbow injection, Fig. 4.6. In any case, the UWS spray was targeted directly onto the mixing element. The mixing length between mixer and catalyst intake was roughly 450 mm and 150 mm with regards to the underbody and close-coupled type SCR system, respectively.

Both SCR systems were meshed using polyhedral cells, maintaining a maximum cell base size of 2.8 mm. This was in line with the approach of Fischer [31,32] and in close agreement with the findings of Bhattacharjee et al. [126] concerning mesh insensitivity with respect to ammonia homogenisation



Figure 4.6: CFD domains for the simulation of UWS preparation: underbody type (centre) and close-coupled type SCR system with mixer 1 (top right) and mixer 2 (bottom left). The systems not to scale, mixers and SCR catalysts are shown in grey.

and UWS preparation. The meshes were refined in the areas of the mixing elements and the injection domes. A prism layer was included in order to ensure accurate simulation of the thermal and fluid-dynamic boundary layer. The thickness of the prism layer was adjusted to maintain y^+ in the range 30...300. A standard wall function formulation [125] was used. Both the mixing elements as well as the pipe walls were meshed with solid cells in order to consider their thermal behaviour. A conformal mesh was guaranteed at the interface between the fluid and solid cell layers. A summary of the grid sizes can be found in Tab. 4.4. The catalyst substrates were modelled as porous media by adding an additional force $\mathbf{F}_p = -\mathbf{K} \cdot \mathbf{v}$ to the momentum conservation equation, where \mathbf{K} represented the porous resistance tensor and \mathbf{v} was the superficial velocity [125]. The three mutually-orthogonal directions of the porous resistance tensor were defined as

$$K_{ii} = \alpha_i |\mathbf{v}| + \beta_i \quad (4.2)$$

where α_i and β_i were model coefficients with the dimensions kg m^{-4} and $\text{kg m}^{-3} \text{s}^{-1}$ (note that a summation was not implied by the repeated subscripts). Porosity coefficients for the main flow direction (catalyst channels) were calibrated against measurement data to model backpressure and adjusted for the lateral directions in order to mimic flow straightening by the catalyst channels, Tab. 4.4.

The SIMPLE algorithm was used in both steady-state and transient simulations. The residual error tolerances were set to 0.01 for all solution variables except the pressure, for which it was set to 0.001. A fully-implicit Euler scheme was used for temporal discretisation. Spatial discretisation was realised using the (first order) upwind differencing (UD) scheme for enthalpy and a blend between UD and (second order) central differencing (CD) for density (blending factor 0.7) [125]. A multi-dimensional (second order) monotone advection and reconstruction scheme (MARS) was applied for momentum, turbulence and scalars as Fischer [31,32] showed that using (first order) UD effected an unacceptable level of numerical diffusion. In comparison the MARS scheme, the induced inaccuracies became apparent in the non-physical intensification of scalar transport and a significant reduction of the tur-

bulence quantities in the mixing section. The discretisation settings used in this work are consistent with the best practice setup proposed by Fischer [32] and have been used in all subsequent works of the author [45, 53, 119].

A steady-state simulation of the flow field was conducted for each operating point and used to initialise transient runs. In order to capture the dynamics of the liquid phase and species mixing, transient simulations were conducted. Following the suggestion of Fischer [32], the time step was set to 0.2 ms during periods involving droplet motion within the CFD domain and the steepest gradients during the initial phases of wall film formation and evaporation. Otherwise, the time step was set to 1.0 ms if not otherwise specified. Fischer regarded this procedure as an excellent compromise between tracking droplets precisely and coping "with the gap in timescales of fast droplet dynamics and relatively slow liquid film dynamics" [32].

4.2.2 Gaseous Phase

Hot air represented the exhaust gas. Molecular viscosity, specific heat capacity, and thermal conductivity were taken from [127]. The temperature-dependent fluid properties were fitted with polynomial functions, whereas the gas density was calculated using the ideal gas equation. The inlet boundary was set up based on the exhaust temperatures and mass flow rates provided in Tab. 4.1. The inlet flow velocity was determined using the continuity equation and by estimating the inlet gas density based on the ideal gas equation. A pressure boundary condition was defined at the outlet of the solution domain in accordance with the test bench setup, assuming an ambient pressure of 101 300 Pa. Additional scalar transport equations were solved for water vapour and an ammonia/isocyanic acid vapour representative. In terms of material properties water vapour and ammonia vapour were assumed, following the suggestion of Fischer [32]. While molecular viscosity, specific heat capacity and thermal conductivity were taken from the CHEMKIN database of STAR-CD, density and binary diffusion coefficients were specified according to [127]. As diesel combustion exhaust contains water vapour, a baseline concentration was specified at the inlet boundary based on measurement data from the engine test bench. Other chemical species obtained from the diesel combustion process were not considered. The choice of scalars, as well as their thermodynamic properties, will be discussed in Section 4.2.3.

The transport of gaseous scalars in turbulent flow fields is primarily driven by convection and turbulent eddies which underlines the importance of covering the impact of turbulence accurately. Zöchbauer et al. [120, 128, 129] showed that the flow field in a typical underbody SCR system was predicted very well, regardless of whether it was solved using a Reynolds averaged Navier Stokes (RANS) or a Large Eddy Simulation (LES) approach. However, in contrast to the LES model, all investigated RANS based approaches underestimated the turbulent kinetic energy (TKE). Yet, the computational effort

Table 4.4: Grid sizes of the simulated SCR system geometries and porosity coefficients for the main flow direction (catalyst channels). $[\alpha] = \text{kg m}^{-4}$ and $[\beta] = \text{kg m}^{-3} \text{ s}^{-1}$.

SCR system geometry	Cell count in Mio. cells				Porosity coefficients	
	Fluid	Porous	Solid	Total	α	β
Underbody / 3-hole injector	2.234	0.117	1.024	3.376	97.876	1769.77
Close-coupled / mixer 1 / h.c. inj.	1.883	0.101	1.343	3.327	272.711	791.65
Close-coupled / mixer 1 / 6-hole inj.	1.900	0.094	1.362	3.356	272.711	791.65
Close-coupled / mixer 2 / h.c. inj.	1.618	0.099	1.150	2.867	272.711	791.65
Close-coupled / mixer 2 / 6-hole inj.	1.609	0.100	1.144	2.853	272.711	791.65

associated with LES calculations remained too high to cover timescales in the double-digit second range within reasonable time. In RANS based approaches, turbulent scalar transport is modelled in analogy to molecular diffusion by using an artificial viscosity, the turbulent viscosity μ_t , which is defined as $\mu_t = C\rho k^2\varepsilon^{-1}$, where k and ε are the turbulent kinetic energy and dissipation, respectively. k - ε models solve a transport equation for both quantities which implies the assumption of isotropic turbulence. However, this is invalid in SCR systems, especially in sections with strong swirling flows [31, 32, 128]. It is widely accepted that RSM models can produce more precise solutions in such cases [130, 131], as they account for the anisotropy of the Reynolds stresses, i.e. of the velocity fluctuations [31, 32, 128]. RSM models solve one transport equation for the turbulent dissipation and six for the Reynolds stresses [131, 132]. The turbulent kinetic energy is calculated based on these Reynolds stresses using an algebraic equation. Following the suggestion of Fischer [31, 32], the RSM model with the Speziale, Sarkar and Gatski approximation for the pressure-strain term (RSM/SSG) [125] was used throughout this work. In comparison with k - ε and k - ω SST models, it was shown to yield the highest turbulent viscosity [31, 32, 120]. Despite this, it underestimated ammonia homogenisation [31, 32] due to the fact that the level of TKE was still underpredicted. As turbulent diffusive scalar transport is assumed proportional to the turbulent viscosity and indirectly proportional to the turbulent Schmidt number Sc_t [125, 131, 133], Fischer [31, 32] compensated the underestimation of turbulent diffusion by lowering Sc_t to 0.15. The applicability of this empirical calibration has been confirmed for common SCR system layouts [45]. Therefore, the application of the RSM/SSG model in combination with the Schmidt number adaptation to $Sc_t = 0.15$ can be seen as the best compromise between accuracy and computational effort to cover timescales exceeding the single-digit second range.

4.2.3 Liquid Phase

The description of the liquid phase requires modelling UWS spray and decomposition as well as droplet wall interaction and wall film. A brief overview of the chosen approaches will be given in the following sections.

UWS Spray

The propagation of the UWS spray was described with a discrete droplet model (DDM) approach, allowing the correct prediction of droplet motion including heat and mass transfer with acceptable numerical effort [134]. In this Euler-Lagrangian type framework, the spray was represented by stochastic particles, the so-called parcels [57]. Each parcel was considered representative for a droplet group and was characterised by a set of properties including droplet diameter, temperature, velocity, and instantaneous trajectory, as well as the number of contained droplets. Conservation equations for mass, momentum and energy were solved individually for each of the parcels [125]. The model considered the effects of drag, buoyancy and turbulent dispersion, being the most vital ones to guarantee an accurate prediction of droplet motion [32, 57, 134]. Two-way coupling between the dispersed phase and the background phase was applied for momentum and heat. Based on a sensitivity study, Bhat-tacharjee and Haworth [126] reported only very little impact on their results if the number of parcels was raised above 10000 per second. In the present work, a good statistical representation of the spray and sufficient discretisation insensitivity was ensured, as the number of injected parcels exceeded 30000 per second in any case [32, 126].

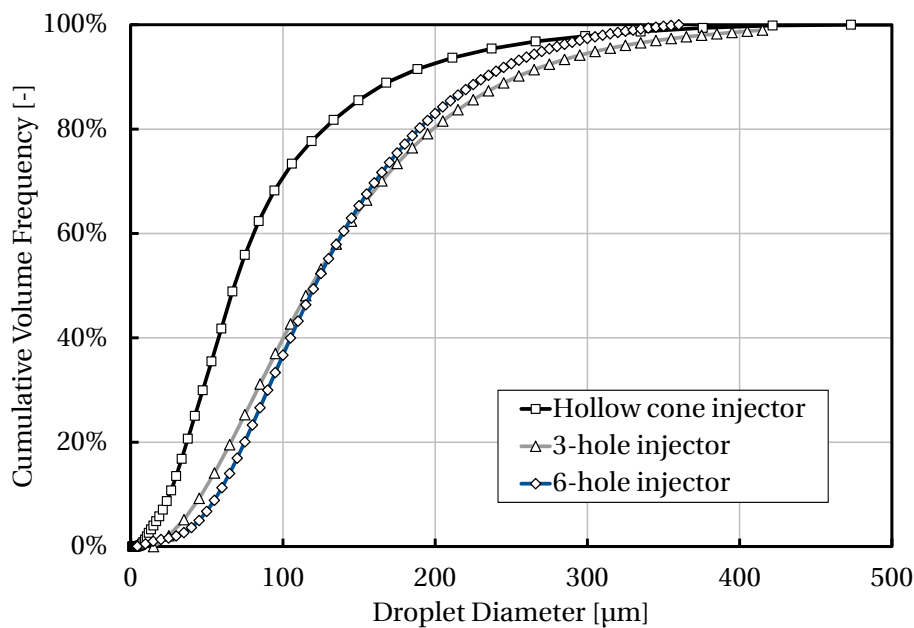
Primary breakup, i.e. the transition of the injected UWS from a continuous phase at the nozzle outlet into a dispersed phase within the carrier fluid, was not considered. Instead, the spray was initialised based on measured droplet spectra and injector characteristics, Tab. 4.5 and Fig. 4.7, which has become common practice in SCR system modelling [32, 37, 126, 134, 135]. The fact that these spectra were measured at room temperature led to concerns regarding the validity of the initialisation in

Table 4.5: Summary of injector characteristics based on manufacturers data.

Injector	Unit	Hollow cone	3-hole	6-hole
Injector beams	[-]	1	3	6
Supply pressure (relative)	[bar]	0	5	5
Cone angle from visualisation	[°]	42	16	26
Cone angle of single beams*	[°]	42	8	7
Spray angle**	[°]	0	6	9
Droplet injection velocity	[m/s]	32	24	24
Sauter mean diameter	[μm]	51	100	97
Static mass flow rate	[kg/h]	8.0	3.15	5.0

* Inner cone angle of hollow cone injector 14.5°

** Angle between central beam axes and central injector axis (polar angle)

**Figure 4.7:** Overview of spray characteristics based on manufacturers measurements.

case of injection into hot exhaust. In order to verify whether this approach was sufficiently accurate, Smith et al. [45] measured the size distribution approx. 130 mm downstream the point of injection, and found that the spectra obtained at 276 °C and 334 °C were very similar to reference measurements at room temperature. Furthermore, the analysis of spectra obtained from CFD yielded that droplet evaporation had a negligible effect on the spray prior to impingement on the mixing element. Therefore, the initialisation of the droplet size distribution in CFD with data gained at room temperature was deemed both valid and sufficient. Secondary breakup was not considered, as its contribution to spray atomisation was expected to be minimal [37, 45, 136, 137].

UWS Decomposition

UWS was modelled as a two-component fluid, consisting of water and urea. Mixing processes within the droplet were described with the rapid mixing model (RM) which has been confirmed as a suitable model for UWS decomposition, both with respect to accuracy and computational efficiency [32, 101, 138]. The thermodynamic liquid phase properties were specified as a function of temperature and

Table 4.6: Modelling approaches for the liquid properties of both lagrangian phase and wall film.

Property	Unit	$f(T)$	$f(Y_{\text{urea}})$	Source	Approach
Density	[kg/m ³]	✓	✗	UWS [111]	polynomial
Viscosity	[kg/m s]	✓	✗	water [127]	polynomial
Surface tension	[N/m]	✓	✗	water [127]	polynomial
Thermal conductivity	[W/m K]	✓	✗	water [127]	polynomial
Specific heat capacity	[J/kg K]	✓/✓	✓	water [127], urea [113]	polynomials
Heat of evaporation	[J/kg]	✓/✗	✓	water [127], urea [101]	polynomial/const.
Vapour pressure	[Pa]	✓/✓	✓	water [127], urea [101]	Antoine equations

urea concentration whenever possible. Following the suggestion of Fischer [32], UWS with 32.5 wt % was taken as a basis for the definition of the density, while the properties of pure water were assumed for viscosity, surface tension and thermal conductivity, Tab. 4.6. Specific heat capacity, heat of evaporation and vapour pressure were specified individually for water and urea, and hence determined depending on the local instantaneous urea concentration, Tab. 4.6. As with water, an evaporation approach was chosen to model urea decomposition instead of an Arrhenius-based approach, following the recommendation of Abu-Ramadan et al. [138]. Evaporation and thermolysis of urea, Eq. (1.1), were described as a single step process by lumping together the respective enthalpies which were assumed constant [32, 101]. The vapour pressure curve of urea was taken from Birkhold [101] and equally accounted for the impact of both evaporation and thermolysis. Boiling and evaporation were considered for both components and using the saturation temperature T_{sat} of the mixture as a threshold [125]. The saturation temperature was calculated based on the actual urea concentration using Raoult's and Dalton's law.

The gaseous species generated during UWS decomposition were represented by active scalars for water vapour and for the ammonia/isocyanic acid vapour. The formation and propagation of isocyanic acid was not modelled individually. Fischer [32] justified this approach based on the assumption that ammonia and isocyanic acid were transported alike by the turbulent flow field. FTIR measurements of the local NH_3 and HNCO concentrations at the downstream end of a mixing pipe confirmed this assumption [124]. Assuming one active scalar as a representative for both thermolysis products also entailed neglecting any gas phase hydrolysis of isocyanic acid, Eq. (1.2). However, this can be regarded as feasible since HNCO remains fairly stable in the gaseous phase up to temperatures in the range 700...1000 °C for several seconds [19, 75]. Besides, its hydrolysis has been reported to be of subordinate importance in the absence of a suitable catalyst and, in particular, at temperatures below approx. 400 °C [15, 19, 20, 139]. On the catalyst substrate, the hydrolysis of isocyanic acid proceeds at very high rates [19]. Under the assumption of equimolarity, the (identical) amount of substance of NH_3 and HNCO can therefore be determined in postprocessing.

Fischer [32] validated the UWS decomposition model by simulating the evaporation of single UWS droplets in a quiescent environment. The characteristic two-step evaporation was predicted very well. The evaporation timescales for water and urea correlated very well with the results of the simulation approaches of Kontin et al. [113] and Birkhold [101]. Agreement with measurement data was deemed sufficient as the prediction accuracy was not perfectly consistent over the whole temperature range. Apart from the impact of the respective experimental setups, Fischer [32] attributed this to the fact that various modelling assumptions were based on aspects of the complex phase change and decomposition chemistry which were still unclarified and are subject to current research. In this context, the UWS droplet decomposition model was deemed a very good compromise between computational efficiency and sufficient precision.

Droplet Wall Interaction

The injection of UWS spray into the exhaust almost inevitably results in droplet impact on the walls of the system. In fact, interaction is usually enforced intentionally by installing mixing elements as primary impingement targets in order to both accelerate UWS decomposition and enhance species mixing. A multitude of different droplet wall interaction regimes has been documented, Fig. 4.8. Besides, droplets may impact on the catalyst substrate. Common impingement models describe the outcome of droplet wall interaction based on a set of (dimensionless) characteristic parameters [99, 100, 140, 141]. In the present case, an adapted Bai Gosman impingement model [99] was applied, as suggested by Fischer [32] and extended by Smith et al. [45]. The following paragraphs briefly describe the adaptation and calibration of critical boundaries for the use with UWS droplets in common SCR systems, as shown in Fig. 4.6.

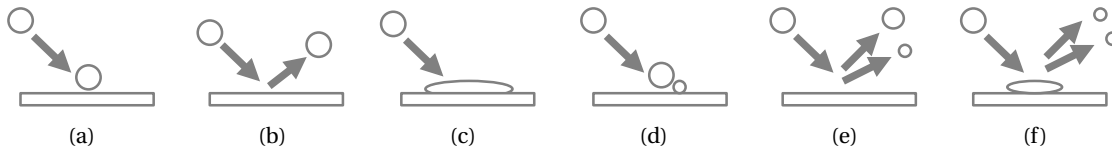


Figure 4.8: Schematic overview of common droplet impact regimes: stick (a), bounce (b), deposition (c), breakup (d), breakup and rebound (e), deposition and splash including partial deposition (f). Adapted from Bai et al. [100].

Bai and Gosman [99] used a deposition limit temperature in order to distinguish between wetting and non-wetting droplet wall interaction regimes. However, the deposition limit is not necessarily a sharp and constant boundary. Following the suggestion of Smith et al. [45], a transition regime was implemented in place of the sharp deposition limit temperature which blended between wetting and non-wetting droplet wall interaction regimes, Fig. 4.9. The corresponding temperature thresholds were denoted upper and lower deposition limit temperature $T_{DL,u}$ and $T_{DL,l}$, respectively, and related by using a constant temperature offset ΔT_{trans} :

$$T_{DL,l} = T_{DL,u} - \Delta T_{trans} \quad (4.3)$$

which was denoted Leidenfrost transition temperature margin. The number of impinging parcels which experienced a Leidenfrost effect n_{LF} versus the overall number of impingement events, n_{imp} , was denoted deposition ratio dr :

$$dr = n_{LF} / n_{imp} \quad (4.4)$$

For every impingement event in the transition regime, the actual ratio was determined, based on the local wall temperature using a linear interpolation between the threshold temperatures. Subsequently, a random number in the range 0...1 was generated and compared to the deposition ratio. Based on the outcome, the droplet behaviour was determined by assigning the respective interaction regime, see Fig. 4.9. The upper deposition limit was defined as a function of the droplet saturation temperature using a constant temperature difference of ΔT_{DL} :

$$T_{DL,u} = T_{sat} + \Delta T_{DL} \quad (4.5)$$

As a consequence, the deposition limit was dependent on the actual urea concentration via the saturation temperature. Above the deposition limit, single droplets were completely evaporated upon impact in order to model partial droplet evaporation due to the Leidenfrost effect. The remaining droplets were treated by the impingement model as before. The droplet fate was determined just as in case of the deposition ratio. Accordingly, the fraction of non-wall-wetting droplet impingement

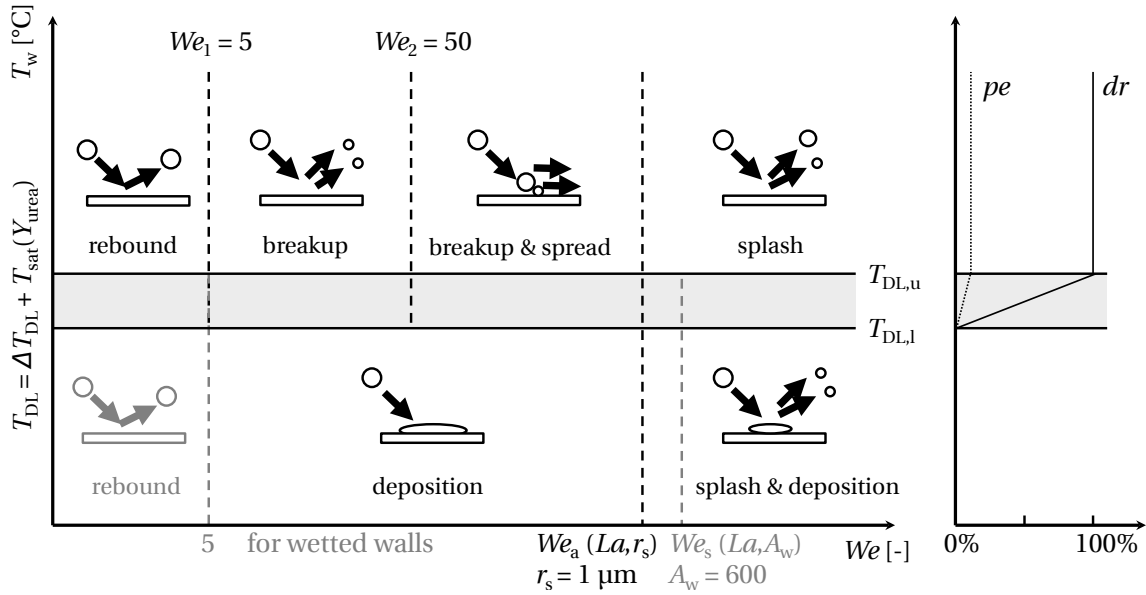


Figure 4.9: Multi-regime Bai Gosman droplet wall interaction model adapted to UWS (left-hand side) with corresponding deposition and partial evaporation ratios (right-hand side). Grey area marks transition regimes, axes not to scale.

events, n_{evap} , which were completely evaporated upon impact, versus the total amount of impingement events experiencing the Leidenfrost effect, n_{LF} , was denoted partial evaporation ratio pe :

$$pe = n_{evap} / n_{LF} \quad (4.6)$$

Bai and Gosman [99] used a set of dimensionless numbers in order to distinguish between droplet wall interaction regimes with different droplet impact energies, see Fig. 4.9. The droplet Weber and Laplace numbers were defined as

$$We_d = \frac{\rho_d d_d c_n^2}{\sigma_d} \quad (4.7)$$

$$La_d = \frac{\rho_d \sigma_d d_d}{\mu_d^2} \quad (4.8)$$

where ρ_d , d_d , c_n , σ_d and μ_d were the density, diameter, impact velocity component normal to the wall, surface tension and viscosity, respectively, of the droplet. The critical Weber numbers We_a and We_s , above which it was possible to observe splash effects on dry and wetted walls, respectively, were given as

$$We_a = A(r_s) La^{-0.18} \quad (4.9)$$

$$We_s = A_w La^{-0.18} \quad (4.10)$$

where $A(r_s)$ and A_w are empirical coefficients, the former depending on the surface roughness r_s [125].

Smith et al. [45] proposed an empirical calibration of the modified Bai Gosman model based on the original setup of Fischer [32]. The authors assumed pure wall wetting for UWS at temperatures below $T_{DL,l} = 271$ °C, by setting $\Delta T_{DL} = 207$ °C and $\Delta T_{trans} = 40$ °C, Fig. 4.10. This was adopted without further modification, as measurements confirmed that spray cooling immediately lowered the wall temperatures to purely wall-wetting regimes, even at exhaust temperatures up to 275 °C (data not shown, compare investigated operating points in Tab. 4.1). Furthermore, Smith et al. [45] achieved an

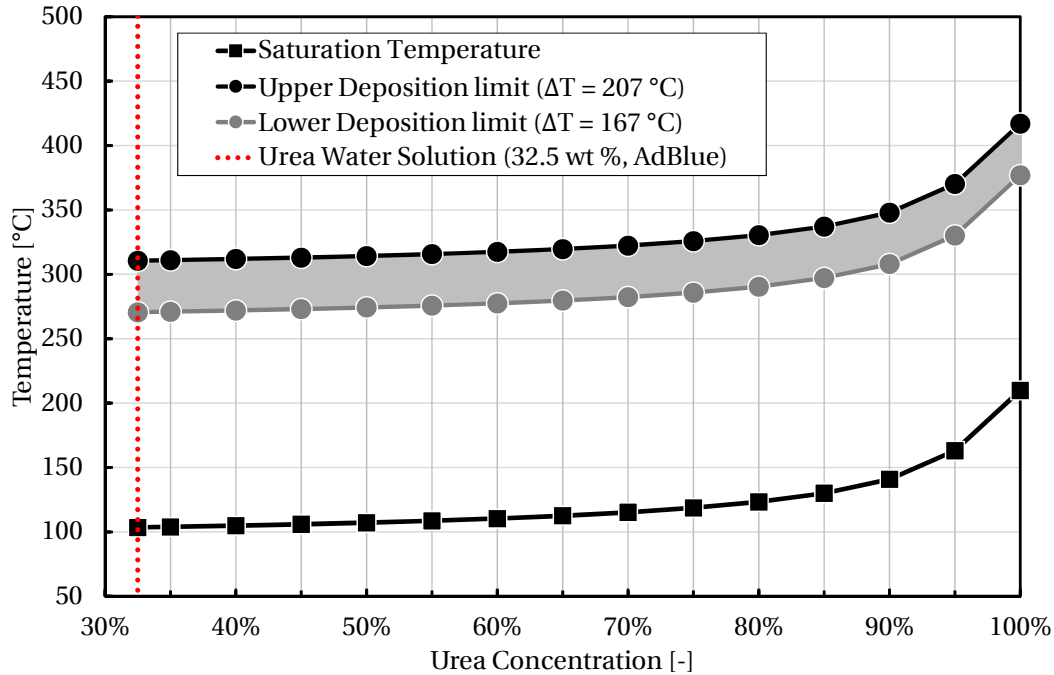


Figure 4.10: Saturation temperature and deposition limit temperatures as a function of the droplet urea concentration. Transition regime between wetting and non-wetting droplet wall interaction regimes marked in grey.

excellent representation of the secondary droplet spectrum by empirically calibrating A_w to 600. Following the suggestion of Fischer [32], $A(r_s)$ was held constant by setting r_s to $1 \mu\text{m}$. Equally, We_1 and We_2 were maintained at 5 and 50, respectively. A summary of the settings can be found in Tab. 4.7.

In the original implementation of the Bai Gosman impingement model, further regimes were distinguished using another threshold temperature, T_L , above the deposition limit [125]. In contrast to all regimes above T_L , the break-up and spread regime was implemented assuming increased heat transfer between droplets and wall due to boiling [125], see Fig. 4.9. Therefore, Fischer [32] regarded "the regimes between $T_{DL,u}$ and T_L [...]" as a better representation of the Leidenfrost phenomenon, than the mechanism implemented beyond T_L " (variable names adapted to match the nomenclature of the present work). Following the argumentation of Fischer [32], and in the absence of suitable calibration data, these regimes were deactivated by setting T_L to the high value of 1800 K.

Droplets entering the catalyst experience intensive interaction with the thin channel walls and hence evaporate quickly. This effect has to be considered in order to capture the formation of ammonia hot spots at the catalyst [45]. It was accounted for by slowing down the droplets after entering the catalyst and by selectively adapting the droplet breakup model in the porous medium to imitate rapid evaporation. Inside the catalyst the droplet velocity was calculated based on a slip relation between the catalyst flow \mathbf{u} and the droplet velocity \mathbf{u}_d , according to the relation $\mathbf{u}_d = \mathbf{u}(1 - S)$ [125]. With the slip factor set to a value close to unity, e.g. $S = 0.9999$, droplets were slowed down vigorously. Droplet breakup was based on the rate equation $dd_d/dt = -(d_d - d_s)/\tau$ where d_d denoted the instantaneous and d_s the stable droplet diameter [125]. Rapid droplet breakup was realised by setting d_s and the characteristic time scale τ to low values, i.e. $1 \mu\text{m}$ and 1ms , respectively. In accordance with the d^2 -law, the reduction of the initial droplet diameter led to a quadratic reduction of the evaporation timescales, see Fischer [32] or Musa et al. [142]. Eventually, droplets were depleted in the catalyst substrate within the single-digit ms range.

Table 4.7: Threshold calibration of the Bai Gosman impingement model adapted to UWS.

Threshold	Quantity	Value	Source	Comment
Surface roughness	r_s	1 μm	[32]	stainless steel
Splash boundary coefficient	A_w	600	[45]	wetted wall
Deposition limit offset temperature	ΔT_{DL}	207 $^{\circ}\text{C}$	[45]	
Leidenfrost transition temperature margin	ΔT_{trans}	40 $^{\circ}\text{C}$	[45]	
Partial evaporation ratio	pe	8 %	[45]	
Breakup boundary	We_1	5	[32]	
Breakup and spread boundary	We_2	50	[32]	

Wall Film Description

The propagation of the liquid film on the internal system walls was described using a two-dimensional finite volume approach [125]. In this Eulerian type framework, the wall film was assumed to be very thin and without impact on the boundary layer assumption. The fluid flow was considered laminar and incompressible, assuming a parabolic and piecewise linear velocity and temperature profile, respectively. Conservation equations for mass, momentum and energy were solved for each boundary cell containing liquid film. The model considered the impact of flow-induced shear forces, gravity, the momentum and enthalpy contribution of impinging droplets, the deceleration of films due to the influence of surface tension, and film stripping at sharp edges [32, 125]. In contrast to the droplet description, diffusion was considered in the description of convective transport within the wall film and in the evaporation model. Following the suggestion of Fischer [32], the binary diffusion coefficient was set to $D_1 = 1 \cdot 10^{-9} \text{ m}^2/\text{s}$ according to the findings of Constantino et al. [143]. All other temperature and concentration dependent liquid phase properties were assumed identical to those of UWS droplets, Tab. 4.6. Equally, Raoult's and Dalton's law were applied to determine the saturation temperature of the mixture and to distinguish between evaporation and boiling.

The effective heat flux into the film is significantly affected by the characteristics of heat transfer between solid walls and film, as well as the heat transport within the film. Below the boiling point and for low excess temperatures $\Delta T = T_w - T_{\text{sat}}$ heat transport is driven by natural convection [58, 144, 145]. Above, the formation of vapour bubbles enhances the heat transfer (nucleate boiling) up to the point where the heat flux becomes maximal (Nukiyama point/temperature), see Fig. 4.11. Beyond this point, heat transfer declines as the vapour bubbles begin to form an insulating vapour layer between solid wall and liquid film (transition boiling). Eventually, a heat flux minimum can be observed (Leidenfrost point/temperature) before the heat flux gradually begins to increase again due to thermal radiation (film boiling).

The temperature-dependency of the heat flux above the boiling point was captured with the Nukiyama pool boiling model [125]. The implementation allowed the specification of crucial parameters such as the maximum heat flux and the Leidenfrost temperature

$$T_{\text{LF}} = T_{\text{sat}} + \Delta T_{\text{LF}} \quad (4.11)$$

using a constant temperature offset ΔT_{LF} . It is worth noticing that the definition of the Leidenfrost point according to Eq. (4.11) was now consistent with that of the deposition limit, Eq. (4.5), i.e. a constant temperature offset was assumed between saturation and Leidenfrost temperature. The calibration was adopted from Fischer [32] without further modifications, see Tab. 4.8. In analogy to the formulation of the deposition limit, the model indirectly accounted for the dependency of the Leidenfrost effect on the actual urea concentration via the saturation temperature. In the absence of suitable measurement data, Fischer [32] calibrated the model using available data for pure water, in line with

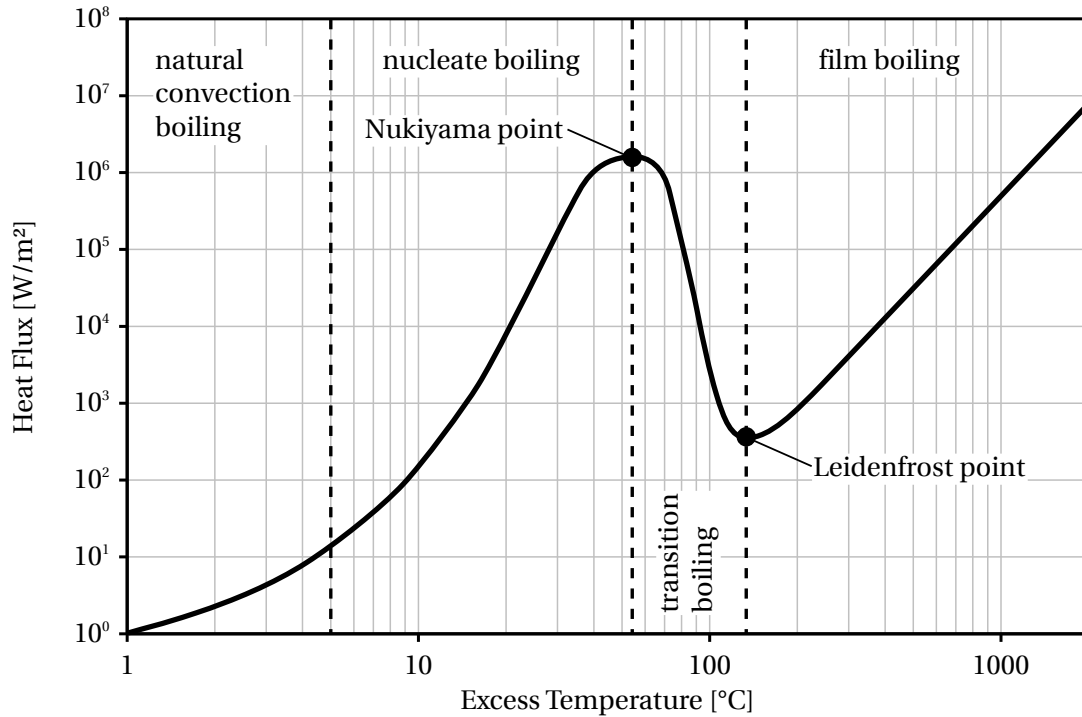


Figure 4.11: Schematic outline of the heat flux between solid walls and liquid film as a function of the excess temperature $\Delta T = T_w - T_{\text{sat}}$ for 32.5 wt % UWS (Nukiyama pool boiling model). Adapted from Talukdar [146] using approximate values for UWS from Fischer [32].

Table 4.8: Threshold calibration of the pool boiling model adapted to UWS.

Threshold	Quantity	Value	Source	Comment
Rohsenow exponent	n	2.07	[125, 147]	water on stainless steel
Rohsenow surface coefficient	c_{sf}	0.015	[125, 147]	water on stainless steel
Leidenfrost point temperature offset	ΔT_{LF}	110 °C	[125, 148]	water
Critical heat flux multiplier	c_{max}	0.015	[125, 148]	STAR-CD default
Critical heat flux range multiplier	c_s	1.2	[125, 148]	STAR-CD default
Leidenfrost heat flux multiplier	c_{min}	0.09	[125, 148]	STAR-CD default

the approach of Birkhold [101]. Fischer [32] verified the applicability of this approach based on the prediction of wall film pathways and wall cooling and found a good correlation.

4.2.4 Solid Walls

Heat transfer was modelled not only in the fluid but also in the solid phase in order to capture the thermal behaviour of the mixing elements and pipe walls (conjugate heat transfer [131]). Hence, heat conduction within the solid was considered along with thermal inertia as well as heat exchange with the exhaust and the surrounding atmosphere. This approach ensured the prediction of realistic temperature distributions and a correct thermal response to wall film evaporation. Free convection was assumed at the outer boundaries assuming an ambient temperature of 25 °C and a thermal resistance coefficient of 0.05 m²K/W.

Chapter 5

Mechanisms of Deposit Formation

5.1 Deposit Formation in a Series SCR System

Based on the literature study, deposit formation was expected to predominate at low temperatures. Hence, an operating point with low exhaust enthalpy and stoichiometric injection, OP 200/100/13, was chosen to gain a first insight into the temporal evolution of deposit formation in the underbody type SCR system. The visual interpretation of Fig. 5.1 revealed that deposits grew linearly with time and that the locations of the deposits remained identical in each experiment. Although the respective deposit nuclei were clearly visible after 15 min, a comparison against the deposits obtained after 120 min revealed that deposit accumulation was very slow. The deposit on the second blade from the right was missing after 30 min, see orange circle in Fig. 5.1(b), which was attributed to the fact that four separate experiments were conducted, each starting from a clean and deposit-free system. Minor variations of the experimental procedure may have affected the results. Moreover, it was unclear to what extent the process of deposit formation was affected during the short period between the suspension of injection and optical inspection, especially in the light of the low overall amount of deposits. These conclusions made clear that investigations on deposit growth needed to be conducted on a visually accessible geometry.

In order to identify major deposit locations and their temperature-dependency, the experiment duration was extended to 240 min and the exhaust temperature was gradually increased. The injection rate was raised to 35 mg/s as the amount of formed deposits was insignificant at OP 200/100/13 and overstoichiometric injection is a common practice during low-temperature operation in order to fill

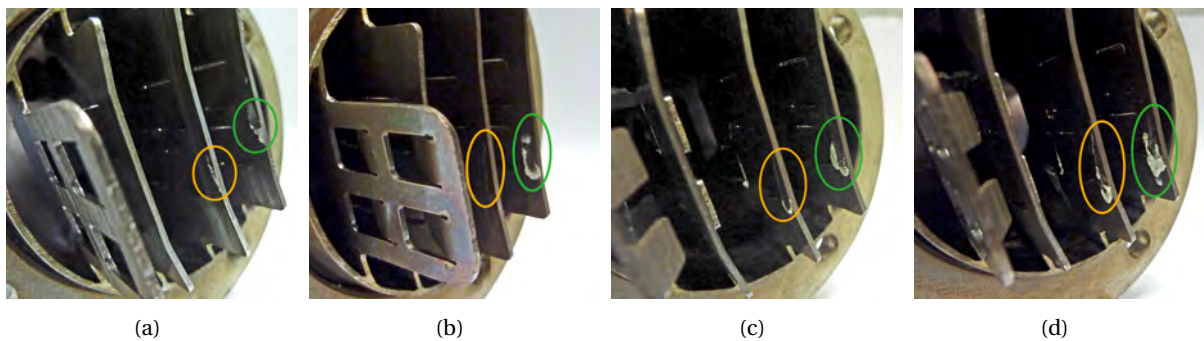


Figure 5.1: Deposit growth on the mixing element of the underbody type SCR system as a function of time at OP 200/100/13: 15 min (a), 30 min (b), 60 min (c), 120 min (d).

up the catalyst's NH_3 storage [149]. The analysis of the deposit yield¹ revealed that the amount of deposits dropped significantly with increasing exhaust temperature. While 14.5 % of the injected urea was converted into deposits at 200 °C, the deposit yield was reduced by approximately one order of magnitude at 240 °C, Tab. 5.1. The analysis showed that the amount of deposits adhering to the injector varied to a much lesser extent than the overall mass. In contrast to the higher-temperature OPs, a thin but closed deposition layer spread over the injector at OP 200/100/35 and substantially contributed to the increase of the deposit weight, Fig. 5.2 (first column). It is worthwhile mentioning that despite the deposits around the injector holes, no blockage was observed. The distinct temperature-dependency of the deposit weight was not reflected in the optical impression of the deposits on the mixing element, Fig. 5.2 (second and third column). Since the mixing element was the primary impingement target, it was also the key location for deposition. However, especially at low-temperature OPs, the exhaust enthalpy flux was not sufficient to guarantee complete preparation of the injected UWS. Excess UWS stripped from the mixer rear edges and effected secondary impingement as well as deposition on the downstream piping of the exhaust system. The latter accounted for a major fraction of the deposit weight at OP 200/100/35, Fig. 5.2 (fourth column). Only minor deposits were found on the catalyst inlet under all conditions (results not shown).

Table 5.1: Deposit mass and yield in the underbody type SCR system as a function of the exhaust temperature. Mixing section includes mixing element. Experiment duration 240 min.

Operating Point	Unit	OP 200/100/35	OP 220/100/35	OP 240/100/35
Injected urea mass	[g]	163.8	163.8	163.8
Deposit mass mixing section	[g]	23.79	7.21	2.41
Deposit mass injector	[g]	0.17	0.12	0.12
Deposit yield	[%]	14.5	4.4	1.5

The comparison between the deposits observed on the injector and the mixing element revealed further details on the particular mechanisms of deposit formation. Although the chemistry and physics of deposit formation apply regardless of the location, the preceding mechanisms of wall wetting are of entirely different nature. At the mixing element, droplet impingement was the primary cause as it led to liquid film generation, trickling and accumulation, as well as to droplet stripping. The present work focusses on these effects. At the injector, deposit formation was mainly triggered by injector leakage, i.e. liquid film release and droplet ejection after the completion of the actual injection event. However, a detailed description of these mechanisms goes beyond the scope of this work.

The experiments with the series exhaust system confirmed the fundamental temperature-dependency of deposit formation. It was interesting to notice that, despite the significant impact of temperature on the deposit yield, the location of the deposits was affected only to a minor extent. Initial deposit nuclei may form within less than 15 min after SOI. The investigations on the closed system provided only little detailed information about the mechanisms of deposit formation. However, the obtained data was suitable to verify the relevance of the mechanisms and to validate the predicted deposit formation risk, see Sections 5.2 and 6.3.

¹A definition of the deposit yield is given in Section 2.1, Eq. 2.1.

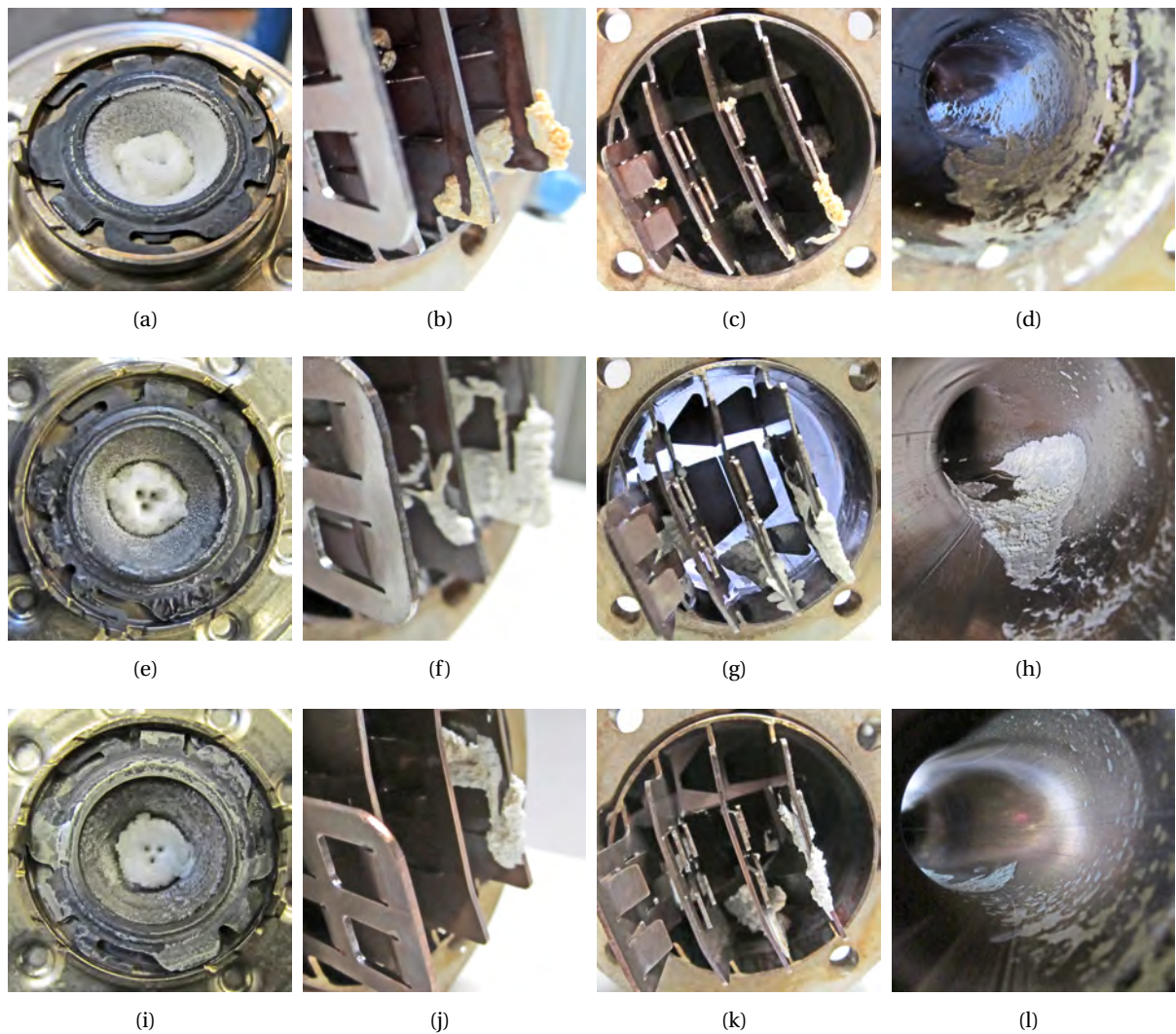


Figure 5.2: Deposit formation in the underbody type SCR system as a function of the operating conditions: OP 200/100/35 (first row), OP 220/100/35 (second row) and OP 240/100/35 (third row). Locations: injector (first column), mixing element (second and third column) and mixing section (fourth column). Experiment duration 240 min.

5.2 Deposit Formation on Mixer Blades

In order to gain a deeper understanding of the mechanisms involved in the formation of deposits, the areas of interest were made optically accessible. An optical volume was equipped with a surrogate mixing element, which imitated the geometric features of the mixer used in the underbody type SCR system. In this section, common wall film transport phenomena are discussed along with typical deposition areas. Experimental results obtained using the optical volume are compared with results from the series exhaust system in order to verify their representativity. Eventually, the mechanisms which promote or impede deposit formation are identified.

5.2.1 Wall Film Transport and Deposition

Wall film formation and transport was recorded on a mixing element plate exposed to two injector beams. A steady state had been attained for each operating point considering wall temperature, UWS evaporation, liquid film spreading and transport. The size of the wetted areas increased with the injection rate and decreased for rising temperatures, Fig. 5.3. For an exhaust temperature of 200 °C, complete wall film evaporation was unachievable even for lowest injection rates, such as 3.3 mg/s. A noticeable area remained permanently wetted and wall film was periodically transported off the impingement zone. In contrast, at 270 °C the preparation of UWS was practically residue-free for injection rates as high as 6.5 mg/s. Although in this case, too, a small area remained permanently wetted, the entire rest of the injected liquid was evaporated. It was striking that, despite being permanently wetted, impingement areas were not subject to deposit formation in any of the cases.

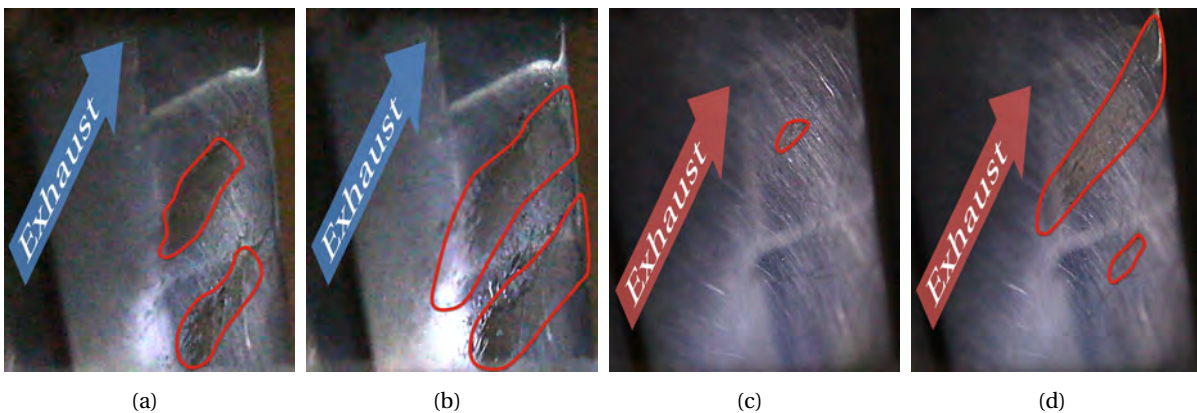


Figure 5.3: Wall wetting in primary impingement areas as a function of the injection rate: OP 200/100/3.3 (a), OP 200/100/6.5 (b), OP 270/100/6.5 (c), OP 270/100/10 (d). Permanently wetted areas marked in red, arrows indicate direction of the exhaust flow. Images show end of the corresponding injection cycles, a steady state has been attained.

Excess wall film trickles off the primary impingement areas due to the momentum introduced via the impinging droplets, the shear stresses induced by the flow field, and gravity. Wall film frequently accumulates at blade edges, Fig. 5.4(a), and is pushed over the edge. Due to adhesion forces, the film typically remains attached to the blade and flips around the edge onto the reverse side of the blade, Fig. 5.4(b). The figures demonstrate typical distribution mechanisms. However, depending on the balance between the local forces, wall film may not only flip from the upper onto the lower part of an edge but also vice versa, i.e. against gravity. In particular at blade edges, the supply with fresh UWS displaces the present film and is able to push it even in the upstream direction, Figs. 5.4(b) and 5.4(c). If wall film accumulates to a certain point, gravitational and shear forces cannot be compensated

by adhesion anymore. As a consequence, droplets strip off edges and impinge on subjacent blades, Fig. 5.4(c), or the downstream piping. At blade joints wall film is distributed onto all adjacent blade faces, Fig. 5.4(d). The experiments show that the direction of wall film propagation is determined by the local balance between momentum, shear stresses, gravity and adhesion. Wall film is extensively distributed on the mixing element, if it does not decompose rapidly after impingement.

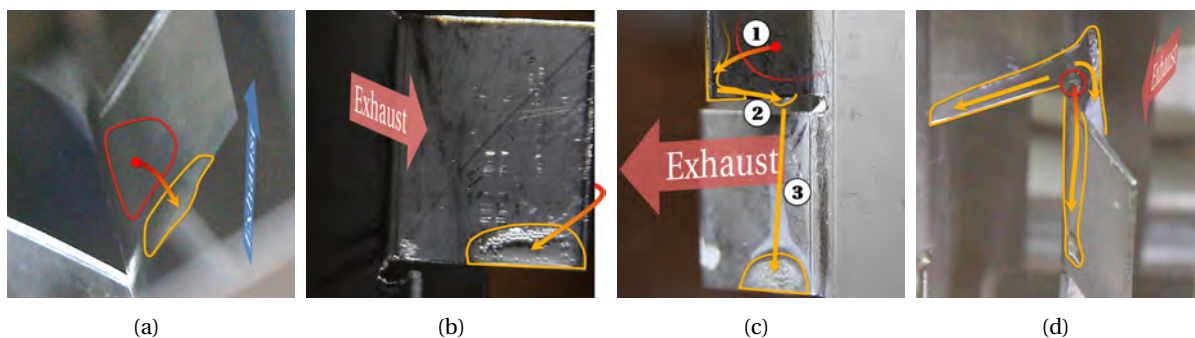


Figure 5.4: Wall film pathways and accumulation at edge exposed to direct incident flow (a), droplet flipping around edges and accumulation on reverse blade side (b), droplet stripping from edges and accumulation on subjacent blade (c), wall film distribution at blade joint (d). Primary impingement areas marked in red, areas with wall film accumulation marked in yellow. Broad blue and red arrows indicate direction of the exhaust flow.

Persisting liquid film was eventually converted into solid deposits. A systematic parameter study was conducted to investigate deposition locations as a function of exhaust temperature, mass flow, and injection rate. A number of representative scenarios have been compiled in Fig. 5.5. The extent of deposit formation ranged from tiny deposits in close proximity to the impingement areas, Fig. 5.5(e), to noticeable deposits at the lower rear blade edge, Fig. 5.5(g). A further increase of the injection rate led to significant liquid accumulation and continuous droplet stripping, Fig. 5.5(d). As the film at the lower blade edge oscillated vigorously, wall film occasionally splashed onto adjacent areas outside of the main wall film pathways and immediately solidified. The fact that deposits of similar size and location were found at different operating conditions indicates that the deposition location is essentially determined by the balance between exhaust enthalpy flux and UWS injection rate. An increase of the exhaust temperature and/or mass flow shifted the deposit location upstream, whereas raising the injection rate shifted the location downstream. The results prove that fluid film pathways do not depend on the operating conditions. This is plausible as the general structure of the flow field is not modified by the operating conditions, except for the velocity magnitude which scales with the mass flow rate and temperature [32]. Hence, shear stress, being a major driving force for wall film transport, will also mainly vary in magnitude but not in direction. Liquid film continuously evaporates as it trickles off the primary impingement areas and is heated up. Hence, the film thickness decreases and adhesion forces gain in importance, compared to shear stresses and gravitation. Eventually, the film is thinned and slowed down to the point where secondary reaction products are not carried away by the film anymore, but adhere at the system wall. Ultimately, deposit formation has to be expected as soon as the exhaust enthalpy flux is not sufficient to decompose the injected UWS immediately. While deposits will form alongside the fluid film pathways, their exact location is determined by the balance between exhaust enthalpy flux and injection rate. Droplet stripping or liquid film splashing do not impede deposit formation but shift it to a downstream location or an adjacent blade area.

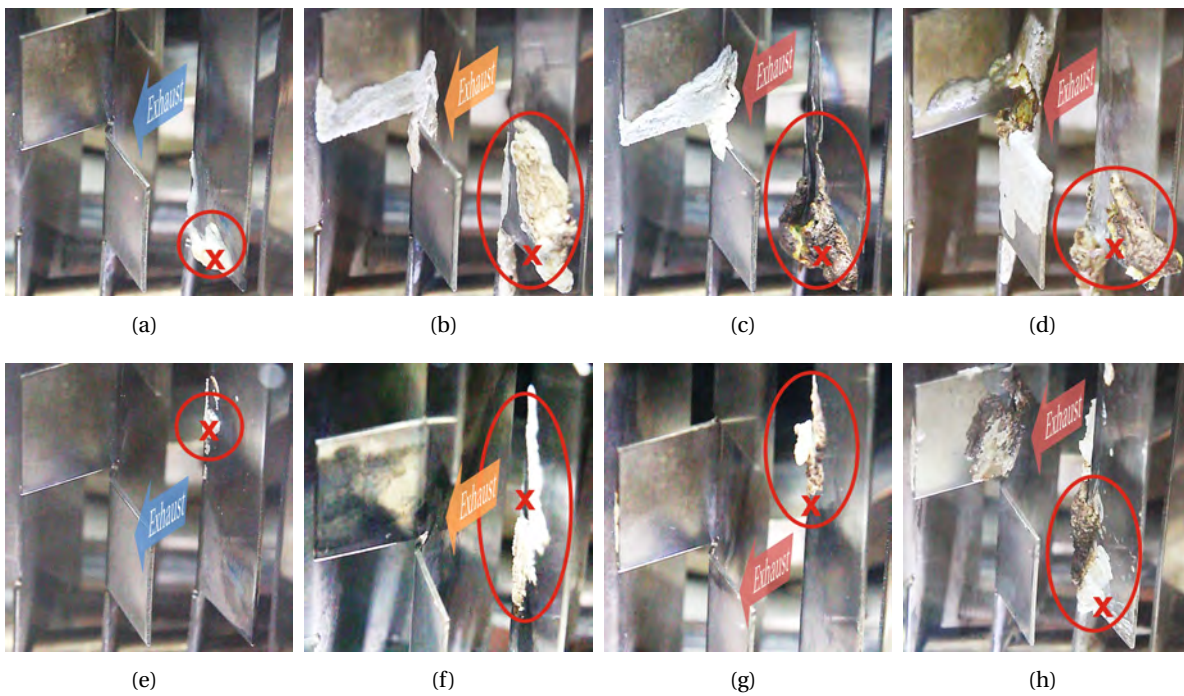


Figure 5.5: Locations of deposit formation as a function of temperature and injection rate after 60 min of dosing: OP 200/100/3.3 (a), OP 235/100/13 (b), OP 270/100/25 (c), OP 270/100/35 (d), OP 200/200/3.3 (e), OP 235/200/13 (f), OP 270/200/25 (g), OP 270/200/35 (h). Red circles mark deposit locations, red crosses indicate thermocouple locations. Thermocouples installed on reverse blade side. Broad blue, orange and red arrows indicate direction of the exhaust flow.

The question arose whether the phenomena observed in the optical volume were representative for series SCR systems. To answer this question, typical deposition scenarios from the respective experiments were compared, Fig. 5.6. The excellent correlation shows that the optical box represented these phenomena in a realistic way. The comparison confirms that liquid film accumulation and deposition frequently occur at geometric features, such as blade edges, gaps, and holes, but are not bound to them. All areas exposed to wall wetting have to be considered as potential deposit locations, regardless of whether these faces are exposed to intense shear flow, or lie within a wake region. Holes, gaps, and blade edges do not immediately trigger deposit formation. However, as the film is distributed onto a broader area at such geometric irregularities, they promote further thinning and, eventually, deposition of the UWS film in the form of solid deposits.

The obtained results shed some light on the mechanisms of wall film transport and deposition. However, they also showed that conclusions about the risk of deposit formation in a specific area could not be drawn solely based on the location and the local flow field. Further investigations were necessary to identify the mechanisms which promote or prevent deposit formation, and to quantify the boundaries of deposit formation.

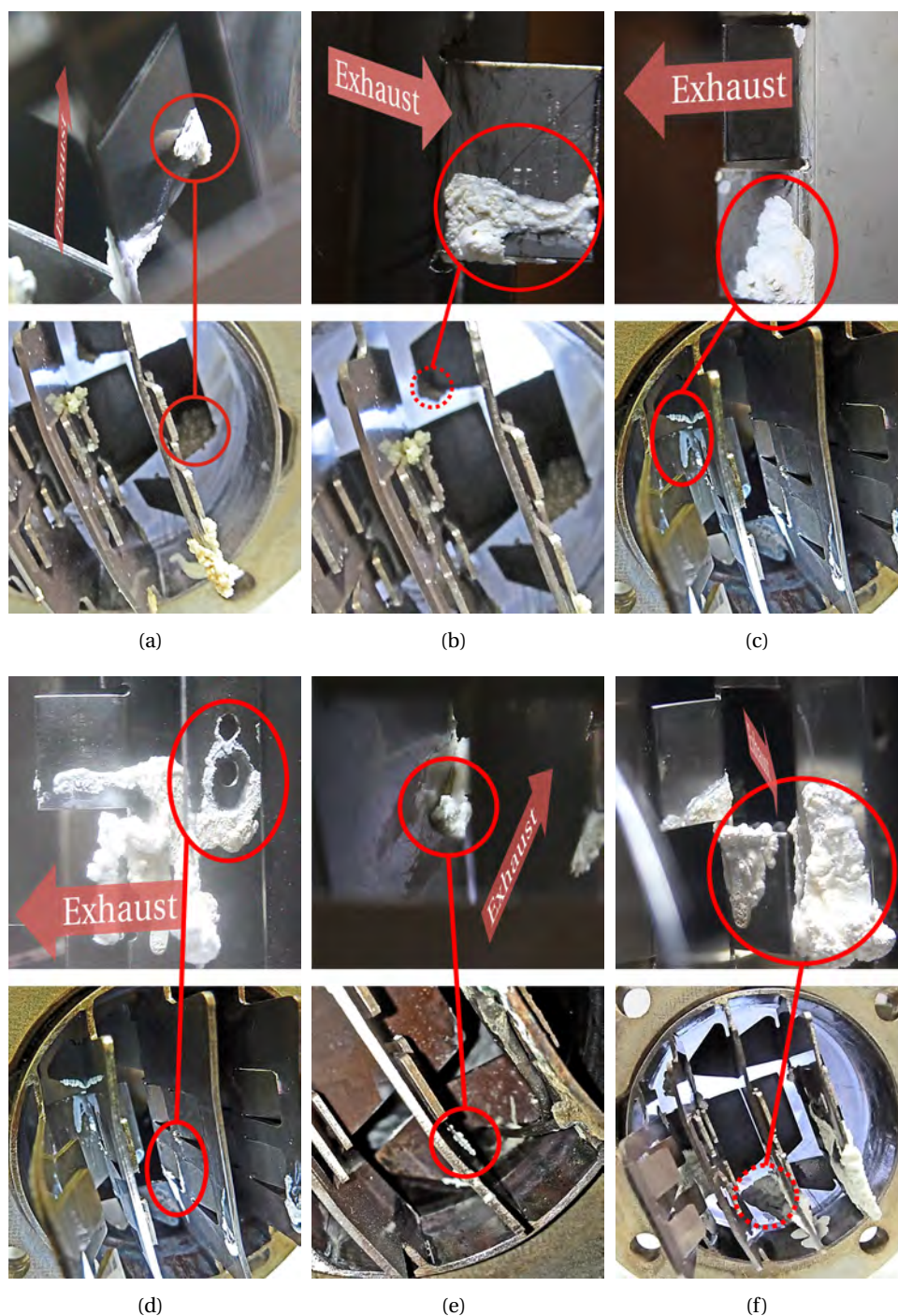


Figure 5.6: Common deposit formation scenarios at blade edges: Frontal blade side (a, incident flow), reverse blade side (b, wake region), stripping from edge onto subjacent blades (c, wake region). Common deposit formation scenarios at blade faces: wall film trickling through holes and gaps in plain surfaces (d, shear flow), plain surface (e, shear flow), rear blade side (f, wake region). Upper images: experiments in optically accessible box. Lower images: corresponding deposit formation mechanism in underbody type SCR system. Dashed lines indicate deposit formation on rear side of the tagged blade. Broad red arrows indicate direction of the exhaust flow.

5.2.2 Deposit Growth and Prevention

Typical sequences of deposit growth are depicted in Figs. 5.7(a) and 5.7(b). Once liquid film has solidified locally it can act as a nucleus for further deposit accumulation. UWS which reached the existing deposit solidified at its upstream border (*damming growth*). However, some deposits also grew at peripheral borders (*peripheral growth*), despite the fact that they were not wetted from outside at the corresponding edge. These cases show that UWS is transported through the capillary structure of the deposits, i.e. through small canals and fissures. This can be regarded as a separate growth mechanism and is responsible for the formation of deposits in the underbody type exhaust system, which were not plausibly explicable on the basis of liquid film pathways, see Figs. 5.7(c) and 5.7(d). The experiments reveal that deposits can grow in virtually any direction and reach locations which are not covered by regular fluid film pathways.

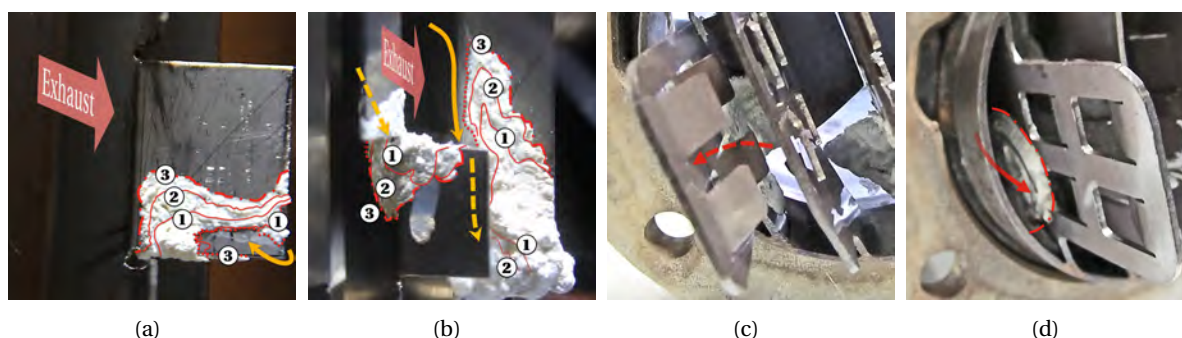


Figure 5.7: Common mechanisms of deposit growth as a function of time: OP 270/100/13 after 30 min (a, (1) 10 min, (2) 20 min, (3) 30 min), OP 270/100/25 after 60 min (b, (1) 20 min, (2) 40 min, (3) 60 min). Deposit growth on the mixing element of the underbody type SCR system at OP 220/100/35 after 240 min: frontal view (c, deposit formation at the rear blade) and left-hand side view (d, deposit formation resulting from wall film flipping onto the reverse blade side and subsequent peripheral deposit growth in the upstream direction). Yellow arrows indicate liquid film trickling pathways (dashed if hidden by blades), red arrows indicate direction of deposit growth (dashed if hidden by blades). Dotted red lines: damming growth, dotdashed red lines: peripheral growth. Broad red arrows indicate direction of the exhaust flow.

The consecutive steps of deposit formation are initial wall wetting, liquid film accumulation, deposit nucleus formation and deposit accumulation, Fig. 5.8. The study of the impingement zones over a period of 60 min revealed that, despite permanent wetting, deposit nuclei do not form within these areas. Impinging droplets cause a continuous dilution with fresh UWS, and present film was continuously transported off these areas. On a physical basis, this can be related to strong and continuous motion and mixing of the film, i.e. intense liquid film dynamics. The superposition of periodic supply and continuous removal of UWS manifests in a strong fluctuation of the local wall film thickness. Due to the continuous wall film trickling, secondary reaction products (i.e. potential deposits) are continuously removed from the impingement areas. Moreover, the average local urea concentration is lower, which effectively also inhibits undesired reactions. It is probable that wall film in the direct vicinity of primary impingement areas exhibits similar properties. Concludingly, the formation of deposit nuclei is effectively prevented in areas with intense liquid film dynamics. However, if the film trickles off these areas and thins down through continuous evaporation, the dynamics can be reduced down to a point where deposits readily form.

The visual analysis of particularly thick wall films revealed that they trickle with higher velocities than thin films, as gravitational and shear forces gain in significance over adhesion forces. Besides, the

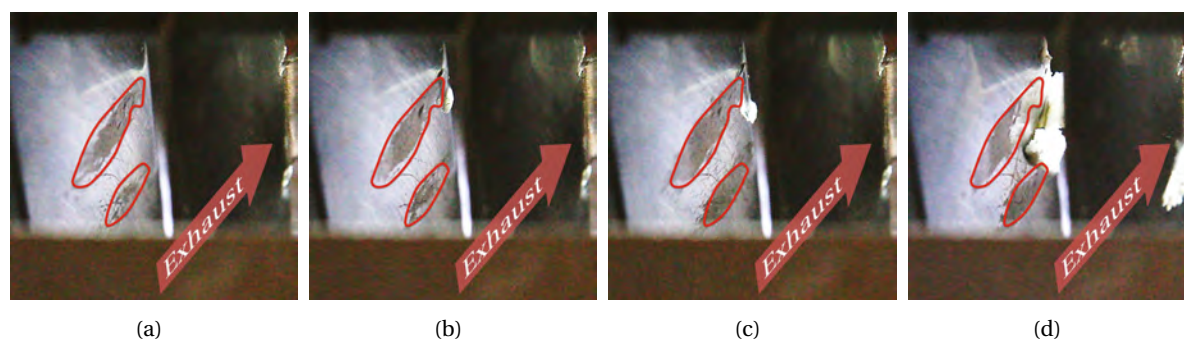


Figure 5.8: Consecutive steps of deposit formation on a plain mixer surface: initial wall wetting (a, 30 s after SOI), liquid film accumulation (b, 90 s after SOI), deposit nucleus formation (c, 130 s after SOI), and deposit accumulation (d, 60 min after SOI). Primary impingement areas marked in red. Broad red arrows indicate direction of the exhaust flow.

heat input into the film and the evaporation rates are reduced, due to the smaller surface to volume ratios. Ultimately, solidification of the film is suspended and potentially formed secondary reaction products are continuously washed away. As thick films transport large amounts of UWS, they cause massive liquid phase accumulation at the lower/rear blade edges, Fig. 5.9. In further consequence, this behaviour leads to very thick films and to continuous droplet stripping. In areas with intense accumulation, present liquid film is continuously diluted with fresh UWS and removed through droplet stripping. Such film is permanently put into motion and mixed, which impedes deposition locally. Potentially formed secondary reaction products are continuously removed and deposition can effectively be prevented over long periods (> 60 min).

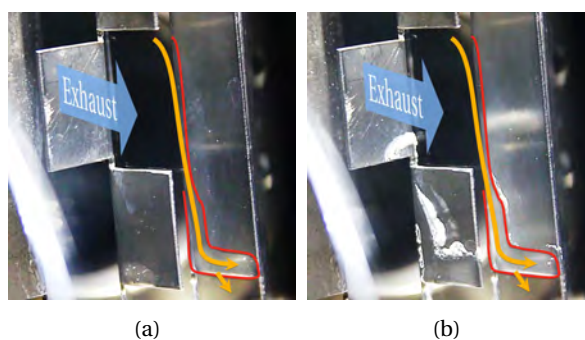


Figure 5.9: Prevention of deposit formation by intensive liquid film trickling and accumulation: 1 min after SOI (a), 60 min after SOI (b). OP 200/100/13. Red lines indicate wall film boundaries, yellow arrows indicate liquid film trickling pathways and stripping from edge. Broad blue arrows indicate direction of the exhaust flow.

All previous investigations showed that rear blade edges are of key importance during the formation of deposits. In order to evaluate whether the shape of the blade edges had any influence on the deposit formation risk, single blades of mixer 2 of the close-coupled type SCR system were whetted to yield sharp edges, Fig. 5.10(a). Experiments with and without sharpened rear blade edges revealed that the shape of the edges had practically no impact, neither on the extent nor on the location of deposit formation on the mixing element, compare Figs. 5.10(b) and 5.10(c).

The experiments presented in this section illustrate that intense liquid film dynamics are the root cause for these major mechanisms preventing deposit formation. In primary impingement areas and their vicinity, this becomes visible in the continuous fluctuation of the local wall film thickness. In

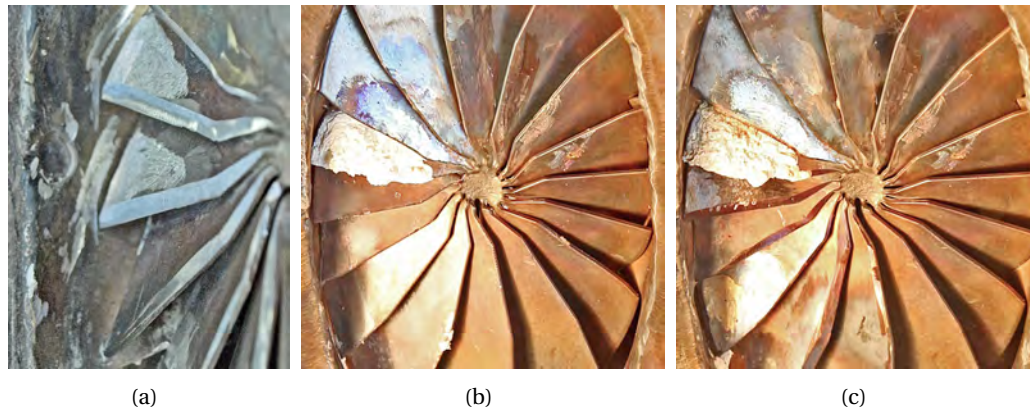


Figure 5.10: Sharpening of single rear blade edges exposed to deposit formation (a). Deposit formation on the rear blade edges with (b) and without (c) sharpening. Test case: mixer 2 in combination with the 6-hole injector. OP 275/170/45, experiment duration 90 min.

case of thick films and in wall film accumulation areas, the effect becomes obvious through high trickling velocities and high film thicknesses in combination with stripping from edge, respectively. In order to exploit this knowledge for the assessment of the deposit formation risk, it is necessary to determine critical thresholds for each mechanism. As measuring such thresholds is very difficult, a set of criteria will be formulated for each mechanism and the corresponding thresholds will be empirically determined in the modelling section, see chapter 6.

5.3 Deposit Formation Boundaries and Conditions

In order to quantify both the boundaries and the conditions of deposit formation in SCR systems, the process was studied on the surrogate mixing element over a wide range of operating conditions. In this section, the deposition limit, deposit solidification temperatures and times, as well as deposit accumulation are assessed. Moreover, it provides information about critical injection rates, and helps to understand how the described impact factors contribute to the severity of individual deposits.

5.3.1 Deposition Limit

A parameter study was conducted to determine the deposition limit as a function of the operating conditions. Fig. 5.11 depicts the dependency of the temperature drop, ΔT_m on the steady state temperature of the impingement area at EOI, $T_{m,EOI}$, for different exhaust mass flows and UWS injection rates. Approximate boundaries were added based on the visual analysis of the wall wetting regimes. However, they shall not be interpreted as sharp thresholds, as the regimes blended into each other. The shape of the curves, i.e. the increase of the cooling performance with decreasing temperatures, reflects the changes of the underlying heat transfer mechanisms from film boiling via transition boiling to nucleate and natural convection boiling. The graphs reveal that the cooling performance rises with increasing injection rates (injection pulse lengths) and decreasing exhaust mass flows (enthalpy fluxes). The deposition limit marks the boundary between occasional wall wetting (Leidenfrost transition) and a stable Leidenfrost effect. The latter can be regarded as another mechanism preventing deposit formation, as it impedes wall wetting permanently.

At high enthalpy fluxes in combination with low injection rates (200 kg/h, 13 mg/s), wall wetting was omitted down to temperatures of approx. 264 °C. In contrast, at low enthalpy fluxes in combination

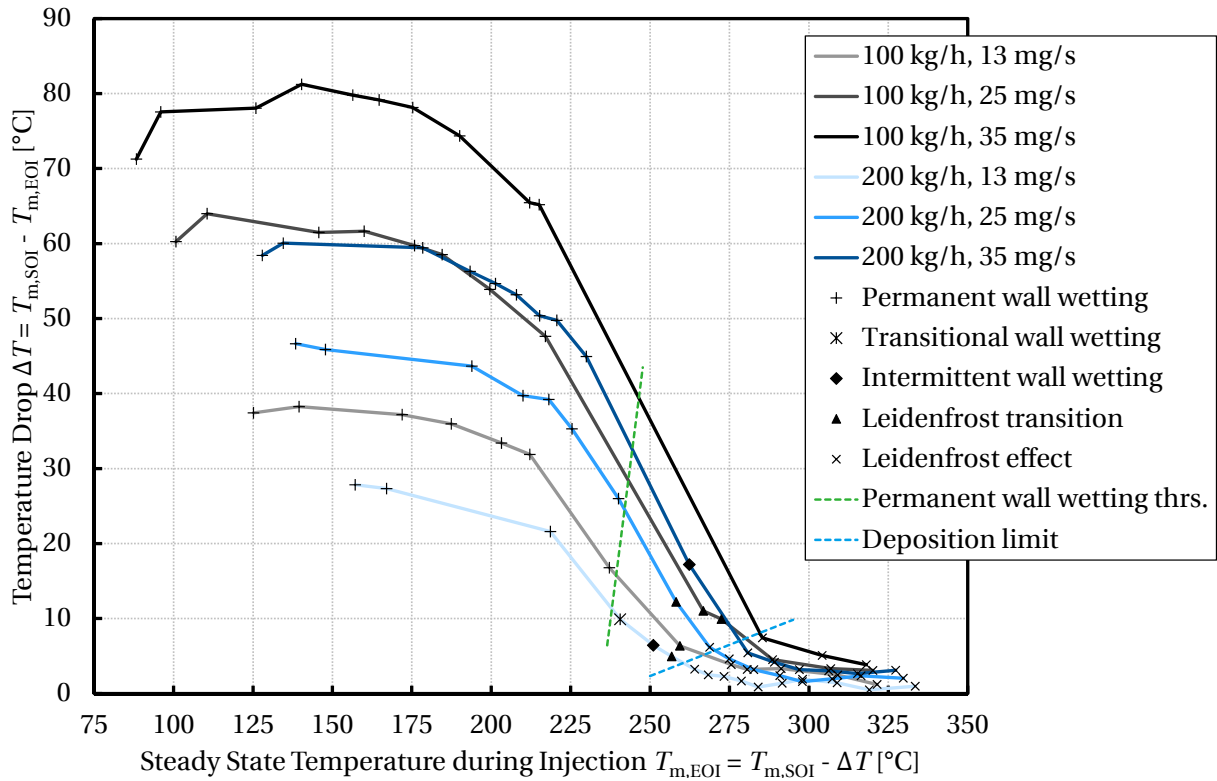


Figure 5.11: Evolution of solid cooling ΔT as a function of the steady-state temperature of the mixing element prior to end of injection $T_{m,EOI}$, for different exhaust mass flow and injection rates. Approximate boundaries (thresholds) have been added to facilitate the differentiation of the wall wetting regimes.

with high injection rates (100 kg/h, 35 mg/s) temperatures above 285 °C were necessary to prevent wall wetting. The results demonstrate that an increase of the injection rate shifts the deposition limit towards higher temperatures. However, they also show that this effect can be compensated by raising the exhaust enthalpy flux. From a general perspective, the deposition limit is determined by the balance between the exhaust enthalpy flux and the specific impingement mass flow rate, Eq. 2.2. Depending on the operating conditions, the deposition limit on a typical mixing element may lie in the range between approx. 250 °C and 300 °C. Obviously, the complexity of droplet wall interaction renders a universal specification of the deposition limit cumbersome.

Permanent wall wetting was observed below approx. 230 °C. The lower the temperature, the more undecomposed film was available for deposition. In the temperature window between the permanent wall wetting threshold and the deposition limit, the walls were periodically wetted, but the film always evaporated completely prior to the next injection event. The results clearly point to the fact that the permanent wall wetting threshold is, in fact, the more relevant boundary. If it is not transcended, deposit formation is prevented due to the absence of a persisting wall film. Ultimately, whether or not a wall film is completely evaporated is essentially determined by the local balance between the film mass and the (temperature and concentration-dependent) heat input into the film.

5.3.2 Solidification Conditions

The systematic parameter study presented in Section 5.2.1 revealed that the deposit location alongside a wall film pathway was essentially determined by the balance between exhaust enthalpy flux and

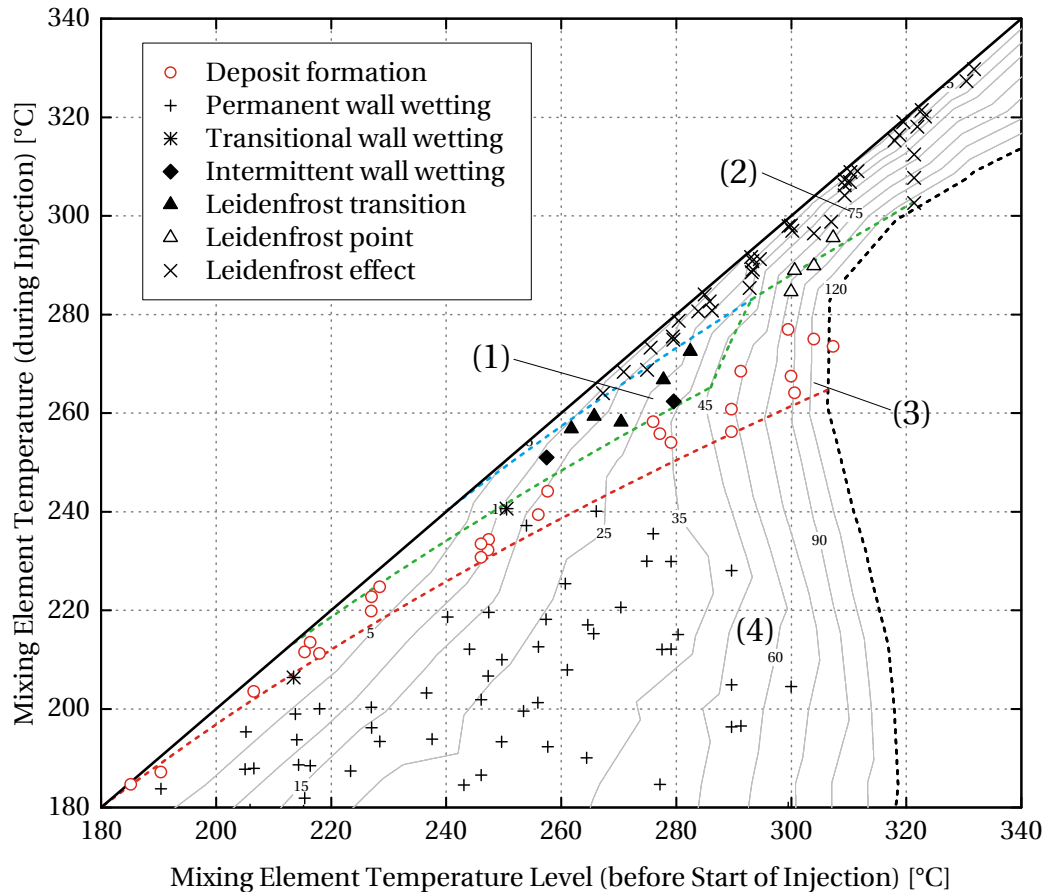


Figure 5.12: Wall wetting and deposit formation on the mixing element as a function of the temperature: intermittent and transitory wall wetting regimes (1), Leidenfrost effect (2), deposit formation (3), and permanent wall wetting (4). Approximate regime boundaries marked by dashed lines: minimum solidification temperature (red), permanent wall wetting threshold (green), and deposition limit (blue). Injection rates shown as contour lines.

injection rate. In order to shed further light on the boundary conditions of deposit formation, the solidification temperatures T_s were evaluated for all experiments conducted during the study, Fig. 5.12. In all cases, the impingement areas exhibited permanent wall wetting. The respective temperatures were added to the chart. Furthermore, it was complemented with the data obtained during the investigation of the deposition limit. All measurements were marked according to the observed wall wetting regime. The abscissa of Fig. 5.12 shows the temperature level of the mixing element before SOI $T_{m,SOI}$. The ordinate indicates the respective steady-state temperatures, which appeared during the observed phenomena. For low exhaust enthalpy fluxes, the minimum temperature was limited by the droplet temperature upon injection, ranging from 50 °C to 80 °C (data not shown). For high exhaust enthalpy fluxes, it was determined by the onset of the Leidenfrost effect at the maximum injection rate, 120 mg/s.

The data reveals that for temperatures below $T_{m,SOI} \approx 215$ °C, complete decomposition was not possible (intersection of the green and solid black line). The injected UWS was converted either into a deposit or retained its fluid state. With respect to typical dosing strategies, this range of operating conditions cannot be avoided. Deposits exhibited a rather moist consistency up to approx. 210 °C and could be washed away easily, if the injection rate was increased. Above 215 °C, complete UWS decomposition was possible (green line), if a critical injection rate was not exceeded. Up to $T_{m,SOI} \leq 290$ °C, it was characterised by the regime transition between intermittent and permanent wall wetting. Above

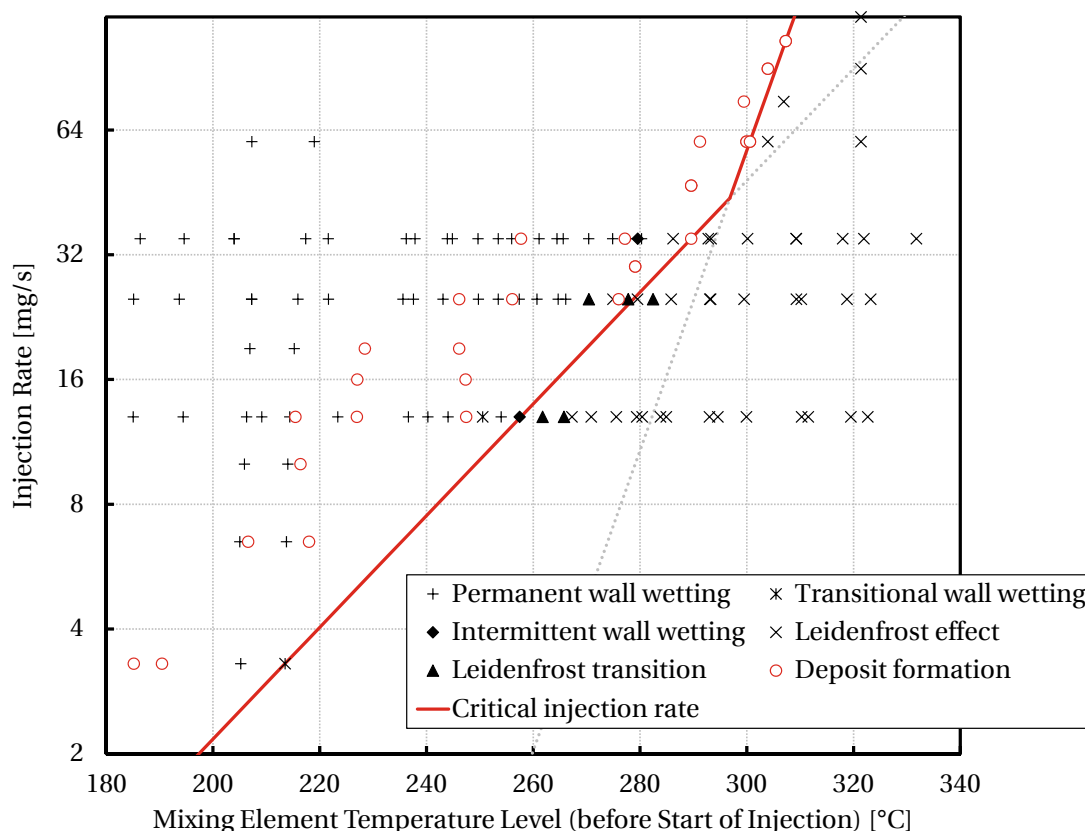


Figure 5.13: Critical injection rate for the onset of permanent wall wetting and deposit formation on the mixing element, as a function of the mixing element temperature level.

300 °C, intermittent wall wetting could not be observed anymore. If the impingement area was cooled beyond the Leidenfrost point, the walls were permanently wetted and deposits were formed. The critical injection rate increased exponentially, Fig. 5.13 (note the logarithmic scale of the ordinate). The transition between the characteristic behaviour became apparent in the change of the growth rates around 295 °C. In the experiments, excess wall film trickled off the impingement areas, thinned down and heated up. Alongside the fluid film pathways, the liquid film dynamics continuously reduced to an extent which allowed solidification. The eventual solidification temperature rose with increasing mixing element temperature level and laid within a narrow temperature band.

On a physical basis, the observed behaviour can be explained using the Nukiyama pool boiling curve. If the temperature of the impingement area drops beneath the Leidenfrost point, the heat flux increases sharply and the wall is wetted. Depending on the local balance between film mass and heat input into the film, the temperature may recover sufficiently prior to the next injection and evaporate the film completely. Intermittent wall wetting can be observed if this balance can be maintained. If the heat input is insufficient, the temperature of the impingement area further drops and the walls are permanently wetted. While Fig. 5.13 proves that an increase of the injection rate may be compensated by raising the temperature, the data in Fig. 5.12 demonstrates the limits of this measure. The heat consumption of the evaporating film increases with the injection rate. While evaporative cooling of the solid walls is very efficient, the temperature recovery of the impingement areas will at some point be limited by the maximum heat input of the exhaust gas. This may be seen as an explanation why a stable transitory behaviour between pure Leidenfrost effect and permanent wall wetting was only observed up to just above $T_{m,SOI} = 280$ °C. Above 300 °C, permanent wall wetting and subsequent deposit formation was triggered as soon as the temperature fell below the Leidenfrost point. This

behaviour also became visible in the rate change of the critical injection rate characteristic around $T_{m,SOI} = 295\text{ }^{\circ}\text{C}$.

Obviously, the validity of the specified critical injection rate is limited to the investigated system and operating conditions. Considering the multitude of impact factors, a generalisation to arbitrary systems and conditions is hardly possible. Even within one system, the onset of permanent wall wetting depends on the local balance between the specific impingement mass flow rate and the heat input. While the former depends on the injection strategy, spray targeting, and characteristics, the latter is determined by the effective heat fluxes between exhaust gas, film and solid. For instance, an extension of the impingement area A_{imp} would reduce the specific impingement mass flow rate $\dot{m}_{imp,s}$ and, thus, raise the critical injection rate by promoting wall film evaporation. This would be equivalent to shifting the contours of constant injection rate in Fig. 5.12 towards lower mixing element temperature levels $T_{m,SOI}$. As a consequence, system operation with two different injectors may yield an entirely different deposit formation risk, even if the exhaust temperature, mass flow, and the injection rates are maintained constant.

The analysis of the experimental data made clear that it is neither reasonable nor possible to specify a universal permanent wall wetting threshold. The determination of a system-specific critical injection rate is bound to a modelling approach capturing all involved physical effects, ranging from an accurate representation of the spray characteristics, targeting, and droplet wall interaction, to the correct prediction of liquid film dynamics and the effective heat fluxes between exhaust gas, fluid film and solid material. Besides, the sole prognosis of whether or not an excess wall film will be formed, is not sufficient to determine whether or not the resulting deposit will pose a risk to reliable system operation. Therefore, the solidification timescale, deposit accumulation and the content of the deposit were included into the analysis to determine the actual deposit severity, see Sections 5.3.3-5.4.2.

5.3.3 Solidification Timescales

Depending on the operating conditions, the time between SOI and the formation of a deposit nucleus varied significantly. Below $T_{m,SOI} = 200\text{ }^{\circ}\text{C}$, the solidification timescales t_s noticeably exceeded values of 600 s. Above $300\text{ }^{\circ}\text{C}$, conversion into solid deposits occurred in less than 160 s, Fig. 5.14. In the intermediate temperature range $200\text{...}300\text{ }^{\circ}\text{C}$, the UWS solidification timescales did not depend on the mixing element temperature level. The comparison of operating points with identical mixing element temperature level yielded that the solidification timescales were lower for lower injection rates as well as for higher exhaust mass flows, see Fig. 5.14 for $T_{m,SOI} = \text{const}$. This trend was inverted, however, if the amount of excess wall film was very small, e.g. around $T_{m,SOI} = 280\text{ }^{\circ}\text{C}$. In such cases, it was possible that the respective solidification timescales increased by a factor of up to 2...3, even compared to operating points with similar mixing element and deposition temperatures. This behaviour was also equivalent to very slow deposit accumulation. The minimum observed timescale was $t_s = 45\text{ s}$, typical values ranged between 60 s and 240 s. In case of strong UWS accumulation at rear blade edges, the liquid phase was put into vigorous motion. As a consequence, UWS continuously splashed onto hot and dry, adjacent blade face areas and solidified immediately. This can be seen as supporting evidence that droplets stripping from edges also do not hinder deposit formation but shift the problem towards the downstream piping. The experimental results demonstrate that even critical operating conditions do not immediately trigger deposit formation at low temperatures. At high temperatures, however, the temporal delay between start of injection and UWS solidification is short.

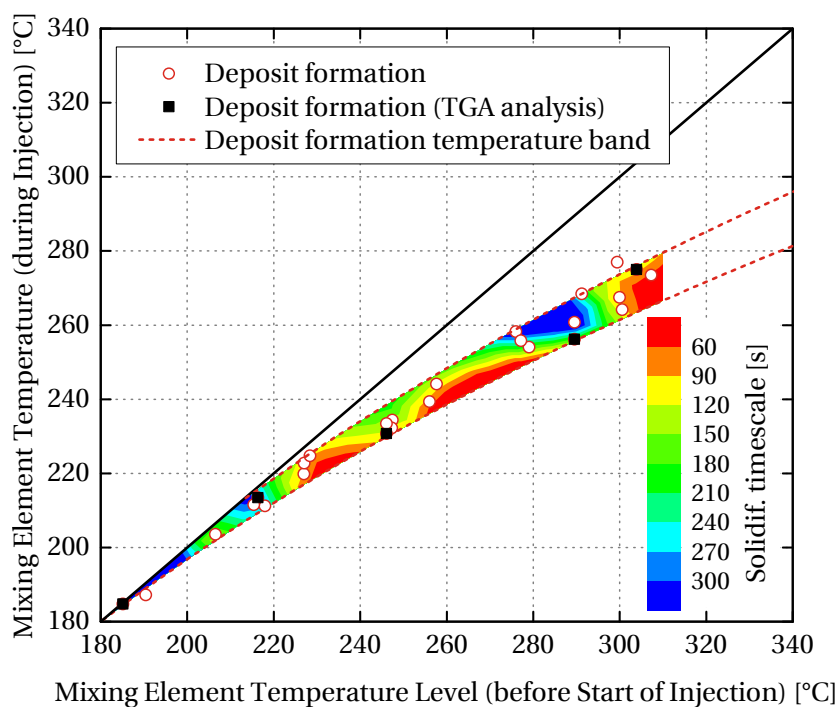


Figure 5.14: UWS solidification timescales as a function of the mixing element temperature level. Deposit formation temperature band adopted from Fig. 5.12.

5.3.4 Deposit Accumulation

Deposit accumulation was assessed optically by comparing to a reference. The individual deposits were classified based on a scale with six levels. At temperatures below $T_{m,SOI} = 200\text{ °C}$ deposit growth was very slow, Fig. 5.15. Deposits formed up to 210 °C retained a moist consistency and could easily be washed away. The available exhaust enthalpy was hardly sufficient to evaporate the entire water content of the UWS. In the range $200\text{...}290\text{ °C}$, accumulation remained on a constant and comparatively low level. Around 290 °C deposit growth was highly dependent on the injection rate. Above, it was very pronounced in all cases. The change of the accumulation characteristic was closely related to that of the critical injection rate, Fig. 5.13. Above 300 °C , the critical injection rate already exceeded 50 mg/s . However, as soon as the Leidenfrost effect could not be maintained, intensive wall wetting and subsequent deposit formation was triggered. In this temperature range, the critical injection rate is to be seen as a sharp boundary, which marks the onset of noticeable deposit formation.

5.4 Deposit Content and Decomposition

A set of representative deposits was selected in order to clarify the impact of the boundary conditions, under which the deposits were formed, on their thermal stability. In this section, the deposit content and the decomposition behaviour of the individual components are studied. Deposits are characterised and categorised with respect to their formation and decomposition temperatures. Critical thresholds are provided and constitute the basis for the assessment of the deposit severity in Section 5.5.

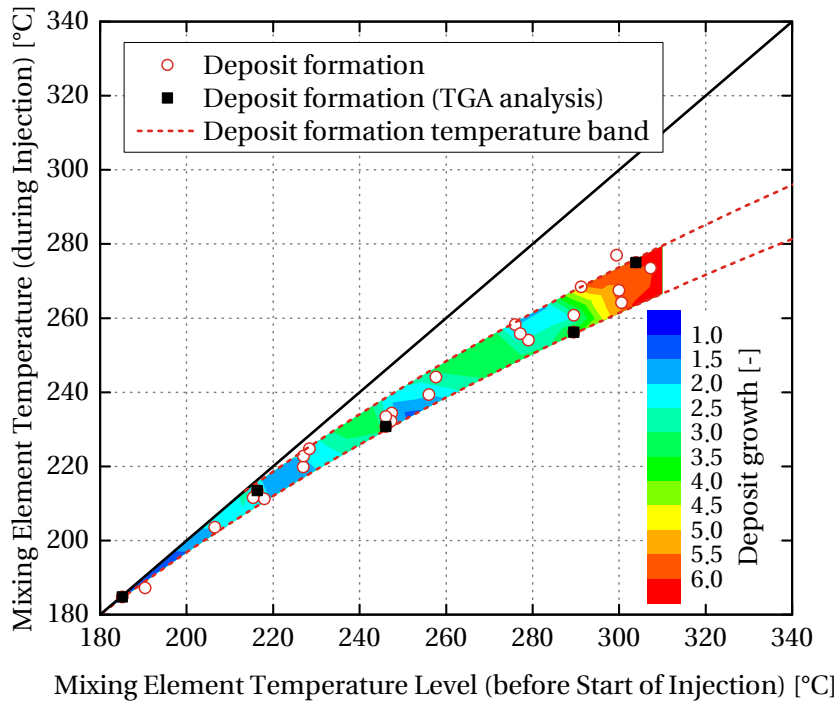


Figure 5.15: Deposit growth as a function of the mixing element temperature level. Deposit formation temperature band adopted from Fig. 5.12.

5.4.1 Chemical Content Analysis

The temperatures at which individual deposit components decompose at noticeable rates vary significantly, Tab. 5.2. Hence, it is evident that the temperature-stability of individual deposits is determined by its composition. The analysed set of deposits covered a wide range of deposit formation temperatures T_s between 185 °C and 275 °C. Samples were named according to the operating point at which they were generated, Tab. 5.3.

Thermogravimetry allowed a qualitative and, to a limited extent, also a quantitative assessment of the deposit composition. The analysis was based on the comparison of the decomposition behaviour of single deposits against that of the major reference substances, Fig. 5.16. Major components of the individual deposits were identified in particular by interpreting characteristic temperatures and mass

Table 5.2: Decomposition temperatures of pure reference substances based on thermogravimetric analyses: start of decomposition (SD, ≥ 2 % mass loss), decomposition at noticeable rates (ND, $|dm| \geq 8\%/min$) and sample depletion ($m \leq 1$ % of the original sample mass). Heating rate 10 °C/min, purge gas N_2 , sample mass 3.9 mg.

Process	SD [°C]	ND [°C]	Depletion [°C]
Urea decomposition	151	174	377
Biuret decomposition	195	203	400
Cyanuric acid decomposition	278	326	372
Ammelide decomposition	348	382	664
Ammeline decomposition	348	410	702
Melamine decomposition	250	287	337

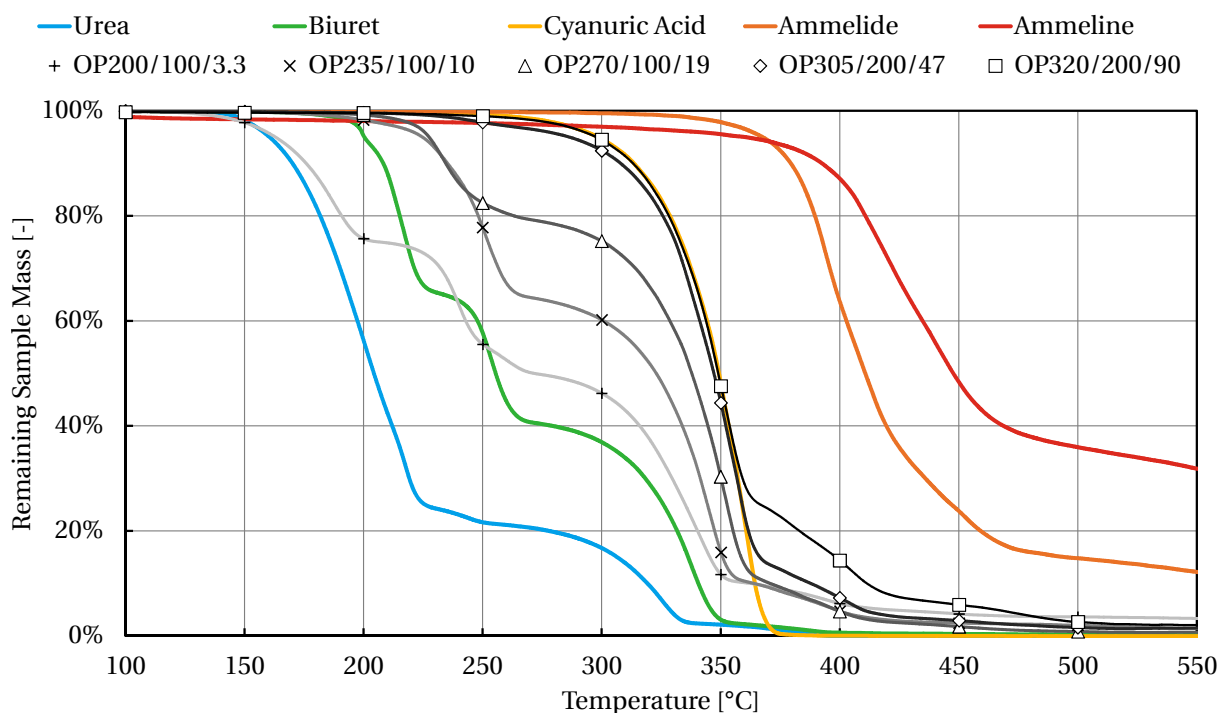


Figure 5.16: Thermogravimetric analyses of deposit samples and reference substances. Residual weight of the samples marked with symbols every 50 °C in order to facilitate the identification and comparison. Heating rate 10 °C/min, purge gas N₂, sample mass 3.9 mg.

shoulders, under consideration of the underlying chemistry, Tab. 5.3.

The evidence suggests that deposits can be classified into two categories, based on their formation temperature T_D . Up to 231 °C, deposits were characterised by the degree of conversion of urea and biuret into cyanuric acid (*low-temperature deposits*), Tab. 5.3. The amount of temperature-stable components amounted up to around 8 % of the sample mass. In case of deposition temperatures as low as 256 °C urea and biuret fractions were negligible. Cyanuric acid became the major component and deposits were characterised by the degree of conversion of cyanuric acid into the temperature-

Table 5.3: Overview of formation temperatures and content of a representative set of deposits based on thermogravimetric analyses. Heating rate 10 °C/min, purge gas N₂, sample mass 3.9 mg.

Operating point	$T_{m,SOI}$ [°C]	T_s [°C]	Major components
OP 200/100/3.3	185	185	urea, biuret, cyanuric acid, ≈ 8 % of ammelide and ammeline
OP 235/100/10	216	213	biuret, cyanuric acid, ≈ 8 % of ammelide and ammeline
OP 270/100/19	246	231	biuret, cyanuric acid, ≈ 8 % of ammelide and ammeline
OP 305/200/47	290	256	cyanuric acid, traces of biuret, ≈ 12 % of ammelide and ammeline
OP 320/200/90	304	275	cyanuric acid, ≈ 24 % of ammelide and ammeline

stable components ammelide and ammeline (*high-temperature deposits*). Their amount added up to around 12 % (OP 305/200/47) and 24 % (OP 320/200/90). The comparison of the decomposition behaviour of the deposits against that of ammelide and ammeline provides an insight into the impact of their amount on the depletion process. If their fraction within the deposit increases, the depletion temperatures and timescales rise significantly.

Evidently, thermogravimetric analyses based on a constant heating rate provide a consistent framework for the analysis of the deposit content. An excellent comparability between samples and reference substances was ensured by maintaining the initial sample masses constant. However, due to the fact that deposit decomposition in exhaust systems rarely involve constant heating and temperatures as high as 800 °C, a separate measurement campaign was necessary in order to systematically evaluate decomposition timescales.

5.4.2 Decomposition Behaviour

Decomposition timescales are highly dependent on the deposit composition as well as on the temperature to which the sample is heated. The exhaust temperature level may exhibit significant variations, particularly in urban traffic. As a consequence, periods with temperatures sufficiently high for deposit decomposition may be short. In order to reflect this situation, individual deposit components were heated with 100 °C/min to the desired temperature, which was then maintained for 60 min. Depletion within the single minute range was assumed as a criterion for fast sample decomposition.

The results support the classification of deposits based on their fraction of temperature-stable components. The evaluation of the decomposition timescales proves that deposits may decompose rapidly at temperatures as low as 350 °C, if their major components are urea, biuret and cyanuric acid (low-temperature deposits), Tab. 5.4. However, fast decomposition may require a significant increase of the temperature level of up to 700 °C if ammelide and ammeline accumulate within the deposit (high-temperature deposits). The decomposition behaviour of the temperature-stable components is dominated by ammeline, as ammelide depletion was always achieved earlier compared to ammeline (data not shown).

A review of the decomposition timescales furthermore demonstrated that both urea as well as biuret decomposition were significantly accelerated above 250 °C. The decomposition of either of these promotes the formation of ammelide and ammeline, which may also be seen as an explanation for the abrupt increase of the fraction of temperature-stable components in deposit samples formed above 250 °C, see Tab. 5.3. In case of pure urea, sample depletion required 548 s whereas 98 % of the sample were already decomposed after 36 s. Again, this confirms that minor amounts of ammelide and ammeline, which were formed during urea decomposition, may be decomposed even at temperatures as low as 350 °C.

5.5 Deposit Severity

Even though deposits may form at all temperatures up to the deposition limit, not every deposit necessarily poses a threat to reliable system operation. In general, the potential severity of a deposit increases with its formation temperature. In this section, the actual deposit severity ds shall be assessed and classified through the comprehensive interpretation of the available data on solidification temperatures and timescales, deposit accumulation and content, as well as the decomposition behaviour of the individual deposit components, see Tab. 5.5.

Table 5.4: Decomposition timescales of pure substances at temperatures up to 700 °C according to TGA measurements. Heating rate 100 K/min, residence time at target temperature 60 min, purge gas N₂, sample mass 2.6 mg. Sample depletion was assumed when the residual weight had dropped to 1 % of the original mass.

Component	Weight [mg]	Temp. [°C]	Res.wght. [mg/mg]	Time [s]
Urea	2.670	150	33.7%	3600
Urea	2.680	200	24.1%	3600
Urea	2.683	250	20.4%	3600
Urea	2.685	300	10.4%	3600
Urea	2.660	350	2.0%	36
Urea	2.660	350	1.0%	548
Biuret	2.658	200	62.0%	3600
Biuret	2.630	250	56.3%	3600
Biuret	2.630	300	8.2%	3600
Biuret	2.590	350	1.0%	62
Cyanuric Acid	2.621	300	1.0%	2106
Cyanuric Acid	2.605	350	1.0%	87
Ammeline	2.507	500	19.1%	3600
Ammeline	2.655	600	1.0%	1816
Ammeline	2.650	700	1.0%	59

At low temperatures, deposit formation can hardly be prevented, as the critical injection rates are very low. However, deposits form and accumulate slowly, and a moderate temperature increase is sufficient to trigger their decomposition. The tolerable injection rate increases with temperature. At the same time, the trends observed with respect to the solidification timescales, deposit growth and composition equally intensify the deposit severity. As a consequence, high temperature operating points combine short solidification timescales, rapid accumulation and temperature-stable deposits. Compared to the low-temperature operating points, they are characterised by an abrupt initiation of deposit formation, if the critical injection rate is exceeded.

Below 160 °C neither urea decomposition nor undesired secondary reactions proceed at noticeable rates. Undecomposed urea may recrystallise or remain within the system in the form of a melt. Deposits are expected to largely maintain a moist state, remain soluble in UWS, and deposit slowly. As the reducing agent remains stored in its original state, it may easily undergo thermolysis upon heating to 350 °C. Therefore, these two types of deposits exhibit the lowest severity $ds = 0$.

Between 160 °C and 250 °C, the chemical stability of deposits gradually increases and their content can be characterised by the degree of conversion of urea and biuret into cyanuric acid. However, up to 175 °C the deposit content remains practically limited to urea and biuret. Deposit severity is specified as $ds = I$. Above, the cyanuric acid content gradually increases and deposits contain minor amounts of ammelide and ammeline. Nevertheless, the solidification timescales are still large and deposits grow slowly. Up to 210 °C, they retain a rather moist consistency and can easily be washed away ($ds = II$). The fraction of temperature-stable components remains on a constant low level and deposit accumulation is still fairly average up to approx. 250 °C ($ds = III$). As individual deposits may vary significantly with respect to their mass and composition, the specification of any universal min-

Table 5.5: Classification of the deposit severity ds based on the solidification temperature T_s and timescale t_s , average deposit growth dg , deposit composition, and the expected decomposition temperatures T_{dcmp} . Temperature stable deposit components include ammelide and ammeline.

ds [-]	T_s [°C]	Main components	T.-stable [mg/mg]	t_s [s]	dg [-]	T_{dcmp} [°C]
0	$T \leq 133$	urea (crystallised)	$\ll 1\%$			≥ 350
0	$133 < T \leq 160$	urea (melt)	$\ll 1\%$			≥ 350
I	$160 < T \leq 175$	urea, biuret	$< 1\%$			≥ 350
II	$175 < T \leq 210$	urea, biuret, cyanuric acid	$\leq 10\%$	> 300	1...2	≥ 350
III	$210 < T \leq 250$	urea, biuret, cyanuric acid	$\leq 10\%$	$f(T_e, \dot{m}_e, \dot{m}_{UWS})$	2...3	≥ 350
IV	$250 < T \leq 270$	cyanuric acid, ammelide, ammeline	$> 10\%$	$f(T_e, \dot{m}_e, \dot{m}_{UWS})$	3...4	600...700
V	$270 < T$	cyanuric acid, ammelide, ammeline	$> 10\%$	< 160	5...6	600...700

imum decomposition rate or maximum decomposition timescale would be questionable. However, the structure of deposits with a maximum severity of $ds = III$ is dominated by components exhibiting rapid decomposition upon heating to 350°C . Furthermore, as they are not expected to form in large amounts, it appears safe to assume that the temperature increase will lead to a disintegration of the deposit structure. Urea, biuret, and cyanuric acid melt and decompose. The small remaining fragments of solid ammelide and ammeline will be distributed or transported off the system in powdery form, both rendering them harmless to reliable system operation.

Above 250°C , deposits can be characterised by the degree of conversion of cyanuric acid into ammelide and ammeline. The fraction of temperature-stable components rises and deposits accumulate increasingly fast. Above 270°C , this trend coincides with fast solidification and accumulation. Therefore, this temperature was taken as a threshold to distinguish between high and very high deposit severity, $ds = IV$ and $ds = V$, respectively. Temperatures in the range $600\text{...}700^\circ\text{C}$ are required to achieve fast decomposition of the ammelide and ammeline content.

The classification allows a reasonable differentiation of the deposit severity. The effective decomposition rates and timescales may depend on the actual deposit mass, its surface to volume ratio, the operating conditions, and the system setup. However, the underlying chemistry can be regarded as universal. Hence, the classification system may be used to complement a (quantitative) model-based prediction of excess wall film with a (qualitative) temperature-dependent evaluation of the deposit severity.

Chapter 6

Modelling Deposit Formation

The mechanisms of wall film transport and deposition have been shown in Chapter 5. The knowledge gained about the major influence factors, which promote or impede deposit formation, shall now be combined with data from the literature into an empirical approach to predict deposits based on the physical properties of the wall film. The validated CFD model presented in Section 4.2 was used to simulate the propagation of the wall film both in the underbody type and the close-coupled type SCR systems.

6.1 Modelling Concept

The validity of correlations between single impact factors and deposit formation is usually limited to a specific SCR system and can hardly be generalised. Even if different systems exhibit the same trends, thresholds, such as the critical injection rate, cannot arbitrarily be transferred due to the complex interaction of system design, operating, and boundary conditions. Therefore, a predictive modelling concept has to consider all relevant impact factors and their interaction. In the first place, this includes an accurate representation of the mixing section geometry, spray characteristics, and targeting. Deposit formation proceeds on timescales in the minute to hour range, which, to the present day, cannot be captured with reasonable computational effort. Therefore, the presented model focusses on the interpretation of liquid film propagation and properties, in order to assess the deposit formation risk. This means that, in the second place, droplet wall interaction, wall film formation, propagation, and evaporation, as well as the convective and turbulent dispersion of gaseous species have to be considered precisely. For this purpose, a validated CFD model for the simulation of UWS preparation in automotive SCR systems was used, as introduced in Section 4.2. The framework readily allows the simulation of ammonia homogenisation to be extended by the prediction of the deposit formation risk and can cover the required timescales in the double-digit second range. The base model is capable of predicting excess wall film and its propagation. As a consequence, it intrinsically captures the permanent wall wetting threshold and fundamental impact factors, such as the specific impingement mass flow rate or wall film dynamics. The representation of all relevant heat fluxes contributes to the accurate simulation of wall film evaporation and heat up.

As a **first step**, the prediction of the deposit formation risk requires the **identification of all potential deposit locations**. As soon as the temperature of the impingement target has attained a steady state, the amount and location of the undecomposed excess film becomes evident. While persisting film is regarded as precursor of deposit formation, it depends on the local conditions whether or not deposits are eventually formed. Therefore, the **second step** involves the **systematic analysis of the**

wall film properties with respect to the mechanisms which promote or impede deposit formation. Continuous impingement and different forms of wall film dynamics, e.g. the fluctuation of the film thickness, have been reported to impede deposit formation locally. These mechanisms have to be formulated in the form of mathematical correlations, and the respective threshold values have to be calibrated. Ultimately, the local wall film temperature decides on the relevance of individual deposition pathways. Below its decomposition temperature, urea may recrystallise. The crystallisation limit can be determined based on the UWS phase diagram. Above the urea decomposition temperature, the relevant deposit formation chemistry is determined by the temperature and, up to approx. 300 °C, the availability of gaseous isocyanic acid. Eventually, the simultaneous interpretation of temperature and HNCO concentration allows to draw conclusions on the composition and severity of a potential deposit.

6.2 Assessment of the Deposit Formation Risk

The deposit formation risk model will be explained based on the comparison of two specific areas on the mixing element of the underbody type SCR system, Fig. 6.1. Both areas were exposed to continuous wall wetting at OP 200/100/35. However, the experiments showed that even after 4 h the upstream area (marked in green) did not exhibit noticeable deposit formation in contrast to the rear blade side (marked in red). Due to wall time limitations, it was not possible to capture the entire experiment duration in CFD. The simulated time was limited to 40 s, equivalent to 120 injection events. It will be shown in the present chapter that this was sufficient for a comprehensive analysis of the deposit formation risk based on the physical properties of the wall film. The consecutive steps of the analysis were

1. **identification of potential deposit locations**
(wall film pathways)
2. **analysis of the wall film dynamics**
(impingement areas, wall film mass fluctuations, thickness, and velocity)
3. **evaluation of the deposit formation risk**
(wall film temperature level, urea concentration, and HNCO concentration)

and will be addressed in the following sections. A deposition risk will be derived and the deposit severity will be estimated.

6.2.1 Identification of Potential Deposit Locations

The optical investigations on the mechanisms of deposit formation confirmed that liquid film is to be seen as a precursor of deposit formation and showed that potential deposition locations were found alongside liquid film pathways, Section 5.2.1. Fig. 6.1 shows the wall film distribution after 120 injection events. Both areas were exposed to wall wetting. Yet, major deposits were only found on the reverse side of the rear blade, especially at the upper and rear blade edge. The simulated time was sufficient to capture both the pathways and properties of the wall film, as well as solid cooling. Despite this, the exact wall film pathways were subject to minor variations due to statistical variations of the spray targeting, turbulent droplet dispersion, as well as fluctuations of the flow field. This was especially relevant for injectors with short pulse durations, broad spray cone angles and high injection frequencies, such as the hollow-cone injector, Section 4.1.2 and Tab. 4.5. However, it did not affect the major pathways, but was limited to peripheral areas with very low wall film thickness. In order to reflect this behaviour, the intersection of the areas covered by wall film at the end of all injection events within the last second of the simulated time, i.e. after the 118th, 119th and 120th

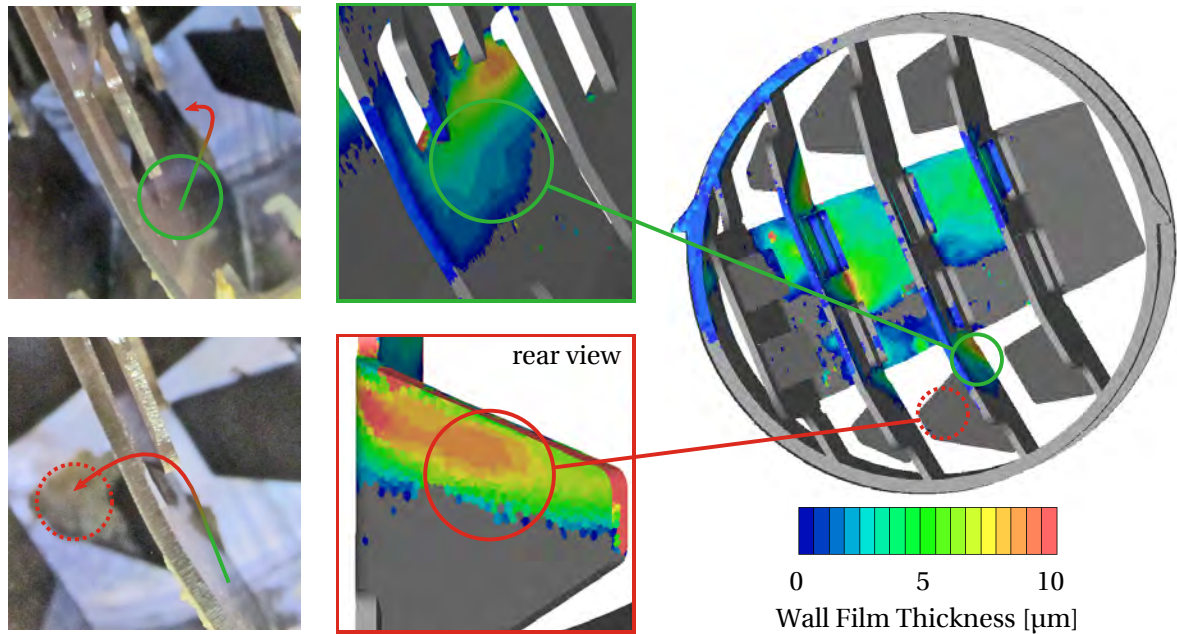


Figure 6.1: Choice of two areas exposed to wall wetting: upstream area without deposit formation (marked in green) and rear blade face with deposit formation (marked in red). OP 200/100/35. Left-hand side shows deposit formation on the mixing element after 4 h. Right-hand side shows simulated wall film thickness on the mixing element after 40 s. Dotted lines indicate deposit formation and/or wall wetting on the rear side of the tagged blade, arrows indicate fluid film pathways.

injection event, was taken as a basis for the evaluation of the deposit formation risk and denoted *final footprint*. In order to guarantee reasonable results, cells were only classified as wetted if the film exceeded a minimum thickness of $d_{n,c}$. The development of the overall wall film mass on the upstream area and the rear blade side proves that 40 s of calculated time were enough to attain a steady state, Fig. 6.2. The mass fluctuation on the upstream area reflects the periodic evaporation of the UWS water content. Comparison with Fig. 6.3 shows that this process is closely linked to the development of the wall film temperature, which is plausible as the local evaporation rates are highly dependent on the actual wall film temperature.

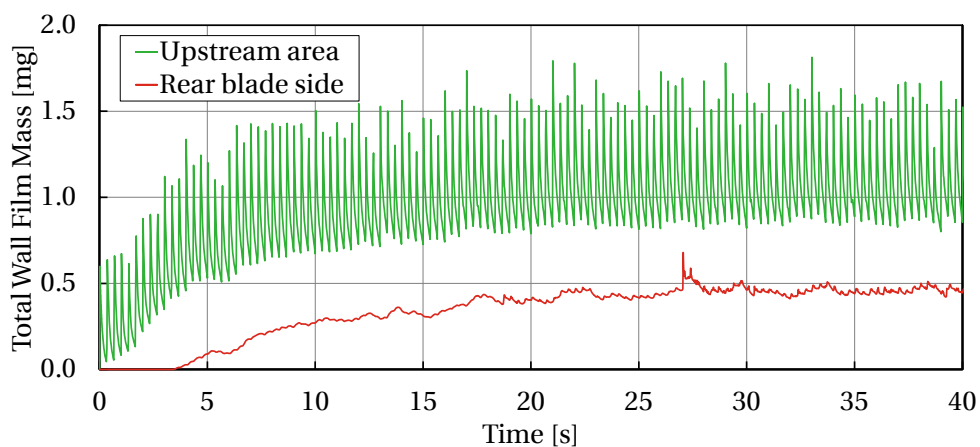


Figure 6.2: Development of the total wall film mass on the upstream area and the rear blade side. OP 200/100/35, initial 40 s after SOI.

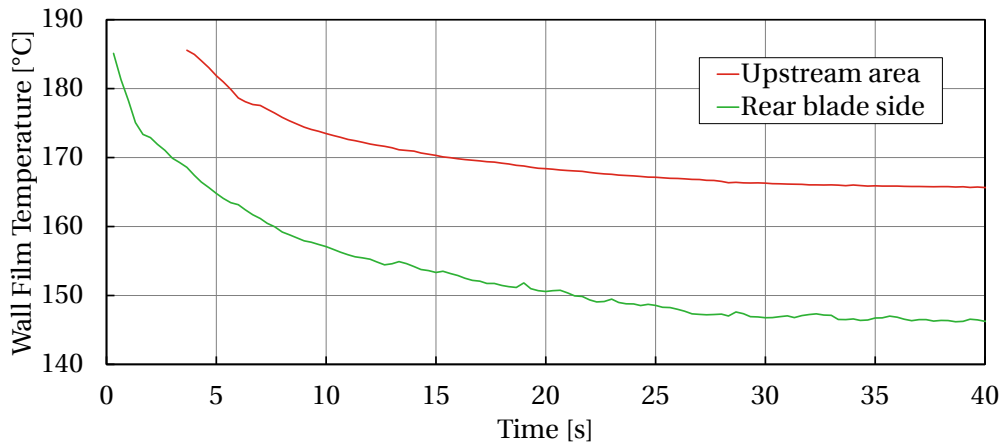


Figure 6.3: Development of the average wall film temperature on the upstream area and the rear blade side. OP 200/100/35, initial 40 s after SOI.

6.2.2 Analysis of the Wall Film Dynamics

The formation of deposit nuclei was effectively impeded in **impingement areas** as the ongoing droplet wall interaction induced intense liquid film dynamics, continuous dilution and mixing of present wall film. While the supply with fresh UWS was due to the periodic injection, the formed film was removed from the area through trickling and/or evaporation. To identify the corresponding areas based on the CFD results, the total instantaneous liquid film mass on the mixing element surface was monitored during the first injection event. Fig. 6.4(a) exemplarily shows the total wall film mass during the first injection event and proves that noticeable wall wetting only occurred on the upstream area. The union of the wetted areas in a 4 ms period around the time of maximum wall film mass, $t_{if,max} \pm 2$ ms, during the first injection, was denoted *initial footprint*. The extension of the evaluation to a 4 ms period was necessary to capture the initial footprint of injectors featuring very short pulse durations, such as the hollow-cone injector ($t_{pulse} = 1.6$ ms). However, it had negligible impact on the assessment of the initial footprint of the 3-hole and 6-hole injectors. Following the argumentation in Section 5.2.2, it was assumed that deposit formation would not be initiated in this area, which was therefore classified as *no deposition risk*. In the case at hand, the maximum wall film mass was attained 22 ms after SOI, Fig. 6.5. While a distinct initial footprint was identified on the upstream area, the rear blade side exhibited only negligible wall wetting from secondary impingement during the first injection event.

Intense wall film dynamics were found to impede deposition not only in the area of the initial footprint, but also in adjacent areas where existent liquid film was continuously diluted and mixed with fresh UWS. Fig. 6.4(b) clearly demonstrates that dilution effects were limited to the vicinity of impingement areas whereas further downstream the urea concentration approached 100 %. Wall film dynamics became apparent in the **fluctuations of the wall film mass**, see Fig. 6.2. While the respective areas were supplied with excess film from impingement, the formed film was removed from the area through trickling and/or evaporation. A coefficient was introduced to quantify the extent of liquid film dynamics. It was calculated based on the maximum and minimum mass on each wetted cell face during a specified period at the end of the simulated time relative to the liquid film mass $m_{wf,0}$ at the beginning of this period:

$$fd = \frac{\Delta m_{wf,max}}{m_{wf,0}} = \frac{m_{wf,max} - m_{wf,min}}{m_{wf,0}} \quad (6.1)$$

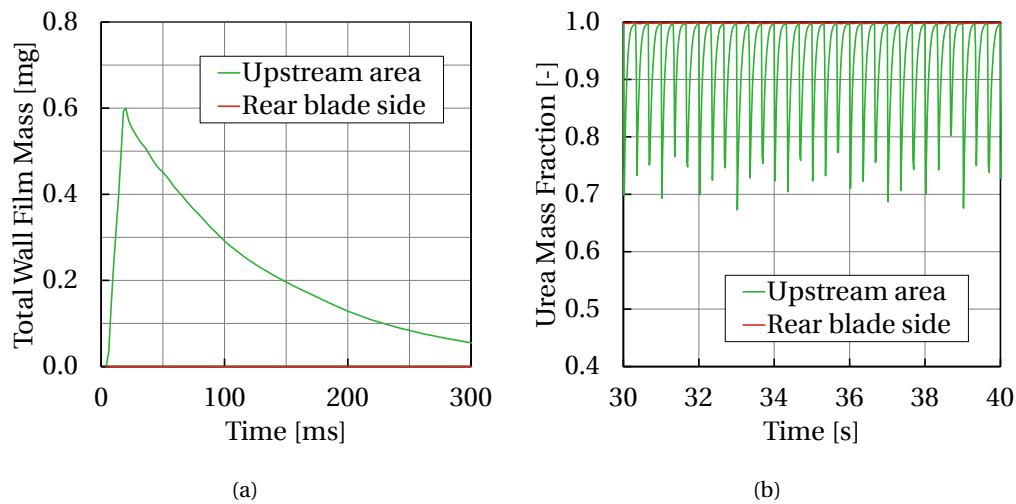


Figure 6.4: Development of the total wall film mass during the first impingement event (a, initial 300 ms after SOI) and wall film urea concentration (b, 30...40 s after SOI) on the upstream area and the rear blade side. OP 200/100/35.

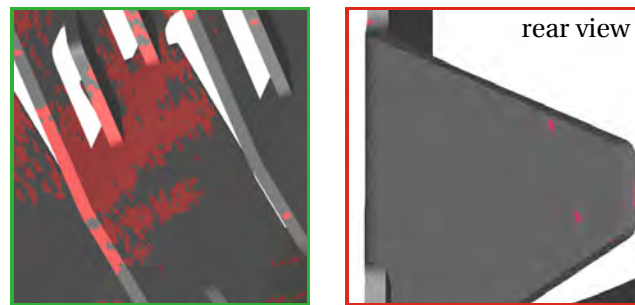


Figure 6.5: Visualisation of the initial footprint on the upstream area (left-hand side) and the rear blade side (right-hand side). OP 200/100/35, 22 ± 2 ms after SOI. Footprint marked in red, no scale applied.

In the presented case, a 2 s period from 38...40 s, equivalent to six injection events, was used as a basis for the analysis of wall film dynamics. Only cells which were wetted during the entire period were taken into account. The intensity of wall film dynamics is shown in Fig. 6.6. For increased wall film dynamics above a specified threshold value $fd \geq fd_c$, the corresponding areas were specified as *no deposition risk*.

Significant liquid film accumulation also impeded deposition locally due to the intense liquid film dynamics and the reduced evaporation rate. The effect was triggered at rear blade edges, manifested in the form of very high film thicknesses, and promoted droplet stripping and liquid film flipping onto reverse blade sides. Despite the continuous exchange of fluid film, the local film properties may remain constant. Therefore, areas with a liquid film thickness above a specified threshold $d \geq d_{s,c}$ were classified as *flipping, stripping*.

The experimental investigations furthermore showed that deposit formation was impeded in **thick films** which trickled **with high velocities**. Fig. 6.7 shows the velocity level at the end of the 120th injection event prior to the next burst of impinging droplets. In contrast to areas with intense wall film mass fluctuations, the continuous exchange of fluid film did not necessarily become visible in the form of periodically changing wall film properties. Areas of intense wall film movement were found on the rear part of the upstream area and extended onto the rear blade side. Liquid film which

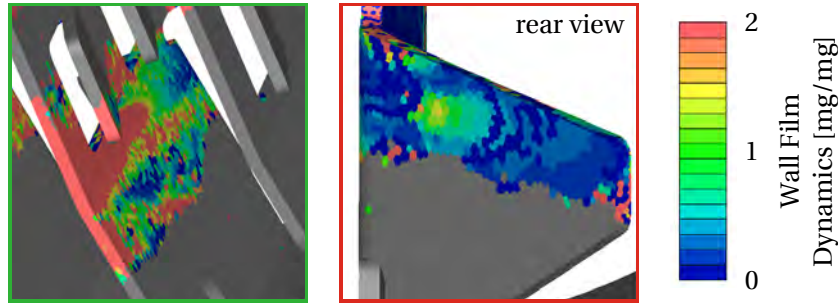


Figure 6.6: Visualisation of the wall film dynamics on the upstream area (left-hand side) and the rear blade side (right-hand side). OP 200/100/35, 38...40 s after SOI.

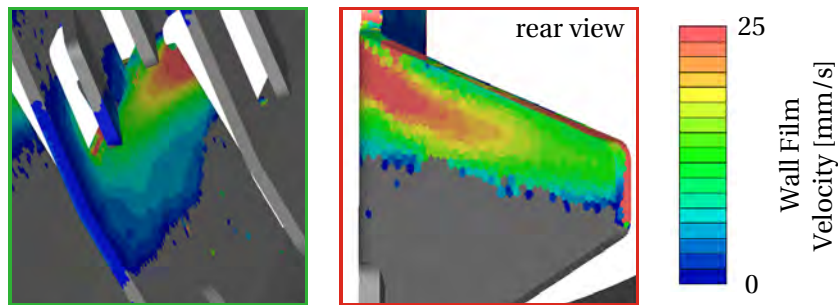


Figure 6.7: Visualisation of the wall film trickling velocity on the upstream area (left-hand side) and the rear blade side (right-hand side). OP 200/100/35, 40 s after SOI.

fulfilled both the requirement of an increased thickness $d \geq d_{t,c}$ and velocity $c \geq c_{t,c}$ was classified as *transport*.

The variety of the criteria shows that wall film dynamics manifest in different forms. Impingement and local wall film mass fluctuations do not necessarily imply high film trickling velocities or thicknesses. The respective areas may be permanently wetted but still not exhibit deposition formation due to the continuous dilution and mixing of the film. In contrast, the local conditions in accumulation areas or thick films with high trickling velocities may even remain constant. However, potentially formed deposit nuclei are continuously removed, as the local wall film is continuously exchanged. At the same time, the evaporation rates remain on a comparatively low level due to the low surface to volume ratios. Therefore, it is safe to assume that in such areas deposit formation is impeded only locally. In consequence, the eventual deposit locations are shifted to adjacent areas on the respective blades or to the downstream piping. In order to reflect this situation, these areas were classified as *transport/flipping/stripping* instead of *no deposition risk*.

6.2.3 Evaluation of the Deposit Formation Risk

The relevant deposit chemistry is primarily determined by the wall film temperature level T_{wf} , see Sections 2.2.1, 2.2.3 and 5.5. Three major regimes can be distinguished: urea crystallisation ($T_{wf} \leq 133\text{ °C}$), slow urea decomposition ($133\text{ °C} < T_{wf} < 160\text{ °C}$) and fast urea decomposition, possibly along with secondary reactions ($T_{wf} \geq 160\text{ °C}$).

The temperature distribution of the wall film after 120 injection events is shown in Fig. 6.8. Droplet impingement on the front side of the mixing element intensively cooled the blades locally, despite the fact that this area was exposed to direct incident exhaust flow. This was attributed to the fact that the water content evaporated with minimum temporal delay on the primary impingement areas. The

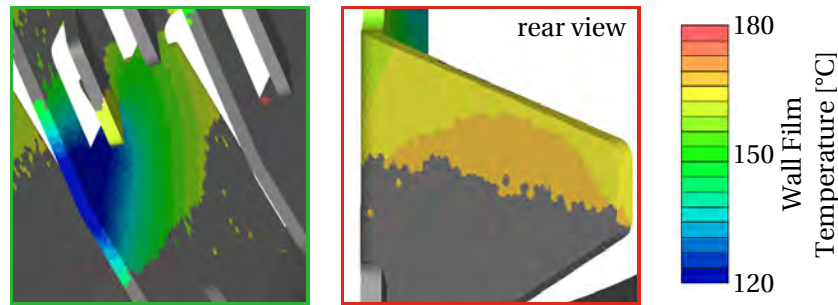


Figure 6.8: Visualisation of the wall film temperature on the upstream area (left-hand side) and the rear blade side (right-hand side). OP 200/100/35, 40 s after SOI.

UWS then trickled downstream towards the rear blade side and was continuously heated up, reaching temperatures in the range 160...170 °C. In contrast, the film temperature in the upstream area for the most part ranged from 120 °C to 160 °C. Thus, all of the three major deposit chemistry regimes were relevant. The fact that the mixer was subject to intense cooling as a result of wall wetting and continuous liquid film evaporation underlines the importance of choosing the simulation time high enough to capture solid cooling and of considering thermal mass and heat conduction within the solids.

Urea Crystallisation ($T_{wf} \leq 133$ °C)

In case the wall film temperatures remain or drop below 133 °C urea may recrystallise if its concentration rises above the crystallisation limit, see phase diagram in Fig. 2.14. Since the critical concentration is temperature-dependent it was calculated cell-wise. Based on the local comparison between actual and critical urea concentrations within the wall film, areas which complied with $Y_{urea} \geq Y_{urea,c}(T)$ were classified as *crystallising urea*. Wall film with a urea concentration below the crystallisation limit was classified as *crystallisation risk* since urea decomposition and secondary reaction rates were assumed negligible in this temperature range. It is worth mentioning that the liquid film urea concentration at the end of each injection event was above 96 %. In the area of primary impingement the concentration temporarily decreased during impingement, whereas on the rear blade side it permanently remained on a very high level.

Slow Urea Decomposition (133 °C < $T_{wf} \leq 160$ °C)

Urea decomposes at temperatures above its melting temperature 133 °C. However, since neither decomposition at significant rates nor noticeable by-product formation was observed up to 160 °C, wall film with the mentioned properties was classified as *urea decomposition*.

Fast Urea Decomposition / Secondary Reactions ($T_{wf} > 160$ °C)

If the wall film temperatures reach 160 °C, urea decomposition rates increase and secondary reactions start to become evident. The formation of by-products, such as biuret, is bound to the availability and concentration of gaseous HNCO. Therefore, in case of low isocyanic acid concentrations $X_{HNCO} < X_{HNCO,c}$ above the wall film, the corresponding cells were classified as *urea decomposition*. In the opposite case, $X_{HNCO} \geq X_{HNCO,c}$, the isocyanic acid concentration was assumed high enough to trigger the formation of by-products. Following the categorisation proposed in Section 5.5, five

deposition risk categories were implemented according to the respective temperature levels and corresponding deposit components, see Tab. 5.5. In case the critical HNCO concentration was attained above the wall film, the corresponding cells were classified as *deposition risk 1...5* assuming the temperature thresholds given in Tab. 5.5, where higher numbers indicate higher deposit severity. As it was not possible to measure the critical isocyanic acid concentration, it was calibrated empirically by comparing the predicted deposit locations with the measurement results.

It is worth mentioning that the NH_3/HNCO sources were shifted over time as solid cooling lowered the local evaporation rates, resulting in the evolution of wall film trickling pathways. While the main sources were in the vicinity of the front face of the mixing element during the first injection events, they were shifted downstream as time was progressing, see Fig. 6.9. The release of gaseous NH_3/HNCO furthermore increased the local concentrations downstream their origin. Due to the transient nature of the injection process, the production rates of gaseous species were subject to continuous fluctuations. In order to reflect this, the HNCO concentration was time averaged over a 2 s period from 38...40 s, which has been established as a common strategy for the evaluation of ammonia uniformity at the catalyst [32, 129], Fig. 6.10.

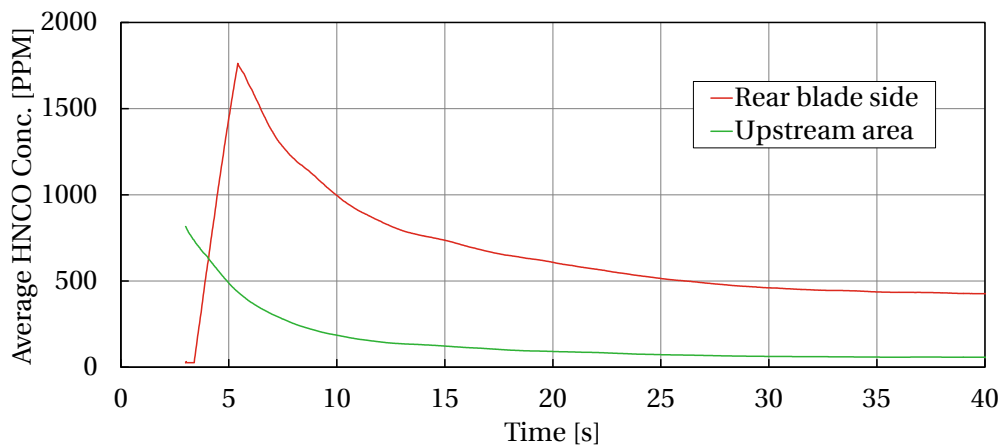


Figure 6.9: Development of the average isocyanic acid concentration above surfaces exposed to wall wetting on the upstream area and the rear blade side. OP 200/100/35, 3...40 s after SOI, concentration time-averaged over 2 s periods prior to the respective time of evaluation.

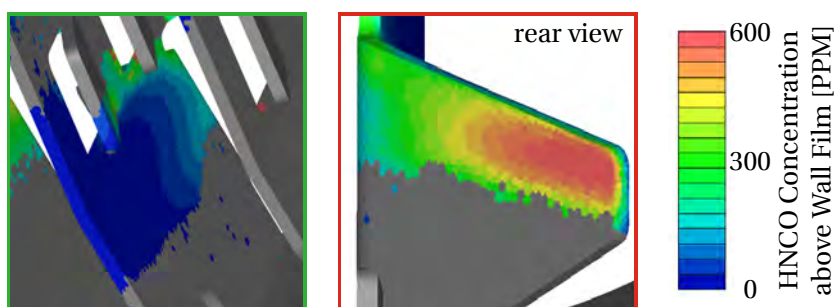


Figure 6.10: Visualisation of the time-averaged gaseous HNCO concentration above the wall film on the upstream area (left-hand side) and the rear blade side (right-hand side). OP 200/100/35, 38...40 s after SOI.

Assessment of the Deposit Formation Risk

The required set of model parameters was empirically calibrated based on the available measurement data from the underbody type and close-coupled type SCR systems, Tab. 6.1. The individual analysis steps were integrated into an automated post-processing routine which visualised the deposit formation risk based on the presented classification system, Fig. 6.11. The analysis showed that the upstream area did not bear any deposition risk. In the major part of the wetted area, deposit formation was impeded due to the high liquid film dynamics. In adjacent areas wall film was too cold to exhibit noticeable by-product formation and urea was expected to decompose slowly. However, wall film was heated up and transported off this area onto the rear blade side where the risk of deposit formation was non-negligible due to the increased HNCO concentrations. As the wall film temperature remained below 210 °C, the lowest deposition risk level was predicted. This implied slow growth which was confirmed by the low amount of deposits obtained in the experiment after 4 h, Fig. 6.1. The deposit must have contained mainly urea and biuret. The simulation results further indicated a wall film flipping and droplet stripping risk on the upper and rear blade edge which was in line with the experimentally observed formation of deposits on the reverse blade side and the downstream piping, Figs. 6.1 and 5.2(d).

The observations showed that intensive cooling itself is not necessarily a problem since the corresponding areas were also exposed to intensive liquid film dynamics which prevented deposition. This provides further evidence that deposits form because excess wall film is transported off the impingement areas, concentrates and is heated up before reaching remote regions where conditions may be suitable for deposit formation. The local deposit formation risk was always interpreted based on the locally predominating prediction. The impact of single (isolated) cells, or very small areas, was deemed to be of subordinate importance, if they exhibited a risk significantly deviating from that of the surrounding areas.

The presented method yielded a plausible prediction of the deposit formation risk on two characteristic areas based on a CFD simulation of the physical properties of the wall film. Therefore, the

Table 6.1: Calibration of thresholds for the deposit formation risk model. Set of values consistently used throughout the entire study.

Threshold	Quantity	Value
Initial footprint evaluation period	Δt_{if}	± 2 ms
Final footprint evaluation period	Δt_{ff}	2 s
HNCO concentration averaging period	Δt_{HNCO}	2 s
Wall film dynamics evaluation period	Δt_{fd}	1 s
Numerical wall film thickness threshold	$d_{n,c}$	0.01 μm
Thick wall film thickness threshold	$d_{t,c}$	10 μm
Accumulated wall film thickness threshold	$d_{s,c}$	100 μm
Wall film trickling velocity threshold	$c_{t,c}$	20 mm/s
High liquid film dynamics threshold	fd_c	1 mg/mg
Critical HNCO concentration threshold	$X_{HNCO,c}$	200 PPM
Urea crystallisation temperature	$T_{urea,c}$	132.6 °C
Lower temperature threshold $ds = I$	$T_{1,min}$	160 °C
Lower temperature threshold $ds = II$	$T_{2,min}$	175 °C
Lower temperature threshold $ds = III$	$T_{3,min}$	210 °C
Lower temperature threshold $ds = IV$	$T_{4,min}$	250 °C
Lower temperature threshold $ds = V$	$T_{5,min}$	270 °C

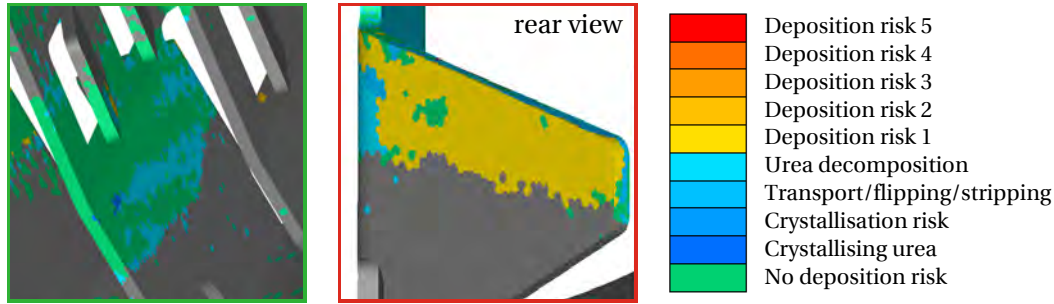


Figure 6.11: Visualisation of the deposit formation risk on the upstream area (left-hand side) and the rear blade side (right-hand side). OP 200/100/35, 40 s after SOI.

next logical step was to test the accuracy of the deposit formation risk for the entire mixing element. Furthermore, it was desirable to verify whether the method was capable of assessing the impact of mixing element and mixing section geometry, injector, and operating conditions, such as exhaust temperature and injection rate, see Section 6.3.

6.2.4 Acceleration of Solid Cooling

The model presented in Sections 6.2.1-6.2.3 evaluates the deposit formation risk at a specified point of time. The validity of the prediction depends on whether the simulated time covers the evolution of solid cooling and, hence, fluid film pathways up to a point at which they have reached a steady-state in the area of interest. The simulation time necessary to reach a steady-state may differ depending on the investigated area and operating conditions. Optical investigations on the close-coupled type SCR systems revealed that the timescales of wall wetting at the location of subsequent deposit formation ranged between 2 s and more than 60 s. It was dependent on the applied mixing element and doser and increased noticeably if the injection rate was reduced from 60 mg/s to 35 mg/s. However, since the simulated time is often limited by the acceptable wall time and available computing power, it was set to a maximum of 40 s. In order to capture the evolution of the wall film pathways within the given timeframe, potential acceleration methods were reviewed.

It was the premise for the optimisation to reduce the simulation wall time while maintaining a consistent thermodynamic behaviour of the fluid and liquid phase and without modification of the exhaust system geometry. An optimisation of the numerical framework, e.g. by increasing the time step sizes or lowering mesh size, is limited by issues of precision and stability. A modification of the dosing strategy, e.g. by increasing the static mass flow rate of the injector, the injection rate and/or dosing frequency, would impact the cooling behaviour and render statements about critical injection rates impossible. Tests with continuous injection led to an exaggeration of the lateral liquid film spreading (results not shown) and thus provided an incorrect prediction of the liquid film pathways. As a consequence, a significant reduction of the wall time requirements, while maintaining the modelling depth, was deemed possible only by the application of similarity principles.

Consistency of the flow field can be achieved by maintaining the Reynolds number $Re = \rho_f c l_f / \mu_f$ constant, where ρ_f , μ_f , and c are density, dynamic viscosity, and velocity of the fluid, respectively, and l_f is a characteristic length of the fluid domain. Consistent heat transfer can be achieved by maintaining the Prandtl number $Pr = \mu_f c_{p,f} / \lambda_f$, the Biot number $Bi = \alpha l_s / \lambda_s$ and the Nußelt number $Nu = \alpha l_f / \lambda_f$ constant, where $c_{p,f}$ and λ_f are the specific heat capacity and the thermal conductivity of the fluid, respectively, λ_s the thermal conductivity of the solid, l_s a characteristic length of the solid domain and α the specific heat transfer coefficient. Unsteady heat flux problems are characterised

by an identical development of the temperature field, if the Fourier number Fo is used as temporal coordinate [150]. An identical temperature field may therefore be observed for

$$Fo = \frac{\lambda_s}{c_{p,s}\rho_s} \frac{t}{l_s^2} = \text{const.} \quad (6.2)$$

where $c_{p,s}$ and ρ_s are the specific heat capacity and the density of the solid, respectively.

The comparison of Figs. 6.2, 6.3 and 6.9 demonstrates that the development of wall film mass and temperature, as well as the isocyanic acid concentration above the wall film simultaneously attain a steady state. Evidently, a reduction of the solid density ρ_s reduces the simulated time required to capture the cooling processes and, hence, the evolution of the fluid film pathways. Alternatively, the covered timescale is increased if the simulated time is maintained constant. The modification of the solid density ρ_s can be understood as a reduction of the thermal mass and is similar to the approach chosen by Birkhold [101]. Naturally, it can be regarded as equivalent to reducing the specific heat capacity $c_{p,s}$ of the solid material. In order to confirm the validity of the strategy, a test case was set up using a flat plate. The exhaust temperature and velocity were set to 275 °C and 10 m/s. Injection was modelled according to the properties of the 6-hole injector, Tab. 4.5, and the dosing rate was set to 35 mg/s. Solid cooling was evaluated by averaging the temperature of the six impingement target areas. The solid density was varied in the range 0.1...1.0 $\rho_{s,\text{ref}}$. All variants approached a target temperature of approx. 186 °C, see Fig. 6.12 – 85 % of the temperature drop of was attained after roughly 7 s by reducing the solid density to 0.1 $\rho_{s,\text{ref}}$, compared to 40 s using the reference density. The faster the temperature field attains a steady-state, the earlier the temperature-dependent evaporation rates will remain constant and, hence, the earlier the evolution of the fluid film pathways will be completed. Both temperature and wall film mass attained a steady state after roughly 20 s instead of 70 s (data not shown). The reduction of the thermal mass also effected steeper temperature gradients upon impingement, Fig. 6.12. Therefore, an arbitrary reduction of the solid density is not recommendable in order to ensure the precise solution of the gradients without further reduction of the time step size. The applicability of the methodology was further tested by comparing the areas covered with wall film using the setup with mixer 1 and the 6-hole injector at OP 275/100/35 with and without density reduction. The test yielded similar wall film patterns after 7 s instead of 20 s, if ρ_s was set to 10 % of the original value (data not shown). Concludingly, the described methodology significantly extended the covered timescale for the prediction of the deposit formation risk based on the physical properties of the wall film. It was applied to all simulations of the close-coupled type SCR systems using an injection rate of 35 mg/s, i.e. in case of OP 275/170/35. In all other simulations liquid film pathways and solid cooling were well covered, even without applying the speed up methodology.

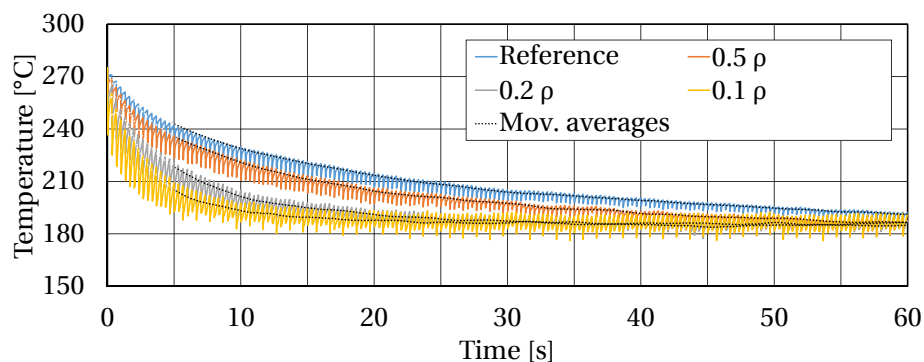


Figure 6.12: Solid cooling of the impingement target areas of a flat plate as a function of the solid density ρ_s . $T_e = 275$ °C, $c_e = 10$ m/s, 6-hole injector, 35 mg/s. Moving average (100 values) of the temperature shown above 10 s.

6.3 Validation of the Prediction Methodology

The applicability of the deposit formation risk model depends on whether it can assess the impact of major operating conditions and the system setup on deposit formation. Therefore, the prediction of the model was verified at different temperatures and injection rates, see Sections 6.3.1 and 6.3.2. In addition, it was tested for all combinations of two different mixing elements and spray characteristics, Section 6.3.3. The prediction accuracy was evaluated based on two major criteria: the extent of deposit formation, i.e. the amount of blades exposed to deposit formation, and the ability of the model to predict the location of the deposits and to explain the mechanisms in a given case. In the simulations, a risk for deposit formation was assumed if the respective areas exceeded the size of single cells.

6.3.1 Exhaust Temperature

The sensitivity of the prediction accuracy towards the exhaust temperature was tested on the underbody-type SCR system. Three major deposits were found during the measurement at 200 °C, Fig. 6.13 (solid, dashed and dot-dashed white lines). On the lower rear blade, the model prognosticated the formation of a deposit nucleus on the rear blade face (solid white line). The risk of film accumulation and flipping onto the front side of the blade manifested in the form of blue areas on the upper blade edge, Fig. 6.11. The correlation with the measurement results was excellent. Another major deposit was observed at the rightmost front edge (dashed white line). The model predicted a deposit nucleus on the left-hand side of the corresponding blade. In the measurement, this was confirmed by the position of the trickling pathways. Eventually, the deposit must have grown onto the right-hand side via the lower blade edge. The offset to the predicted deposit location is plausible as the deposit severity was assumed to be very low (deposition risk level 1). Such deposits may still slightly be shifted as they are likely to remain rather moist. The risk model anticipated the formation of a third major deposit, even though its location deviated from the measurement results (dot-dashed white line). The fact that the simulation suggested a deposition risk on the adjacent rear blade edge may be seen as evidence for a minor deviation of the spray targeting (white arrows). This would also yield a plausible explanation for the prediction of a deposit on the upper side of the rightmost front blade, which was not related to any of the experimentally observed deposits (Fig. 6.13(e) above dashed circle). All three major deposits were associated with undesired secondary reactions (deposit formation risk level 1). In contrast, the formation of a small deposit on the second blade from the right was related to urea crystallisation (dotted white line). This was plausible as the reverse side of the corresponding blade was a primary impingement target and, therefore, subject to intense cooling. It should be mentioned that the simulation yielded an additional area with significant deposit formation risk, Fig. 6.14(e) (left above the solid white line) which could not be related to any deposit observed during the measurement. This could in turn be indicative of a minor deviation of the spray targeting, which may have shifted a fraction of the impinging spray to the adjacent blade (white arrows).

The risk model predicted further potential deposit locations, Fig. 6.13 (purple lines). However, it was not possible to verify these, as a documentation of the deposits on the rear side of the mixer was unavailable. The comparison between measurement and simulation results furthermore shows that not all minor deposits can be anticipated, e.g. on the leftmost blade. On the one hand, deposits may grow very slowly if only very little amounts of excess UWS are available locally, i.e. if single cells exhibit a deposit formation risk. On the other hand, minor temperature and mass flow fluctuations cannot completely be eliminated over several hours in a test bench environment. Under such circumstances, the local conditions may be subject to subtle changes which may trigger a delayed onset of deposit formation.

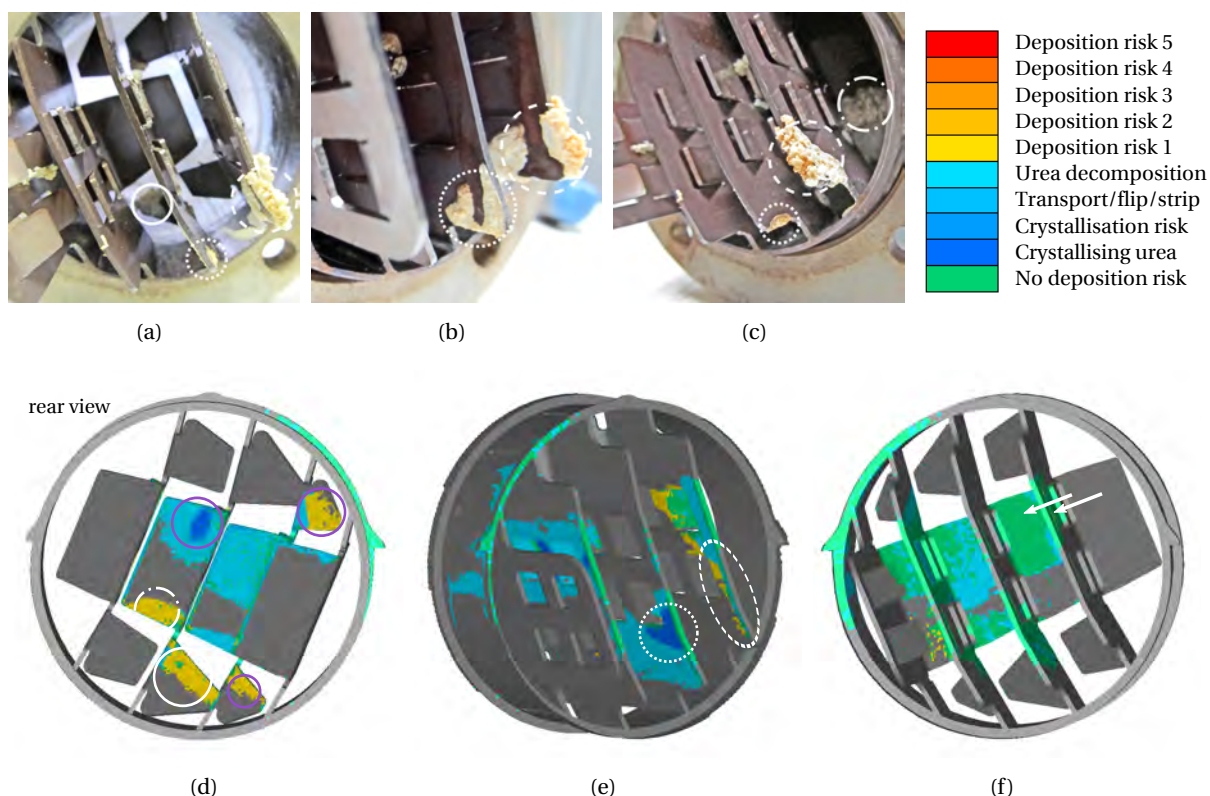


Figure 6.13: Validation of the deposit formation risk on the mixing element of the underbody type SCR system. OP 200/100/35. Upper row shows deposit formation on the mixing element after an experiment duration of 240 min. Lower row shows deposit formation risk prediction 40 s after SOI. White circles indicate major deposit locations, purple circles indicate unverified deposit nucleus locations. Arrows indicate possible deviations of the spray targeting.

In general, the prediction of the deposit formation risk model correlated very well with the measurement results. The large extent of rear blade edge wetting on the central rear blades was a precursor for excessive droplet stripping, and pointed towards the formation of deposits in the downstream piping, see Fig. 5.2(d). Large green areas on the frontal side of the mixing element signalled impingement areas and adjacent sectors with intense liquid film dynamics, which did not exhibit any deposit formation risk. In addition, widespread light blue areas showed blade faces which were wetted but featured low enough temperatures or HNCO concentrations to impede deposition.

Raising the exhaust temperature to 240 °C slightly shifted the deposit locations on the mixing element. Again, three major deposits were found during the measurement, Fig. 6.14 (solid, dashed and dot-dashed white lines). The risk model anticipated deposition on the rear blade face as well as on the left-hand side of the second blade from the right (solid white lines). The measurement confirmed the formation of a large deposit in this area. It seems it originated from two separate nuclei, which merged upon accumulation. Moreover, a deposit nucleus was predicted on the rightmost front edge (dashed white line). The position of the trickling pathways in the experiments confirmed the origin of this deposit and revealed that it spread on both sides of the corresponding blade. The formation of a third major deposit was predicted on the leftmost rear blade (dot-dashed white lines). Furthermore, a small deposit was expected to grow from the central rear blade edge of the second blade from the right (dotted white line). Both deposits were confirmed by the experimental results. The deposit formation risk model predicted further potential deposit nucleus locations, which could not be verified as

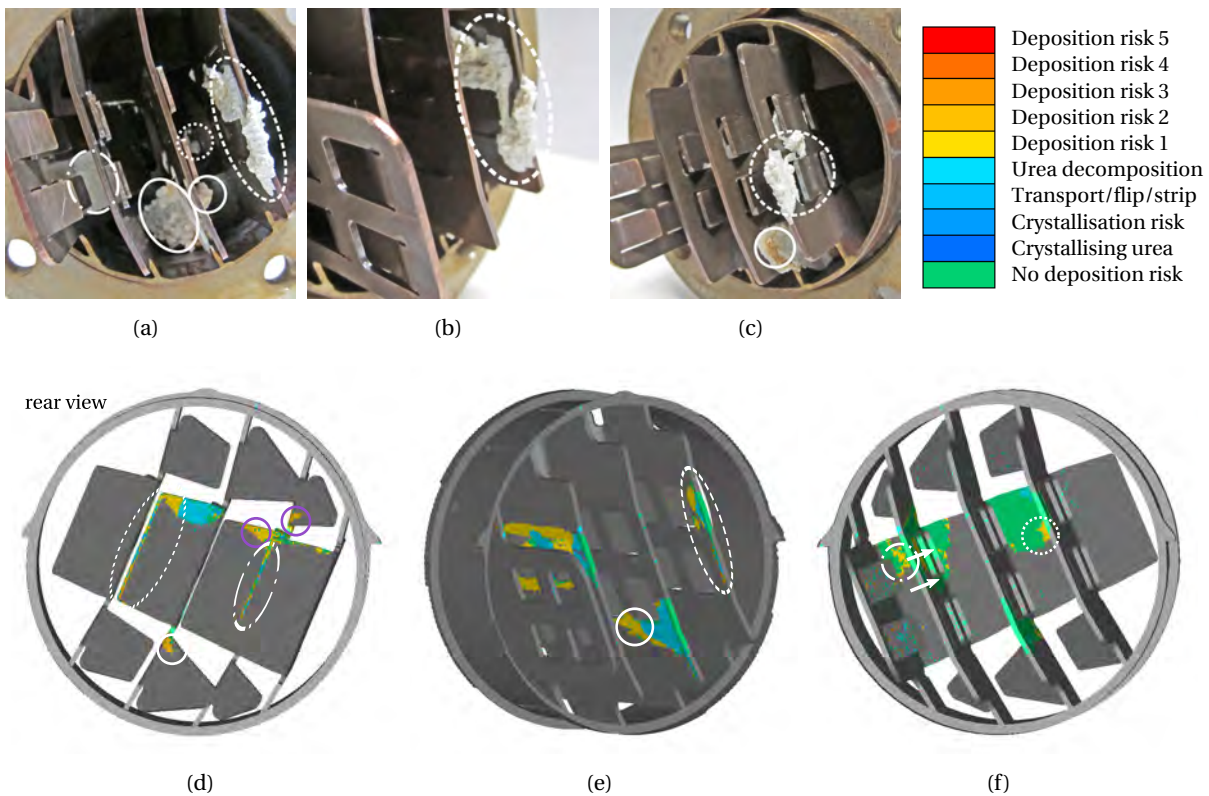


Figure 6.14: Visualisation of the deposit formation risk on the mixing element of the underbody type SCR system. OP 240/100/35. Upper row shows deposit formation on the mixing element after an experiment duration of 240 min. Lower row shows deposit formation risk prediction 40 s after SOI. White circles indicate major deposit locations, purple circles indicate unverified deposit nucleus locations. Arrows indicate possible deviations of the spray targeting.

a documentation of the deposits on the rear side of the mixer was unavailable (purple lines).

In contrast to operation at 200 °C, wall film accumulation at the rear blade edges was noticeably reduced, which lowered the risk of droplet stripping but raised the local probability of deposit formation. Generally, more UWS was prepared due to the increase in temperature. This effectively narrowed down the areas of potential deposit formation and became noticeable in smaller green and light blue sectors. The anticipated deposit severity was increased (deposition risk level 2) and UWS crystallisation was no longer possible.

In conclusion, all major deposits were predicted with good accuracy. The model successfully determines the local deposit formation risk of wetted areas, based on the relationship between liquid film dynamics, temperature and H₂CO concentration. Most importantly, the method is capable of anticipating the impact of the exhaust temperature on the fluid film pathways and properties. The analysis confirmed that blade edges are especially prone to deposit formation. Spatial discrepancies between predicted and observed deposition locations were related to minor deviations of the spray targeting, possibly triggered by deposits on the injector plate, see Fig. 5.2 (first row). This would also deliver a plausible explanation for the fact that the deviations were not systematic. In any case, the predicted deposit severity was low (deposition risk level ≤ 2), which was in line with the small overall amount of deposits on the mixer after 240 min. It also implied the formation of deposits which would easily decompose upon heating to 350 °C.

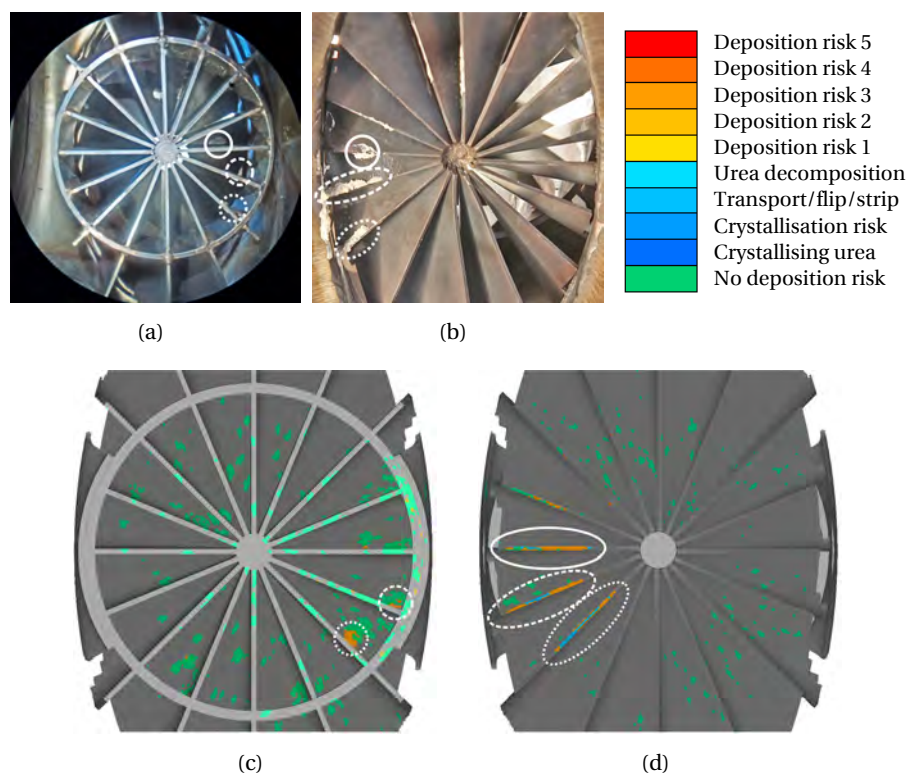


Figure 6.15: Visualisation of the deposit formation risk on the mixing element of the close-coupled type SCR system: front (a, c) and rear view (b, d). OP 275/170/60. Test case: mixer 1 and hollow-cone injector (M1 HC). Upper row shows deposit formation on the mixing element after an experiment duration of 90 min. Lower row shows deposit formation risk prediction 40 s after SOI. White circles indicate major deposit locations.

6.3.2 Injection Rate

In order to assess whether the deposit formation risk model can correctly predict the impact of the injection rate, it was tested on the close-coupled SCR system using mixer 1 and the hollow-cone injector. Two different injection rates were compared, while maintaining exhaust mass flow and temperature constant at 275 °C and 170 kg/s. An experimental duration of 90 min was sufficient to verify the deposit formation risk. Three major deposits were found during the measurements with an injection rate of 60 mg/s, Fig. 6.15. In all cases, deposit formation and accumulation started at the rear blade edges. Subsequently, the central and lower deposit (dashed and dotted lines, respectively) spread onto the outer pipe wall, whereas the upper deposit (solid line) accumulated towards the mixer front side. The deposit formation risk model accurately predicted the formation of a deposit nucleus in all three locations. The development of blue areas indicated strong liquid film accumulation, which can be interpreted as a precursor for liquid film trickling and deposition onto the outer pipe wall. Since the wall film temperature remained below 250 °C, the deposit severity was not very emphasised (deposition risk 3). This was confirmed by the small amount of deposits observed during the measurements after 90 min. The widespread distribution of green areas both on the front and rear side of the mixing element was reflective of the impingement areas and small sectors with highly dynamic wall film, both of which did not exhibit a deposition risk.

Setting the injection rate to 35 mg/s noticeably reduced the amount of deposits, Fig. 6.16. Deposit formation was observed on one single blade only. The deposit formation risk model represented this trend very well and predicted the location of the deposit with excellent accuracy.

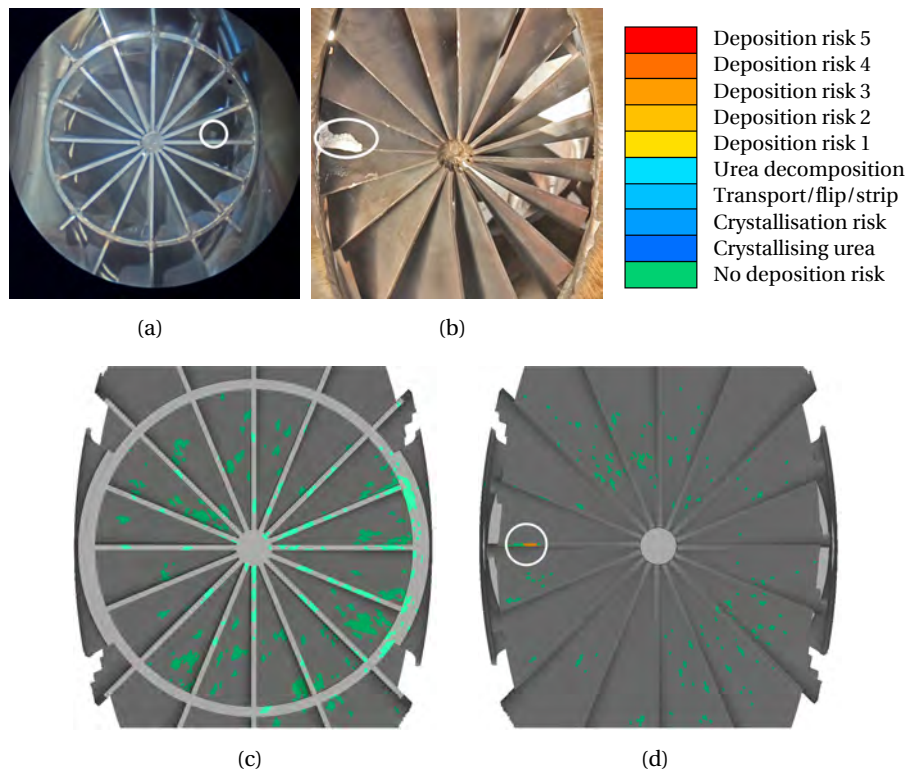


Figure 6.16: Visualisation of the deposit formation risk on the mixing element of the close-coupled type SCR system: front (a, c) and rear view (b, d). OP 275/170/35. Test case: mixer 1 and hollow-cone injector (M1 HC). Upper row shows deposit formation on the mixing element after an experiment duration of 90 min. Lower row shows deposit formation risk prediction 40 s after SOI, $0.1\rho_{s,ref}$. White circles indicate major deposit locations.

6.3.3 Mixing Element and Spray

In order to assess whether the model can correctly predict deposit formation risk trends, the validation was extended to include all possible combinations of the two mixers and injectors. Replacing the mixing element (setup with mixer 2 and the hollow cone injector, M2 HC) yielded a similar extent of deposit formation compared to the reference case M1 HC at 60 mg/s, compare Figs. 6.15(b) and 6.17(b). The individual deposits exhibited slightly stronger accumulation. However, major deposits were observed on two blades only. Based on the simulated wall film pathways, the location of either was predicted with good accuracy by the risk model. A reduction of the injection rate to 35 mg/s revealed a negligible amount of deposits for the setup with mixer 2, Fig. 6.18(b). This trend was confirmed by the model.

Replacing the injector (setup with mixer 1 and the 6-hole injector, M1 6H) resulted in a noticeable increase of deposit accumulation compared to the reference case M1 HC at 60 mg/s, Fig. 6.17(a). Major deposits were found on three blades. Out of these, the risk model predicted two with good accuracy. A reduction of the injection rate to 35 mg/s resulted in two deposits out of which one could be detected unambiguously, Fig. 6.18(a). The evidence suggests that, in case of the setup M1 6H, the overall extent of deposit formation was slightly underestimated. Despite this, major deposit locations were predicted with good accuracy.

Similar results were observed for the setup with mixer 2 and the 6-hole injector, Fig. 6.17(c). Out of two deposits one was predicted with good accuracy at 60 mg/s. However, in case of 35 mg/s, a deposit

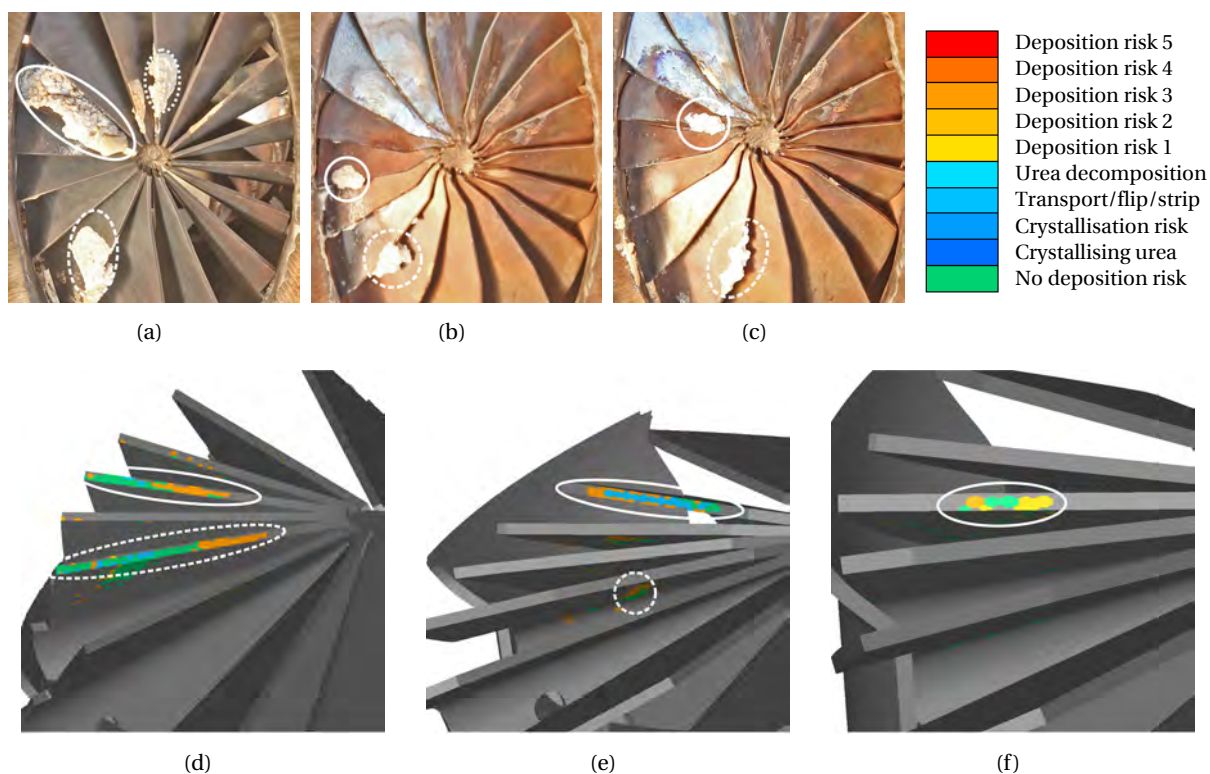


Figure 6.17: Visualisation of the deposit formation risk on the mixing element of the close-coupled type SCR system: mixer 1/6-hole injector (a, d), mixer 2/hollow-cone injector (b, e), mixer 2/6-hole injector (c, f). OP 275/170/60. Upper row shows deposit formation on the mixing element after an experiment duration of 90 min. Lower row shows deposit formation risk prediction 40 s after SOI. White circles indicate major deposit locations.

formation risk was not observed based on the simulation, although one blade was exposed to deposit formation in the measurement, Fig. 6.18(c).

An intermediate deposit severity (deposition risk 3) was observed for all investigated variants and independent of the injection rate, except for the setup M2 6H (deposition risk 2). This was due to the fact that the blade temperature dropped below 250 °C at all areas exposed to deposit formation. Furthermore, this observation was confirmed by single temperature measurements at the respective blades (results not shown) and by the fact that the overall amounts of formed deposits were still very small after 90 min. Reliable system operation was put at risk for neither of the investigated operating points, despite the fact that comparatively high injection rates were applied.

In general, the model captured the measured trends very well. Deposit formation was observed for both injectors. It was interesting to notice that the type of injector had little influence on the extent of statistical variation between the injection events within the last second of the simulated time. The extent of deposit formation increased with the injection rate in all cases. The number of blades exposed to deposit formation was lower in case mixer 2 was applied compared to the reference, mixer 1. Deposit formation was initiated at or in the direct vicinity of rear blade edges. An excellent representation of both extent and location was observed for both setups involving the hollow-cone injector. Apparently, the representation of deposit locations was slightly less accurate for setups involving the 6-hole injector, and the amount of blades exhibiting deposit formation was underestimated.

A detailed analysis of wall wetting and solid cooling was conducted to shed light on the underlying mechanisms. In contrast to mixer 1, the rear blade edges of mixer 2 were not immediately wetted due

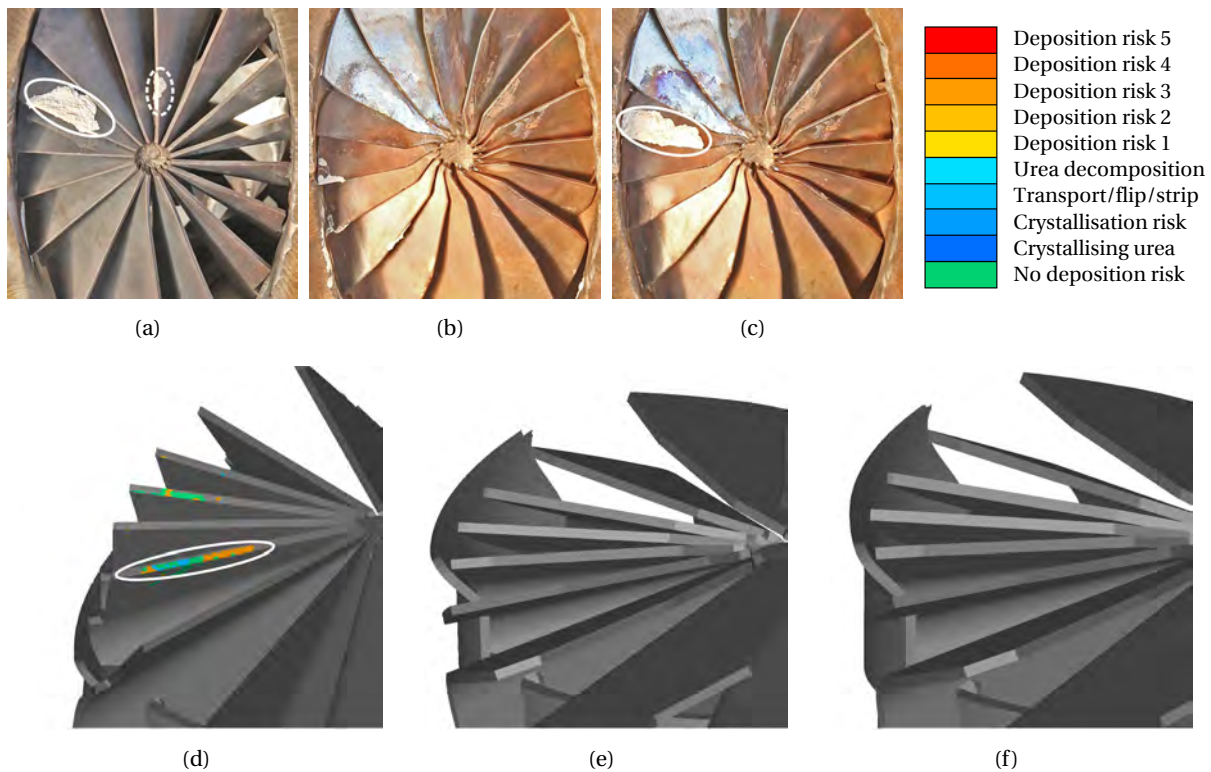


Figure 6.18: Visualisation of the deposit formation risk on the mixing element of the close-coupled type SCR system: mixer 1/6-hole injector (a, d), mixer 2/hollow-cone injector (b, e), mixer 2/6-hole injector (c, f). OP 275/170/35. Upper row shows deposit formation on the mixing element after an experiment duration of 90 min. Lower row shows deposit formation risk prediction 40 s after SOI, $0.1\rho_{s,ref}$. White circles indicate major deposit locations.

to pronounced blade overlapping. As a consequence, a larger blade surface area was used for wall film evaporation, which effectively also increased the timescales necessary for rear blade edge wetting. This phenomenon became visible also through the extent of solid cooling, Fig. 6.19. In comparison with mixer 1, the cooling of the blades was more emphasised and less focused on the rear blade edges. In combination with the hollow-cone injector, the cooling of the mixing element was spread onto a larger area. Due to the focused spray targeting, the local temperature drop was more pronounced for setups using the 6-hole injector. The results demonstrate that the UWS preparation model captures the complex interaction of system design, operating, and boundary conditions very well. Impact factors, such as the specific impingement mass flow rate, are intrinsically considered, which is the basis for the correct determination of the deposit formation risk.

The underestimation of the extent of deposit formation seemed to be systematically related to the usage of the 6-hole injector. The exact location of the injection holes as well as the droplet spectrum were defined based on measurements of the injector in order to ensure accurate simulation of wall film formation and evaporation. Further spray characteristics, such as the exact orientation and the cone angles of the individual injector beams, as well as the injection velocity were set up according to measurements provided by the manufacturer. A detailed analysis of the wall film pathways revealed that blades with a deficient prediction of the deposit formation risk were in fact exposed to intermittent wall wetting. However, the corresponding wall film pathways did not develop adequately. These observations would seem to suggest that, while the spray targeting was correct, the assumption of uniform mass flow distribution within the individual injector beam cones might not

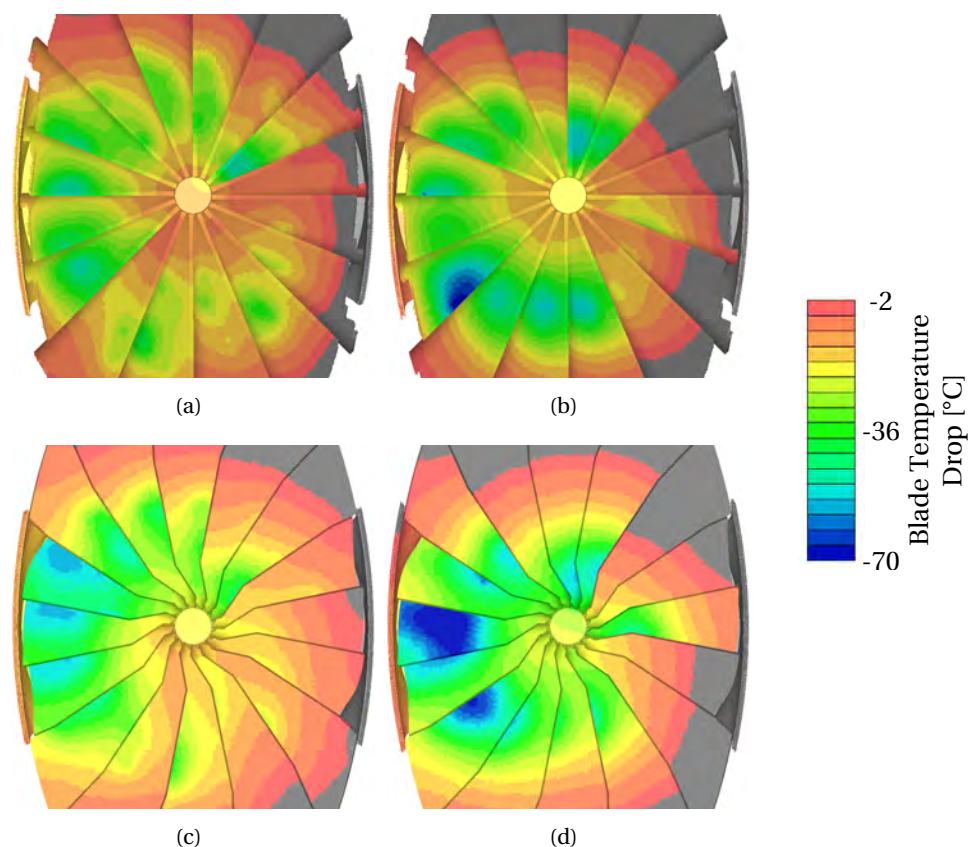


Figure 6.19: Blade cooling of the mixing element of the close-coupled type SCR system: mixer 1/hollow-cone injector (a, 39.818 s after SOI), mixer 1/6-hole injector (b, 40 s after SOI), mixer 2/hollow-cone injector (c, 39.818 s after SOI), mixer 2/6-hole injector (d, 40 s after SOI). OP 275/170/60. Temperature drop evaluated by subtracting the temperature distribution at the end of the last calculated injection event from the reference distribution at SOI.

have been perfectly accurate. In order to test the sensitivity of the results, a simulation of the setup M2 6H was conducted applying injector beam cone angles of 3.5° instead of 7° , while maintaining all other parameters constant (OP 275/170/60, results not shown). The analysis of the wall film pathways revealed permanent wall wetting of the upper rear blade edges, similar to what was observed during the measurements, Fig. 6.17(c). The evidence does not necessarily imply inaccurate measurements of the spray angles. However, it indicates that it might be necessary to model the UWS mass flow as a function of the injector beam cone angle instead of assuming a uniform distribution. A review of literature data confirmed that the largest spray density, as well as the highest local droplet SMD and velocity typically can be found at or close to the spray beam cone axes [151–154].

Chapter 7

Summary and Conclusions

The reduction of nitrogen oxides by means of urea-based SCR systems will continue to be an integral part of emission reduction strategies for both light and heavy duty diesel powered engines. Preventing the formation of deposits is a major design target in order to guarantee effectiveness and reliability of SCR systems. The present work contributes to the understanding of the deposition mechanisms and provides a methodology for the numerical prediction of the deposit formation risk.

Deposit formation may be observed in virtually any location between the point of injection and the intake of the SCR catalyst. While deposits on the injector are primarily triggered by irregular injection, e.g. injector leakage, deposit formation on system walls is closely related to impingement and wetting of the respective areas with urea water solution. Among these, the primary impingement targets exhibit the highest deposition risk. As mixing elements are typically employed as such in passenger car applications, they were the focus of the present work.

An optically accessible box was designed in order to analyse the mechanisms of deposit formation. A surrogate mixing element was installed, which imitated the geometric features of a common mixing element from a series SCR system. A systematic study of wall film evaporation revealed that at low exhaust temperatures, $T_e = 200\text{ }^\circ\text{C}$, complete UWS preparation was not possible even for injection rates as low as 3.3 mg/s. Raising the exhaust enthalpy flux, i.e. the temperature and/or the mass flow, increased the tolerable injection rate and therefore confirmed the fundamental temperature-dependency of deposit formation. In areas of initial wall wetting, continuous dilution and intense mixing of the film effectively impeded deposition independent of the temperature. However, as soon as the film left these areas, deposit formation had to be expected. Typically, wall film was extensively distributed onto all adjacent blade faces at geometric inconsistencies, such as edges, holes, or blade joints. It accumulated at rear blade edges, flipped around rear edges onto the reverse blade faces, and stripped off edges, wetting subjacent blades or downstream piping. Deposits formed independently from the local flow field on surfaces with direct incident flow, shear flow, and in wake regions. Among the variety of geometric inconsistencies, deposit formation was most frequently observed at rear blade edges. The excellent correlation between the deposition scenarios observed in the box and in the SCR systems underlined the universality of the results obtained. Once a deposit nucleus had formed, it could act as a starting point for further deposit accumulation. The analysis of deposit growth yielded two fundamental growth mechanisms. Urea solidified at the upstream border of present deposits (*damming growth*) but also on peripheral borders (*peripheral growth*). In the latter case, UWS was transported through small channels and fissures. The consecutive steps of deposit formation were wall wetting, liquid film accumulation, deposit nucleus formation, and deposit accumulation. Apart from impingement areas, deposit formation was also impeded in liquid films which trickled with high velocities and/or were particularly thick, e.g. in accumulation areas. In other words,

urea solidification was hindered wherever films were continuously put into motion and/or diluted and where undesired reaction products were continuously removed. In addition, thicker wall films implied a lower heat input and evaporation rate due to the reduction of their surface to volume ratio. The sharpening of rear blade edges neither affected the location nor the extent of deposit formation. Concludingly, the study confirmed that persisting liquid film has to be seen as a precursor for deposit formation and proved that location and growth of deposits cannot solely be explained based on the spray targeting. It was possible to plausibly explain the formation of all deposits observed in the underbody type SCR system, based on the described wall film transport and growth mechanisms.

Deposit formation was observed over a wide range of operating conditions. While the minimum temperature was related to start of injection, the maximum temperature depended on whether a stable Leidenfrost effect was maintained permanently. This corresponded to mixer temperatures between approx. 180 °C and 310 °C before the start of injection. The deposition temperature rose with the exhaust enthalpy flux slightly less than proportionally and laid within a narrow temperature band. The area of solidification was determined by the balance between the available exhaust enthalpy flux and the enthalpy required to decompose the injected UWS. Higher injection rates and lower exhaust enthalpies shifted the deposit location further downstream without altering the general liquid film pathways. The critical injection rate, above which deposition had to be expected, increased exponentially with the mixing element temperature level. Up to 290 °C, it was characterised by the transition between intermittent and permanent wall wetting. Above 300 °C, it was determined by the Leidenfrost temperature. The change of the underlying mechanisms became apparent in the increase of the growth rate around 295 °C. The solidification timescales remained above 600 s below 200 °C and below 160 s above 300 °C. In between it was typically governed by the balance between injection rate and exhaust enthalpy flux. At a given temperature, lower injection rates and higher exhaust mass flows effected lower solidification timescales. Deposits grew fast if the temperature level exceeded approx. 290 °C. Accumulation was especially severe whenever the operating conditions initially caused a Leidenfrost effect and subsequently allowed the temperature to fall below the Leidenfrost point. The combination of high injection rates and exhaust enthalpy fluxes led to very short solidification timescales and rapid accumulation.

Thermogravimetry allows an efficient qualitative assessment of deposit components if the experimental boundary conditions are held constant. Deposits formed up to a temperature of 250 °C were characterised by the degree of conversion of urea and biuret into cyanuric acid, and maintained a low and constant amount of temperature-stable components of around 8 % (*low-temperature deposits*). Deposits formed above 250 °C did not contain any urea, only traces of biuret, and were characterised by the degree of conversion of cyanuric acid intoammelide andammeline. Their amount increased with temperature, rendering them more and more temperature-stable (*high-temperature deposits*). Systematic decomposition experiments showed that low-temperature deposits required a moderate temperature increase to at least 350 °C, while high-temperature deposits needed temperatures exceeding 600 °C (DPF regeneration) to be decomposed within the single minute range. Generally, an increase of the deposit mass will prolong the required depletion timescale. It also raises the amount of temperature-stable components produced during urea decomposition. This can be critical in particular if the available time is insufficient for sample depletion as it may further increase the temperature stability of such deposits.

It was the aim of the present work to provide a methodology which allows the prediction of the deposit formation risk based on the physical properties of the wall film. Based on a validated CFD model, the evolution of the wall film pathways on the mixing element was simulated during 40 s after start of injection. In addition, a strategy was presented to significantly lower the timescale of solid cooling based on the application of similarity principles ($Fo = \text{const.}$). It was applied in case the wall film pathways on the mixing element could not be covered sufficiently within the simulated time. Based

on the experimental results, a model was derived which is capable of assessing the local deposit formation risk based on the interpretation of the combined impact of wall film pathways, different forms of wall film dynamics, and the temperature level, together with the local urea and HNCO concentration. The model was able to predict the influence of temperature, spray and mixing element geometry on the deposition risk with excellent accuracy. The formation of deposit nuclei was anticipated for all major deposits. The manipulation of the spray targeting by deposits on the injector plate and minor inaccuracies of the droplet mass distribution as a function of the individual beam cone angles were identified as plausible explanations for deviations between experimental and numerical results. In summary, the model is able to predict the deposit formation risk as a function of fundamental design features and operating conditions. The chemistry of deposit formation is considered indirectly via the wall film temperature and HNCO concentration. Great care has to be taken to model spray targeting and spray characteristics accurately. While the present work focussed on deposit formation on the mixing element, the deposit formation risk model can also be applied to all other SCR system walls.

The presented methodology exceeds the capabilities of available models which rely on the sole interpretation of wall wetting and solid cooling based on single or very few injection events. The specific impingement mass flow rate has significant impact on the efficiency of UWS preparation and, therefore, indirectly affects the deposit formation risk. However, in contrast to the previous interpretation in the literature [44, 93], a high specific impingement mass flow rate is not directly related to deposit formation. In fact, it is related to an increase of both the liquid film dynamics and the dilution of the present wall film which impede deposition locally. Despite this, a high specific impingement mass flow rate is a rough indicator for an increased risk of incomplete wall film evaporation, which would lead to deposit formation as soon as the film leaves the areas of initial wall wetting. The presented methodology can easily be implemented as an extension of state-of-the-art simulations of the ammonia homogenisation. To the present day, models which capture the deposit chemistry in detail have been limited to the simulation of reactor experiments. Unlike these models, the presented methodology is capable of predicting the deposit formation risk in realistic SCR system geometries.

The present work implies a number of design strategies for SCR systems to improve their resistance against deposit formation. Generally, the application of close-coupled type systems contributes to an increase of the exhaust temperature level as heat losses are reduced by installing the system closer to the engine. While this supports UWS evaporation, and hence lowers the deposit formation risk, it often goes along with shortened mixing sections which may exacerbate ammonia homogenisation. The investigations showed that an optimum mixer or injector concept is nonexistent. In fact, the components have to be matched and their interaction optimised in order to yield a broad distribution and reliable targeting of the UWS on the surface of the mixing element. This approach entails a low specific impingement mass flow rate and, therefore, helps to accelerate UWS preparation by maximising the local ratio between available exhaust enthalpy flux and liquid film mass. As a consequence, the local cooling is diminished. Equally, a broad spray targeting contributes to a reduction of the local HNCO concentration which effectively reduces the risk of undesired secondary reactions. The described measures effectively raise the critical injection rate which can be tolerated without the risk of deposition. On the spray side, a well defined targeting may be achieved by ensuring sufficient droplet momentum, either by selecting injectors with higher Sauter mean diameters or by realising higher injection velocities. Both strategies effectively reduce the dispersion of the spray by the flow field between the point of injection and the mixing element. In general, an increase of the surface available for impingement, wall film formation and evaporation is expected to support UWS preparation. However, in the light of the experimental results, it remains questionable whether or not adding holes or flaps to main blade elements helps to reduce the deposit formation risk. In fact, deposit formation was frequently triggered at the resulting edges as wall film accumulation lowered the evaporation rates, droplet stripping shifted the problem to downstream blades or piping, and wall film dynamics were noticeably reduced whenever wall film flipped onto the reverse blade sides. While these

aspects all increase the deposit formation risk, an extension of the surfaces exposed to wall wetting may prevent or at least delay wall film reaching critical locations and help to maintain film dynamics on a higher level. As such extensions typically involve an increase of the engine backpressure, a trade-off between pressure drop and resistance against deposit formation has to be found.

The implementation of detailed chemistry, i.e. reaction kinetics including phase changes, in combination with further reductions of the required wall times is seen as a key development target for future work. This will not only increase the prediction accuracy but also allow to capture deposit accumulation and decomposition. In a first step, this entails coupling the wall film model with a chemical reactor model. In a second step, the wall film model should be extended to account for the impact of film (or deposit) thickness on both the gas phase flow field and the wall film pathways. As deposit formation proceeds on timescales in the minute to hour range the wall time requirements of state-of-the-art simulation models will have to be further reduced. This may be achieved by pre-calculating the flow field of the entire SCR system and mapping the solution onto the boundaries of a smaller simulation domain, e.g. the mixing section or even just the mixing element itself, where UWS preparation and deposit formation proceed. Additionally, freezing the calculation of the flow field may help to reduce the wall time. A periodical recalculation would still allow to capture the impact of deposit growth. As the physical processes involved in UWS preparation proceed on different timescales (e.g. droplet dynamics, wall film dynamics, species mixing, and solid cooling), computational resources may be used more efficiently by using an automated time step adaptation which is sensitive to the instantaneous state of the system. The latter may include, for instance, the droplet mass within the system as well as the gradients of wall film mass changes and/or species concentrations.

Future efforts should also involve enhancing the accuracy of injector modelling. For one thing, capturing the droplet mass distribution as a function of the cone and/or injector beam angles would benefit the prediction accuracy of the wall film pathways. For another thing, accounting not only for the droplet diameter distribution but also for the injection velocity distribution would increase the prediction accuracy of the spray targeting, which is directly related to the actual droplet momentum. For the evaluation of the deposit formation risk it is vital to capture the onset of wall wetting. Therefore, the dependency of droplet wall heat transfer and the deposition limit on parameters, such as the specific impingement mass flow rate, injection frequency, and droplet impact Weber number, should be considered in more detail by next-generation impingement models. This will also be crucial if the transition between Leidenfrost effect and wall wetting regimes shall be captured accurately for arbitrary combinations of sprays and mixing sections. As the mixing sections of state-of-the-art SCR systems have been shortened significantly in the recent years, impingement and wetting of the catalyst substrate has become more likely. Therefore, future research will also have to pay more attention to droplet wall interaction at the catalyst. The application of a Large Eddy Simulation approach has been shown to enhance the prediction accuracy with respect to species mixing and homogenisation. However, so far a combination with the evaluation of the deposit formation risk appears to be out of reach owing to the immense consumption of computational power.

With respect to the model calibration, it is likely that the individual mechanisms, which promote or impede deposit formation, exhibit a transitory behaviour instead of being characterised by sharp thresholds. Equally, the boundaries between individual deposit severity classes are expected to be rather smooth. However, the implementation of such boundaries requires further detailed investigations of the deposit formation process under consideration of additional impact factors, such as the gas phase concentration and time. At the catalyst the boundaries as well as the mechanisms of deposit formation are likely to differ from those observed in the mixing section. This is due to the difference in structure, surface, and the availability of a catalytically active coating and also calls for separate investigations.

Bibliography

- [1] European Automobile Manufacturers Association. New passenger car registrations breakdown by share of diesel. Online resource, accessed: 02.11.2015, http://www.acea.be/uploads/statistic_documents/Diesel_penetration_in_Western_Europe.pdf, 5 2015.
- [2] J.B. Heywood. *Internal Combustion Engine Fundamentals*. McGraw-Hill, 1st edition, 1988.
- [3] J. Warnatz, U. Maas, and R.W. Dibble. *Combustion*. Springer, 4th edition, 2006.
- [4] K. Mollenhauer and H. Tschöke, editors. *Handbuch Dieselmotoren*. Springer, 3rd edition, 2007.
- [5] T. Johnson. Vehicular Emissions in Review. *SAE International Journal of Engines*, 9(2), 2016, doi:10.4271/2016-01-0919.
- [6] Th. Körfer, W. Bick, Th. Schnorbus, B. Holderbaum, M. Pieper, M. Miccio, B. Graziano, and B. Heuser. Konstruktive Umsetzung und thermodynamisches Potential eines variablen Verdichtungsverhältnisses für moderne Dieselmotoren. *Fortschritt-Berichte VDI Reihe 12, Nr. 777, 35. International Vienna Motor Symposium 8.-9. Mai 2014, Band 1: erster Tag*, pages 223–247. VDI-Verlag, 2014.
- [7] T. Fukuma, N. Oikawa, M. Takeda, S. Nakayama, K. Yoshida, and Y. Nozaki. Toyota's development strategy for diesel passenger car after-treatment technology. *Fortschritt-Berichte VDI Reihe 12, Nr. 777, 35th International Vienna Motor Symposium 8-9 May 2014, Volume 2: second day*, pages 309–331. VDI-Verlag, 2014.
- [8] I. Nova and E. Tronconi, editors. *Urea-SCR Technology for deNO_x After Treatment of Diesel Exhausts*. Springer, 1st edition, 2014.
- [9] J. Bolland, M. Parmentier, and J. Schmitt. Control of a Combined SCR on Filter and Under-Floor SCR System for Low Emission Passenger Cars. *SAE International Journal of Engines*, 7(3):1252–1261, 2014, doi:10.4271/2014-01-1522.
- [10] T. Wittka, B. Holderbaum, T. Maunula, and M. Weissner. Development and Demonstration of LNT+SCR System for Passenger Car Diesel Applications. *SAE International Journal of Engines*, 7(3):1269–1279, 2014, doi:10.4271/2014-01-1537.
- [11] F. Steinparzer, P. Nefischer, W. Stütz, D. Hiemesch, and M. Kaufmann. The New BMW Six-Cylinder Top Engine With Innovative Turbocharging Concept. *Fortschritt-Berichte VDI Reihe 12, Nr. 799, 37th International Vienna Motor Symposium, 28-29 April 2016, Volume 2: second day*, pages 138–159. VDI-Verlag, 2016.
- [12] A. Kato, S. Matsuda, T. Kamo, F. Nakajima, H. Kuroda, and T. Narita. Reaction between NO_x and NH₃ on Iron Oxide-Titanium Oxide Catalyst. *The Journal of Physical Chemistry*, 85(26):4099–4102, 1981, doi:10.1021/j150626a029.
- [13] Praxair, Inc. *Ammonia, anhydrous Safety Data Sheet P-4562*, 03 2015.

- [14] P.M. Schaber, J. Colson, S. Higgins, D. Thielen, B. Anspach, and J. Brauer. Thermal decomposition (pyrolysis) of urea in an open reaction vessel. *Thermochimica Acta*, 424:131–142, 2004, doi:10.1016/j.tca.2004.05.018.
- [15] S.D. Yim, S.J. Kim, J.H. Baik, I.S. Nam, Y.S. Mok, J.H. Lee, B.K. Cho, and S.H. Oh. Decomposition of Urea into NH_3 for the SCR Process. *Industrial & Engineering Chemistry Research*, 43:4856–4863, 2004, doi:10.1021/ie034052j.
- [16] H. Dong, S. Shuai, and J. Wang. Effect of Urea Thermal Decomposition on Diesel NO_x -SCR Aftertreatment Systems. *SAE Technical Paper 2008-01-1544*, 2008, doi:10.4271/2008-01-1544.
- [17] H.L. Fang and H.F.M. DaCosta. Urea thermolysis and NO_x reduction with and without SCR catalysts. *Applied Catalysis B: Environmental*, 46(1):17–34, 2003, doi:10.1016/S0926-3373(03)00177-2.
- [18] V. Ebrahimian, A. Nicolle, and C. Habchi. Detailed Modeling of the Evaporation and Thermal Decomposition of Urea-Water Solution in SCR Systems. *AIChE Journal*, 58(7):1998–2009, 2012, doi:10.1002/aic.12736.
- [19] M. Kleemann, M. Elsener, M. Koebel, and A. Wokaun. Hydrolysis of Isocyanic Acid on SCR Catalysts. *Industrial & Engineering Chemistry Research*, 39(11):4120–4126, 2000, doi:10.1021/ie9906161.
- [20] M. Koebel, M. Elsner, and M. Kleemann. Urea-SCR: a promising technique to reduce NO_x emissions from automotive diesel engines. *Catalysis Today*, 59:335–345, 2000, doi:10.1016/S0920-5861(00)00299-6.
- [21] M. Koebel, M. Elsener, and G. Madia. Reaction Pathways in the Selective Catalytic Reduction Process with NO and NO_2 at Low Temperatures. *Industrial & Engineering Chemistry Research*, 40(1):52–59, 2001, doi:10.1021/ie000551y.
- [22] T. Johnson. *Urea-SCR Technology for deNO_x After Treatment of Diesel Exhausts*, chapter Selective Catalytic Reduction Technology, pages 2–31. Springer, 1st edition, 2014.
- [23] G. Madia, M. Koebel, M. Elsener, and A. Wokaun. Side Reactions in the Selective Catalytic Reduction of NO_x with Various NO_2 Fractions. *Industrial & Engineering Chemistry Research*, 41(16):4008–4015, 2002, doi:10.1021/ie020054c.
- [24] M. Koebel, G. Madia, and M. Elsener. Selective catalytic reduction of NO and NO_2 at low temperatures. *Catalysis Today*, 73(3-4):239–247, 2002, doi:10.1016/S0920-5861(02)00006-8.
- [25] S. Käfer. *Trockenharnstoff-SCR-System mit Betriebsstrategie für Fahrzeuge mit Dieselmotor*. PhD thesis, Technische Universität Kaiserslautern, 2004.
- [26] Z. Skaf, T. Aliyev, L. Shead, and T. Steffen. The State of the Art in Selective Catalytic Reduction Control. *SAE Technical Paper 2014-01-1533*, 2014, doi:10.4271/2014-01-1533.
- [27] S. Calvo Zueco, J. Halbei, F. Neumann, J. Oesterle, J. Rudelt, and H. Többen. Harnstoff-SCR-Systeme im Fokus. *MTZ – Motortechnische Zeitschrift*, 68(9):714–719, 2007, doi:10.1007/BF03227433.
- [28] J.J. Oesterle, S. Calvo, B. Damson, G. Feyl, F. Neumann, and J. Rudelt. Urea Systems in Focus – New Challenges and Solutions in the Development of Car and Commercial Vehicle Exhaust Systems. *SAE Technical Paper 2008-01-1186*, 2008, doi:10.4271/2008-01-1186.
- [29] J.J. Oesterle, S. Calvo, B. Damson, F. Neumann, and J. Rudelt. SCR Technology with Focus to Stringent Emissions Legislation. *SAE Technical Paper 2008-01-2640*, 2008, doi:10.4271/2008-01-2640.

- [30] G. Zheng, A. Fila, A. Kotrba, and R. Floyd. Investigation of Urea Deposits in Urea SCR Systems for Medium and Heavy Duty Trucks. *SAE Technical Paper 2010-01-1941*, 2010, doi:10.4271/2010-01-1941.
- [31] S. Fischer, R. Bitto, T. Lauer, C. Krenn, J. Tauer, and G. Pessl. Impact of the Turbulence Model and Numerical Approach on the Prediction of the Ammonia Homogenization in an Automotive SCR System. *SAE International Journal of Engines*, 5(3):1443–1458, 2012, doi:10.4271/2012-01-1291.
- [32] S. Fischer. *Simulation of the Urea-Water-Solution Preparation and Ammonia-Homogenization with a Validated CFD-Model for the Optimization of Automotive SCR-Systems*. PhD thesis, Vienna University of Technology, 2012.
- [33] P. Way, K. Viswanathan, P. Preethi, A. Gilb, N. Zambon, and J. Blaisdell. SCR Performance Optimization Through Advancements in Aftertreatment Packaging. *SAE Technical Paper 2009-01-0633*, 2009, doi:10.4271/2009-01-0633.
- [34] V.O. Strots, S. Santhanam, B.J. Adelman, G.A. Griffin, and E.M. Derybowski. Deposit Formation in Urea-SCR Systems. *SAE International Journal of Fuels and Lubricants*, 2(2):238–289, 2009, doi:10.4271/2009-01-2780.
- [35] T. Schütte. *Ablagerungs- und Alterungsverhalten wässriger Harnstofflösung bei selektiver katalytischer Reduktion von Stickoxidemissionen*. PhD thesis, Universität Lüneburg, 2010.
- [36] J. Seo. Aftertreatment Package Design for SCR Performance Optimization. *SAE Technical Paper 2011-01-1135*, 2011, doi:10.4271/2011-01-1135.
- [37] A. Munnannur, M. Chiruta, and Z.G. Liu. Thermal and Fluid Dynamic Considerations in Aftertreatment System Design for SCR Solid Deposit Mitigation. *SAE Technical Paper 2012-01-1287*, 2012, doi:10.4271/2012-01-1287.
- [38] C.L. Weeks, D.R. Ibeling, S. Han, L. Ludwig, and P. Ayyappan. Analytical Investigation of Urea Deposits in SCR System. *SAE International Journal of Engines*, 8(3):1219–1239, 2015, doi:10.4271/2015-01-1037.
- [39] S. Eakle, S. Kroll, A. Yau, J. Gomez, and C. Henry. Investigation of Urea Derived Deposits Composition in SCR Systems and Their Potential Effect on Overall PM Emissions. *SAE Technical Paper 2016-01-0989*, 2016, doi:10.4271/2016-01-0989.
- [40] L. Xu, W. Watkins, R. Snow, G. Graham, R. McCabe, C. Lambert, and R.O. Carter III. Laboratory and Engine Study of Urea-Related Deposits in Diesel Urea-SCR After-Treatment Systems. *SAE Technical Paper 2007-01-1582*, 2007, doi:10.4271/2007-01-1582.
- [41] Å. Johansson, U. Wallin, M. Karlsson, A. Isaksson, and P. Bush. Investigation on uniformity indices used for diesel exhaust aftertreatment systems. *SAE Technical Paper 2008-01-0613*, 2008, doi:10.4271/2008-01-0613.
- [42] C.S. Sluder, J.M.E. Storey, S.A. Lewis, and L.A. Lewis. Low Temperature Urea Decomposition and SCR Performance. *SAE Technical Paper 2005-01-1858*, 2005, doi:10.4271/2005-01-1858.
- [43] M. Eichelbaum, R.J. Farrauto, and M.J. Castaldi. The impact of urea on the performance of metal exchanged zeolites for the selective catalytic reduction of NO_x Part I. Pyrolysis and hydrolysis of urea over zeolite catalysts. *Applied Catalysis B: Environmental*, 97(1-2):90–97, 2010, doi:10.1016/j.apcatb.2010.03.027.

- [44] C. Becker, T. Ohrnbergera, H. Lüders, H. Härle, F. Birkhold, and C. Jaruvatee. Integrated SCR-System for Future OHW Emission Requirements – AdBlue Mixture, Deposit and Pressure Drop. *7th Emission Control*, 23.05.2014, Dresden, Germany, 2014.
- [45] H. Smith, M. Zöchbauer, and T. Lauer. Advanced Spray Impingement Modelling for an Improved Prediction Accuracy of the Ammonia Homogenisation in SCR Systems. *SAE Technical Paper 2015-01-1054*, 2015, doi:10.4271/2015-01-1054.
- [46] J. Michelin, F. Guilbaud, A. Guil, I. Newbigging, E. Jean, M. Reichert, M. Balenovic, and Z. Shaikh. Advanced Compact SCR Mixer: BlueBox. *SAE Technical Paper 2014-01-1531*, 2014, doi:10.4271/2014-01-1531.
- [47] K.M. Haas, M. Brugger, and R. Brück. Layout and Application of ultra-compact metal catalyst based SCR systems for close coupled engine applications. *4. International MinNOx Conference*, 12.06.2010-13.06.2010, Berlin, Germany, 2012.
- [48] H.J. Neußer, J. Kahrstedt, R. Dorenkamp, and H. Jelden. The Euro 6 Engines in the modular diesel engine system of Volkswagen. *MTZ worldwide*, 74(6):4–10, 2013, doi:10.1007/s38313-013-0057-9.
- [49] R. Brück, P. Hirth, and K. Müller-Haas. Motornahe Kompaktsysteme; Die Katalysatortechnik der Zukunft für PKW und Nutzfahrzeuge. *Internationaler Motorenkongress*, 18.02.2014-19.02.2014, Baden-Baden, Germany, 2014.
- [50] Stefan Knirsch, Ulrich Weiss, Stefan Möhn, and Giovanni Pamio. New Generation of the Audi V6 TDI Engine Part 2: Thermodynamics, Application and Exhaust Cleaning. *MTZ worldwide*, 75(10):22–27, 2014, doi:10.1007/s38313-014-0231-8.
- [51] G. Zheng, F. Wang, S. Zhang, J. Zhang, J. Tao, Z. Zhao, and J. Fan. Development of Compact SCR Systems with Closely Coupled Injector Configurations. *SAE Technical Paper 2014-01-1546*, 2014, doi:10.4271/2014-01-1546.
- [52] T. Heiduk, U. Weiß, A. Fröhlich, J. Helbig, S. Zülich, and S. Lorenz. The new Audi V8 TDI engine. *Fortschritt-Berichte VDI Reihe 12, Nr. 799, 37th International Vienna Motor Symposium*, 28-29 April 2016, Volume 2: second day, pages 160–192. VDI-Verlag, 2016.
- [53] H. Smith, M. Mayer, S. Pierson, and T. Lauer. Optical and Numerical Investigations on the Mechanisms of Deposit Formation in SCR Systems. *SAE International Journal of Fuels and Lubricants*, 7(2):525–542, 2014, doi:10.4271/2014-01-1563.
- [54] D.M. Geske. Mixing It Up For SCR. *Diesel Progress North American Edition*, 6 2007.
- [55] S. Schiller, M. Brandl, B. Hoppenstedt, and K. De Rudder. Wire Mesh Mixer Optimization for DEF Deposit Prevention. *SAE Technical Paper 2015-01-0989*, 2015, doi:10.4271/2015-01-0989.
- [56] R. Brück, T. Cartus, K. Müller-Haas, A. Schatz, N. Zaldua Moreno, and M. Karibayev. "NO_x-free Exhaust Gas" – AdBlue Dosing is the Key. *Fortschritt-Berichte VDI Reihe 12, Nr. 783, 36th International Vienna Motor Symposium*, 7-8 May 2015, Volume 1: first day, pages 266–289. VDI-Verlag, 2015.
- [57] G. Stiesch. *Modeling Engine Spray and Combustion Processes*. Springer, 1st edition, 2003.
- [58] M. Ciofalo, A. Caronia, M. Di Liberto, and S. Puelo. The Nukiyama curve in water spray cooling: Its derivation from temperature-time histories and its dependence on the quantities that characterize drop impact. *International Journal of Heat and Mass Transfer*, 50(25-26):4948–4966, 2007, doi:10.1016/j.ijheatmasstransfer.2007.09.022.

- [59] A. Spiteri, P.D. Eggenschwiler, Y. Liao, G. Wigley, K.A. Michalow-Mauke, M. Elsener, O. Kröcher, and K. Boulouchos. Comparative analysis on the performance of pressure and air-assisted urea injection for selective catalytic reduction of NO_x. *Fuel*, 161:269–277, 2015, doi:10.1016/j.fuel.2015.08.061.
- [60] N. van Vuuren and H. Sayar. High Speed Video Measurements of a Heated Tip Urea Injector Spray. *SAE Technical Paper 2012-01-1747*, 2012, doi:10.4271/2012-01-1747.
- [61] R. Bitto. *Herausforderungen und Lösungsansätze bei der Gestaltung von Diesellabgasanlagen zur Selektiven Katalytischen Reduktion*. PhD thesis, Technische Universität Wien, 2014.
- [62] M. Lecompte, S. Raux, and A. Frobert. Experimental Characterization of SCR DeNO_x Systems: Visualization of Urea-Water-Solution and Exhaust Gas Mixture. *SAE Technical Paper 2014-01-1524*, 2014, doi:10.4271/2014-01-1524.
- [63] X. Tian, Y. Xiao, P. Zhou, and W. Zhang. Optimization of the location of injector in urea-selective catalytic reduction system. *Journal of Marine Science and Technology*, 20(2):238–248, 2015, doi:10.1007/s00773-014-0267-0.
- [64] A.G. Koryakin, V.A. Gal’perin, A.N. Sarbaev, and A.I. Finkel’shtein. Thermography of urea and its pyrolysis products. *Zhurnal Prikladnoi Khimii*, 7(5):989–994, 1971.
- [65] L. Stradella and M. Argentero. A study of the thermal decomposition of urea, of related compounds and thiourea using DSC and TG-EGA. *Thermochimica Acta*, 219:315–323, 1993, doi:10.1016/0040-6031(93)80508-8.
- [66] J.P. Chen and K. Isa. Thermal Decomposition of Urea and Urea Derivatives by Simultaneous TG/(DTA)/MS. *Journal of the Mass Spectrometry Society of Japan*, 46(4):299–303, 1998, doi:10.5702/massspec.46.299.
- [67] P.M. Schaber, J. Colson, S. Higgins, D. Thielen, B. Anspach, and J. Brauer. Study of the urea thermal decomposition (pyrolysis) reaction and importance to cyanuric acid production. *American Laboratory*, 31(16):13–21, 1999.
- [68] A.M. Bernhard, D. Peitz, M. Elsener, Al Wokaun, and O. Kröcher. Hydrolysis and thermolysis of urea and its decomposition byproducts biuret, cyanuric acid and melamine over anatase TiO₂. *Applied Catalysis B: Environmental*, 115-116:129–137, 2012, doi:10.1016/j.apcatb.2011.12.013.
- [69] J.H. Meessen. Urea. *Ullmann’s Encyclopedia of Industrial Chemistry*, 2010, doi:10.1002/14356007.a27_333.pub2.
- [70] W. Brack, B. Heine, F. Birkhold, M. Kruse, G. Schoch, S. Tischer, and O. Deutschmann. Kinetic modeling of urea decomposition based on systematic thermogravimetric analyses of urea and its most important by-products. *Chemical Engineering Science*, 106:1 – 8, 2014, doi:10.1016/j.ces.2013.11.013.
- [71] D. Kunz. *Abgasanalytik bei Dieselmotoren mit Anlagen zur selektive katalytische Reduktion (SCR) von Stickoxiden*. PhD thesis, Universität Kaiserslautern, 1996.
- [72] O. Carp. Considerations on the thermal decomposition of urea. *Revue Romaine de Chimie*, 46(7):735–740, 2001.
- [73] G. Piazzesi, D. Nicosia, M. Devadas, O. Kröcher, M. Elsener, and A. Wokaun. Investigation of HNCO adsorption and hydrolysis on Fe-ZSM5. *Catalysis Letters*, 115(1-2):33–39, 2007, doi:10.1007/s10562-007-9072-2.

- [74] I. Czekaj, O. Kröcher, and G. Piazzesi. DFT calculations, DRIFT spectroscopy and kinetic studies on the hydrolysis of isocyanic acid on the TiO₂-anatase (1 0 1) surface. *Journal of Molecular Catalysis A: Chemical*, 280(1-2):68–80, 2008, doi:10.1016/j.molcata.2007.10.027.
- [75] A. Herr. *Thermische Zersetzung von Festharnstoff für mobile SCR-Katalysatoranwendungen*. PhD thesis, Technische Universität Kaiserslautern, 2004.
- [76] M. Koebel and M. Elsener. Determination of urea and its thermal decomposition products by high-performance liquid chromatography. *Journal of Chromatography A*, 689:164–169, 1995, doi:10.1016/0021-9673(94)00922-V.
- [77] S. Sebelius, T.T. Le, L.J. Pettersson, and H. Lind. Identification of urea Decomposition from an SCR perspective; A combination of experimental work and molecular modeling. *Chemical Engineering Journal*, 231:220–226, 2013, doi:10.1016/j.cej.2013.06.124.
- [78] G. Ostrogovich and R. Bacaloglu. Die Kinetik der Thermolyse von Harnstoff und der darauffolgenden Umwandlungen. II. *Revue Roumaine de Chimie*, 10:1111–1128, 1965.
- [79] W. Kern, H. Paul, and W. Mehren. Über die Polymerisation der Cyansäure und die Struktur des Cyamelids. *Die Makromolekulare Chemie*, 14(1):146–155, 1954, doi:10.1002/macp.1954.020140111.
- [80] E. Lienhard. *Beitrag zur Kenntnis der thermischen Zersetzung von Harnstoff*. PhD thesis, Eidgenössische Technische Hochschule Zürich, 1954.
- [81] R.I. Spasskaya. Preparation of triuret from urea. *Zhurnal Prikladnoi Khimii*, 42, 1969.
- [82] B.V. Lotsch and W. Schnick. New Light on an Old Story: Formation of Melam during Thermal Condensation of Melamine. *Chemistry – A European Journal*, 13(17):4956–4968, 2007, doi:10.1002/chem.200601291.
- [83] L. Costa and G. Camino. Thermal Behaviour of Melamine. *Journal of Thermal Analysis*, 34(2):423–429, 1988, doi:10.1007/BF01913181.
- [84] B. Jürgens, E. Irran, J. Senker, P. Kroll, H. Müller, and W. Schnick. Melem (2,5,8-Triamino-tri-s-triazine), an Important Intermediate during Condensation of Melamine Rings to Graphitic Carbon Nitride: Synthesis, Structure Determination by X-ray Powder Diffractometry, Solid-State NMR, and Theoretical Studies. *Journal of the American Chemical Society*, 125(34):10288–10300, 2003, doi:10.1021/ja0357689.
- [85] E. Wirnhier, M.B. Mesch, J. Senker, and W. Schnick. Formation and Characterization of Melam, Melam Hydrate, and a Melam-Melem Adduct. *Chemistry – A European Journal*, 19(6):2041–2049, 2013, doi:10.1002/chem.201203340.
- [86] N.E. Braml. *Investigation on Precursors and Polymerization Processes of Carbon Nitrides*. PhD thesis, Ludwig-Maximilians-Universität München, 2015.
- [87] C. Hoffendahl, S. Duquesne, G. Fontaine, and S. Bourbigot. Decomposition mechanism of melamine borate in pyrolytic and thermo-oxidative conditions. *Thermochimica Acta*, 590:73–83, 2014, doi:10.1016/j.tca.2014.06.016.
- [88] G. Canosa, P.V. Alfieri, and C.A. Giudice. Hybrid Intumescent Coatings for Wood Protection against Fire Action. *Industrial & Engineering Chemistry Research*, 50(21):11897–11905, 2011, doi:10.1021/ie200015k.
- [89] X. Mei, Y. Cheng, Y. Li, X. Zhu, S. Yan, and X. Li. Thermal decomposition properties of guanidine nitrate and basic cupric nitrate. *Journal of thermal analysis and calorimetry*, 114(1):131–135, 2013, doi:10.1007/s10973-012-2851-z.

- [90] B.V. Lotsch, M. Döblinger, J. Sehnert, L. Seyfarth, J. Senker, O. Oeckler, and W. Schnick. Unmasking Melon by a Complementary Approach Employing Electron Diffraction, Solid-State NMR Spectroscopy, and Theoretical Calculations - Structural Characterization of a Carbon Nitride Polymer. *Chemistry – A European Journal*, 13(17):4969–4980, 2007, doi:10.1002/chem.200601759.
- [91] J.M. Jones and A.N. Rollinson. Thermogravimetric evolved gas analysis of urea and urea solutions with nickel alumina catalyst. *Thermochimica Acta*, 565:39–45, 2013, doi:10.1016/j.tca.2013.04.034.
- [92] A. Lundström, B. Andersson, and L. Olsson. Urea thermolysis studied under flow reactor conditions using DSC and FT-IR. *Chemical Engineering Journal*, 150(2-3):544 – 550, 2009, doi:10.1016/j.cej.2009.03.044.
- [93] A. Nishioka, Y. Sukegawa, K. Katogi, H. Mamada, T. Kowatari, T. Mukai, and H. Yokota. A Study of a New Aftertreatment System (2): Control of Urea Solution Spray for Urea-SCR. *SAE Technical Paper 2006-01-0644*, 2006, doi:10.4271/2006-01-0644.
- [94] A. Schmitt. *Beitrag zur NO_x Emissionsminderung für Niedrig-Emissions-Fahrzeuganwendungen mittels Selektiver-Katalytischer-Reduktion*. PhD thesis, Technische Universität Darmstadt, 2013.
- [95] J.H. Kwak, R.G. Tonkyn, D.H. Kim, J. Szanyi, and C.H.F. Peden. Excellent activity and selectivity of Cu-SSZ-13 in the selective catalytic reduction of NO_x with NH₃. *Journal of Catalysis*, 275(2):187–190, 2010, doi:10.1016/j.jcat.2010.07.031.
- [96] D.W. Fickel, E. D’Addio, J.A. Lauterbach, and R.F. Lobo. The ammonia Selective catalytic reduction activity of copper-exchanged small-pore zeolites. *Applied Catalysis B: Environmental*, 102(3):441–448, 2011, doi:10.1016/j.apcatb.2010.12.022.
- [97] K. Leisner, O. Mihai, K. Wijayanti, A. Kumar, K. Kamasamudram, N.W. Currier, A. Yezerets, and L. Olsson. Comparison of Cu/BEA, Cu/SSZ-13 and Cu/SAPO-34 for ammonia-SCR reactions. *Catalysis Today*, 258:49–55, 2015, doi:10.1016/j.cattod.2015.04.004.
- [98] E. Alano, E. Jean, Y. Perrot, J.P. Brunel, N. Ferrand, J. Ferhan, and K. Pajot. Compact SCR for Passenger Cars. *SAE Technical Paper 2011-01-1318*, 2011, doi:10.4271/2011-01-1318.
- [99] C. Bai and A.D. Gosman. Development of Methodology for Spray Impingement Simulation. *SAE Technical Paper 950283*, 1995, doi:10.4271/950283.
- [100] C.X. Bai, H. Rusche, and A.D. Gosman. Modelling of Gasoline Spray Impingement. *Atomization and Sprays*, 12(1-3):1–27, 2002, doi:10.1615/AtomizSpr.v12.i123.10.
- [101] F. Birkhold. *Selektive katalytische Reduktion von Stickoxiden in Kraftfahrzeugen: Untersuchung der Einspritzung von Harnstoffwasserlösung*. PhD thesis, Universität Karlsruhe, 2007.
- [102] F. Birkhold, U. Meingast, P. Wassermann, and O. Deutschmann. Analysis of the Injection of Urea-water-solution for automotive SCR DeNO_x-Systems: Modeling of the Two-phase Flow and Spray/Wall-Interaction. *SAE Technical Paper 2006-01-0643*, 2006, doi:10.4271/2006-01-0643.
- [103] L. Bolle and J.C. Moureau. Experimental Study of Heat Transfer by Spray Cooling. In D.B. Spalding and N.H. Afgan, editors, *Heat and Mass Transfer in Metallurgical Systems*, pages 527–534. Hemisphere Publishing Corporation, 1981.

- [104] J. Schmidt and H. Boye. Influence of Velocity and Size of the Droplet on the Heat Transfer in Spray Cooling. *Chemical Engineering & Technology*, 24(3):255–260, 2001, doi:10.1002/1521-4125(200103)24:3<255::AID-CEAT255>3.0.CO;2-8.
- [105] D. Czechowski. *Modell zur Bestimmung der Leidenfrosttemperatur bei der Sprühkühlung von Schmiedewerkzeugen*. Promotionsvortrag, Universität Hannover, 2006.
- [106] S. Fest-Santini. *Wärmeübergang bei der Sprühkühlung mit intermittierenden Sprays oberhalb der Leidenfrosttemperatur*. PhD thesis, Universität Magdeburg, 2009.
- [107] R.J. Issa. *Numerical Modeling of the Dynamics and Heat Transfer of Impacting Sprays for a Wide Range of Pressures*. PhD thesis, University of Pittsburgh, 2003.
- [108] P. Dunand, G. Castanet, M. Gradeck, D. Maillet, and F. Lemoine. Energy balance of droplet impinging onto a wall heated above the Leidenfrost temperature. *International Journal of Heat and Fluid Flow*, 44:170–180, 2013, doi:10.1016/j.ijheatfluidflow.2013.05.021.
- [109] J.D. Bernardin and I. Mudawar. The Leidenfrost Point: Experimental Study and Assessment of Existing Models. *Journal of Heat Transfer*, 121(4):894–903, 1999, doi:10.1115/1.2826080.
- [110] F.W. Jr. Miller and H.R. Dittmar. The Solubility of Urea in Water. The Heat of Fusion of Urea. *Journal of the American Chemical Society*, 56(4):848–849, 1934, doi:10.1021/ja01319a023.
- [111] BASF Aktiengesellschaft Geschäftseinheit Leime und Tränklarze. *Technisches Merkblatt M 6221 d AdBlue*, 11 2006.
- [112] Terra Industries Inc. *Urea & Urea Solution Storage, Handling and Dilution*, 12 2006.
- [113] S. Kontin, A. Höfler, R. Koch, and H.J. Bauer. Heat and Mass Transfer accompanied by Crystallisation of single Particles containing Urea-water-solution. *ILASS Europe 2010, 23rd Annual Conference on Liquid Atomization and Spray Systems, 06.09.2010-08.09.2010, Brno, Czech Republic*, 2010.
- [114] M. Chauvy, O. Davodet, J. Houstin, and J.B. Ramolet. SCR Modeling: How To Characterize Urea Deposit In Exhaust Line. *AST User Conference, 28.06.2011-30.06.2011, Graz, Austria*, 2011.
- [115] C. Rudek. Untersuchung der Ablagerungsbildung durch AdBlue-Eindüsung zur No_x-Reduktion im SCR-Katalysator mittels Versuch und CFD Simulation. *ANSYS Conference and 32. CADFEM Users' Meeting, 29.04.2015-30.04.2015, Wien, Austria*, 2014.
- [116] A. Jäger. Development of SCR-System by a combination of thermodynamic test benches, simulation and model gas test bench. *FEV Conference Diesel Powertrains 3.0, 28.10.2014-29.10.2014, Montabaur, Germany*, 2014.
- [117] J. Bohbot, N. Gillet, and A. Benkenida. IFP-C3D: an Unstructured Parallel Solver for Reactive Compressible Gas Flow with Spray. *Oil & Gas Science and Technology – Revue d'IFP Energies nouvelles*, 64(3):309–335, 2009, doi:10.2516/ogst/2009016.
- [118] O. Deutschmann, S. Tischer, C. Correa, D. Chatterjee, S. Kleditzsch, V.M. Janardhanan, N. Mladenov, H.D. Minh, H. Karadeniz, and M. Hettel. *DETCHEM Software package*. Karlsruhe, 2.5th edition, 2014.
- [119] H. Smith, V. Schimik, K. Gabel, and T. Lauer. Evaluation and Prediction of Deposit Severity in SCR Systems. *SAE International Journal of Engines*, 9(3), 2016, doi:10.4271/2016-01-0970.
- [120] M. Zöchbauer, S. Fischer, T. Lauer, T. Siegmann-Hegerfeld, and M. Harasek. Validation of Turbulence Models for an Automotive SCR System with Laser Doppler Anemometry Measurements. *SAE Technical Paper 2013-01-1579*, 2013, doi:10.4271/2013-01-1579.

- [121] SCHOTT Technical Glass Solutions GmbH. *SCHOTT BOROFLOAT® 33*, 05 2009.
- [122] Würth. *Technisches Datenblatt Super RTV-Silikon*, 09 2012.
- [123] Sartorius AG. *Sartorius LA Reference*, 06 2007.
- [124] L. Möltner. *Theoretische und experimentelle Untersuchungen zur Ammoniakaufbereitung aus AdBlue® unter besonderer Berücksichtigung der Tropfen/Abgas- und Tropfen/Wandinteraktion*. PhD thesis, Technische Universität Wien, 2014.
- [125] CD-adapco. *Methodology STAR-CD VERSION 4.16*, 2011.
- [126] S. Bhattacharjee, D.C. Haworth, and R. Moores. CFD Modeling of Process Upstream of the Catalyst for Urea SCR NO_x Reduction Systems in Heavy-Duty Diesel Applications. *SAE Technical Paper 2011-01-1322*, 2011, doi:10.4271/2011-01-1322.
- [127] VDI-Gesellschaft Verfahrenstechnik und Chemieingenieurwesen, editor. *VDI-Wärmeatlas*. Springer, 10th edition, 2006.
- [128] M. Zöchbauer, H. Smith, and T. Lauer. Advanced SCR Flow Modeling with a Validated Large Eddy Simulation. *SAE Technical Paper 2015-01-1046*, 2015, doi:10.4271/2015-01-1046.
- [129] M. Zöchbauer. *Prediction of the Ammonia Homogenization in Automotive SCR Systems with Large Eddy Simulation*. PhD thesis, Vienna University of Technology, 2016.
- [130] S. El Tahry. Application of a Reynolds Stress Model to Engine-Like Flow Calculations. *Journal of Fluids Engineering*, 107(4):444–450, 1985, doi:10.1115/1.3242508.
- [131] J.H. Ferziger and M. Perić. *Computational Methods for Fluid Dynamics*. Springer, 3rd edition, 2002.
- [132] S.B. Pope. *Turbulent Flows*. Cambridge University Press, 1st edition, 2000.
- [133] CD-adapco. *USER GUIDE STAR-CCM+ Version 9.02*, 2014.
- [134] H. Ström, A. Lundström, and B. Andersson. Choice of urea-spray models in CFD simulations of urea-SCR systems. *Chemical Engineering Journal*, 150:69–82, 2009, doi:10.1016/j.cej.2008.12.003.
- [135] S. Das, K. Das, Z. Abidin, and D. Mehta. Effects of Various Model Parameters in the Simulation of a Diesel SCR System. *SAE Technical Paper 2012-01-1297*, 2012, doi:10.4271/2012-01-1297.
- [136] J.W. Kiedaisch and S.P. Gravante. Calibration of CFD Spray Model Parameters Using Detailed Experimental Spray Characterization Data. *ICLASS 2009, 11th Triennial International Annual Conference on Liquid Atomization and Spray Systems, 26.07.2009-30.07.2009, Vail, Colorado USA*, 2009.
- [137] A. Spiteri and P. Dimopoulos Eggenschwiler. Experimental Fluid Dynamic Investigation of Urea-Water Sprays for Diesel Selective Catalytic Reduction-DeNO_x Applications. *Industrial & Engineering Chemistry Research*, 53(8):3047–3055, 2014, doi:10.1021/ie404037h.
- [138] E. Abu-Ramadan, K. Saha, and X. Li. Modeling the Depleting Mechanism of Urea-Water-Solution Droplet for Automotive Selective Catalytic Reduction System. *American Institute of Chemical Engineers Journal*, 57(11):3210–3225, 2011, doi:10.1002/aic.12523.
- [139] A. Lundström, T. Snelling, P. Morsing, and P. Gabrielsson. Urea decomposition and HNCO hydrolysis studied over titanium dioxide, Fe-Beta and γ -Alumina. *Applied Catalysis B: Environmental*, 106:273–279, 2011, doi:10.1016/j.apcatb.2011.05.010.

- [140] D.W. Stanton and C.J. Rutland. Multi-dimensional modeling of thin liquid films and spray-wall interactions resulting from impinging sprays. *International Journal of Heat and Mass Transfer*, 41:3037–3054, 1998, doi:10.1016/S0017-9310(98)00054-4.
- [141] D. Kuhnke. *Spray/Wall-Interaction Modelling by Dimensionless Data Analysis*. PhD thesis, Darmstadt University of Technology, 2004.
- [142] S. Musa, S. Masahiro, T. Furuhashi, and M. Arai. Evaporation characteristics of a single aqueous urea solution droplet. *Paper-ID ICLASS06-195, ICLASS-2006 Conference, 27.08.2006-01.09.2006, Kyoto, Japan*, 2006.
- [143] L. Constantino, G. D’Errico, O. Ortona, and V. Vitagliano. Transport Properties of Urea and Alkylureas Aqueous Solutions. A Velocity Correlation Study. *Journal of Molecular Liquids*, 84(2):179–191, 2000, doi:10.1016/S0167-7322(99)00180-4.
- [144] S. Nukiyama. The maximum and minimum values of the heat Q transmitted from metal to boiling water under atmospheric pressure. *Journal of the Japan Society of Mechanical Engineers*, 37:367–374, 1934, doi:10.1016/0017-9310(66)90138-4. Translated from Japanese into English in *International Journal of Heat and Mass Transfer*, 9(12):1419–1433, 1966.
- [145] G. Nellis and S. Klein. *Heat Transfer*. Cambridge University Press, 1st edition, 2009.
- [146] P. Talukdar. Boiling and Condensation. Online resource, accessed: 06.02.2016, [http://web.iitd.ac.in/~prabal/MEL242/\(25\)-boiling-1.pdf](http://web.iitd.ac.in/~prabal/MEL242/(25)-boiling-1.pdf), 10 2012.
- [147] I.L. Piro, W. Rohsenow, and S.S. Doerffer. Nucleate pool-boiling heat transfer. II: assessment of prediction methods. *International Journal of Heat and Mass Transfer*, 47(23):5045–5057, 2004, doi:10.1016/j.ijheatmasstransfer.2004.06.020.
- [148] F.M. White. *Heat and Mass Transfer*. Addison Wesley, 1st edition, 1988.
- [149] L. Krämer, G. Buschmann, L. Stiegler, F. Bunar, S. Richardson, and K.F. Hansen. Mit der Diesel-Abgasnachbehandlung auf dem Weg zum "Super-Ultra-Niedrig-Emissionsfahrzeug (SULEV)". *Fortschritt-Berichte VDI Reihe 12, Nr. 764, 34. Internationales Wiener Motorensymposium 25.-26. April 2013, Band 2: zweiter Tag*, pages 172–192. VDI-Verlag, 2013.
- [150] P. Stephan, K. Schaber, K. Stephan, and F. Mayinger. *Thermodynamik, Grundlagen und technische Anwendungen Band 1: Einstoffsysteme*. Springer, 19th edition, 2013.
- [151] F. Puschmann. *Experimentelle Untersuchung der Spraykühlung zur Qualitätsverbesserung durch definierte Einstellung des Wärmeübergangs*. PhD thesis, Universität Magdeburg, 2003.
- [152] F. Puschmann and E. Specht. Transient measurement of heat transfer in metal quenching with atomized sprays. *Experimental Thermal and Fluid Science*, 28(6):607–615, 2004, doi:10.1016/j.expthermflusci.2003.09.004.
- [153] J. Oh and K. Lee. Spray characteristics of a urea solution injector and optimal mixer location to improve droplet uniformity and NO_x conversion efficiency for selective catalytic reduction. *Fuel*, 119:90–97, 2014, doi:10.1016/j.fuel.2013.11.032.
- [154] R. Lockett, M. Jeshani, K. Makri, and R. Price. An Optical Characterization of Atomization in Non-Evaporating Diesel Sprays. *SAE Technical Paper 2016-01-0865*, 2016, doi:10.4271/2016-01-0865.

Nomenclature

Mathematical Symbols

Arabic Letters

A	–	splash boundary coefficient (dry wall)
A_w	–	splash boundary coefficient (wetted wall)
A_{imp}	m^2	impingement area
Bi	–	Biot number
C	–	proportionality constant
c	m/s	velocity
c_e	m/s	exhaust velocity
c_{max}	–	critical heat flux multiplier
c_{min}	–	Leidenfrost heat flux multiplier
c_n	m/s	impact velocity component normal to the wall
$c_{p,f}, c_{p,s}$	$J/kg \cdot K$	specific heat capacity of the fluid/solid phase
c_s	–	critical heat flux range multiplier
c_{sf}	–	Rohsenow surface coefficient
$c_{t,c}$	mm/s	wall film trickling velocity threshold
d_d	μm	droplet diameter
D_l	m^2/s	binary diffusion coefficient (liquid phase)
$d_{n,c}$	μm	numerical wall film thickness threshold
d_s	μm	stable droplet diameter
$d_{s,c}$	μm	accumulated wall film thickness threshold
$d_{t,c}$	μm	thick wall film thickness threshold
dg	–	deposit growth number
dr	–	deposition ratio
ds	–	deposit severity
fd_c	mm/mm	high liquid film dynamics threshold
$ Fo$	–	Fourier number
k	m^2/s^2	turbulent kinetic energy
K	$kg/m^3 \cdot s$	porous resistance tensor
l_f, l_s	m	characteristic length of the fluid/solid phase
La_d	–	droplet Laplace number
m_d	mg	deposit mass
\dot{m}_e	kg/h	exhaust mass flow
m_{imp}	kg	impinging droplet mass
$\dot{m}_{imp,s}$	$kg/m^2 \cdot s$	specific impingement mass flow rate
\dot{m}_{UWS}	mg/s	UWS injection rate

n	–	Rohsenow exponent
n_{evap}	–	number of parcels evaporating upon impact
n_{imp}	–	overall number of impinging parcels
n_{LF}	–	number of impinging parcels experiencing the Leidenfrost effect
Nu	–	Nußelt number
pe	–	partial evaporation ratio
Pr	–	Prandtl number
r_s	μm	surface roughness
Re	–	Reynolds number
t_{UWS}	ms	UWS injection pulse duration
S	–	slip factor
Sc_t	–	turbulent Schmidt number
t	s	time
$T_{1,\text{min}}$	$^{\circ}\text{C}$	lower temperature threshold $ds = \text{I}$
$T_{2,\text{min}}$	$^{\circ}\text{C}$	lower temperature threshold $ds = \text{II}$
$T_{3,\text{min}}$	$^{\circ}\text{C}$	lower temperature threshold $ds = \text{III}$
$T_{4,\text{min}}$	$^{\circ}\text{C}$	lower temperature threshold $ds = \text{IV}$
$T_{5,\text{min}}$	$^{\circ}\text{C}$	lower temperature threshold $ds = \text{V}$
T_a	$^{\circ}\text{C}$	ambient temperature
T_{dcmp}	$^{\circ}\text{C}$	decomposition temperature
$T_{\text{DL,u}}$	$^{\circ}\text{C}$	upper deposition limit temperature
$T_{\text{DL,l}}$	$^{\circ}\text{C}$	lower deposition limit temperature
T_e	$^{\circ}\text{C}$	exhaust temperature upstream the point of UWS injection
T_{LF}	$^{\circ}\text{C}$	Leidenfrost temperature
$T_{\text{m,EOI}}$	$^{\circ}\text{C}$	temperature of the mixing element at the end of injection
$T_{\text{m,SOI}}$	$^{\circ}\text{C}$	temperature of the mixing element before start of injection
T_s	$^{\circ}\text{C}$	solidification temperature
t_s	s	solidification timescale
T_{sat}	$^{\circ}\text{C}$	saturation temperature
$T_{\text{urea,c}}$	$^{\circ}\text{C}$	urea crystallisation temperature
T_w	$^{\circ}\text{C}$	wall temperature
T_{wf}	$^{\circ}\text{C}$	wall film temperature
ΔT_{DL}	$^{\circ}\text{C}$	deposition limit offset temperature
Δt_{fd}	s	film dynamics evaluation period
Δt_{ff}	s	final footprint evaluation period
Δt_{HNCO}	s	HNCO concentration averaging period
Δt_{if}	ms	initial footprint evaluation period
ΔT_{LF}	s	Leidenfrost point temperature offset
ΔT_{m}	$^{\circ}\text{C}$	temperature drop between SOI and EOI
ΔT_{trans}	$^{\circ}\text{C}$	Leidenfrost transition temperature margin
u	m/s	velocity
u_d	m/s	droplet velocity
v	m/s	superficial velocity
We_d	–	droplet Weber number
We_1	–	breakup Weber number
We_2	–	breakup and splash Weber number
$X_{\text{HNCO,c}}$	PPM	critical HNCO concentration threshold
Y_{urea}	kg/kg	wall film urea mass fraction
$Y_{\text{urea,c}}$	kg/kg	critical wall film urea mass fraction

Greek Letters

α	$W/m^2 \cdot s$	heat transfer coefficient
ε	m^2/s^3	turbulent dissipation
η_d	mg/mg	deposit yield
λ_f, λ_s	$W/m \cdot K$	thermal conductivity of the fluid/solid phase
μ_t	$kg/m \cdot s$	turbulent viscosity
μ_f	$kg/m \cdot s$	dynamic viscosity of the fluid phase
ρ_f, ρ_s	kg/m^3	density of the fluid/solid phase
σ	kg/s^2	surface tension
τ	ms	characteristic timescale
ω	$1/s$	specific rate of dissipation

Chemical Compounds

Al_2O_3	aluminium oxide
$C_3N_3(OH)_3$	cyanuric acid
$C_3N_3(NH_2)(OH)_2$	ammelide
$C_3N_3(NH_2)_2(OH)$	ammeline
$C_3N_3(NH_2)_3$	melamine
$[C_3N_3(NH_2)_2]_2(NH)$	melam
$[C_6N_7(NH_2)_3]$	melem
$[C_6N_7(NH_2)(NH)]_n$	melon
$(CN)_2$	cyanogen
CO	carbon monoxide
CO ₂	carbon dioxide
HCN	hydrogen cyanide
H ₂ NCN	cyanamide
HNCO	isocyanic acid
H ₂ O	water
H ₂ O ⁺ NCO ⁻	hydronium cyanate
N ₂	nitrogen
(NH ₂) ₂ (CO)	urea
(NH ₂) ₂ (CO) ₂ (NH)	biuret
(NH ₂) ₂ (CO) ₃ (NH) ₂	triuret
NH ₃	ammonia
NH ₄ ⁺ NCO ⁻	ammonium cyanate
NO	nitrogen monoxide
NO ₂	nitrogen dioxide
N ₂ O	nitrous oxide
NO _x	nitrogen oxides

Abbreviations

6H	6-hole injector
CD	central differencing
CSTR	continuously stirred tank reactor
DDM	discrete droplet model
DEF	diesel exhaust fluid
DFT	density functional theory
DOC	diesel oxidation catalyst
DPF	diesel particulate filter
DSLR	digital single-lens reflex camera
EGR	exhaust gas recirculation
EOI	end of injection
FTIR	Fourier transform infrared spectroscopy
HC	hydrocarbons
HC	hollow cone injector
h.c.	hollow cone
HPLC	high performance liquid chromatography
inj.	injector
LES	large eddy simulation
LNT	lean NO _x trap
M1	mixer 1
M2	mixer 2
MARS	monotone advection and reconstruction scheme
MILC	mirrorless interchangeable-lens camera
PM	particulate matter
prod.	production
RANS	Reynolds averaged Navier Stokes
RM	rapid mixing
RSM	Reynolds stress model
SCR	selective catalytic reduction
SCRoF	SCR on filter
SDPF	SCR coated DPF
SI	spark ignition
SIMPLE	semi-implicit method for pressure linked equations
SMD	Sauter mean diameter
SSG	Speziale, Sarkar and Gatski
SSL	spray surface load
SST	shear stress transport
SOI	start of injection
TGA	thermogravimetric analysis
TKE	turbulent kinetic energy
UD	upwind differencing
UWS	urea water solution
wt.	weight
w.v.	water vapour content

List of Figures

1.1	Schematic overview of the major UWS preparation steps	3
2.1	Impact of temperature and injection rate on deposit formation	6
2.2	Rough classification of common doser integration schemes	8
2.3	Impact of temperature and doser integration on deposit formation	8
2.4	Exhaust flow recirculation in the injector dome of an underbody SCR system	9
2.5	Overview of typical mixing element geometries	10
2.6	Modified mixing section designs	11
2.7	Schematic overview of deposit formation mechanism hypotheses	12
2.8	Gradual wetting of the nozzle hole disc by UWS leakage after injector closing	13
2.9	TGA of urea, biuret, cyanuric acid, ammelide and ammeline	15
2.10	Simplified summary of the chemistry of deposit formation	16
2.11	TGA of urea for different sample masses and heating rates	19
2.12	TGA of urea for different crucibles and water vapour concentrations	20
2.13	Impact of droplet and spray characteristics on the Leidenfrost temperature	22
2.14	Urea water solution phase diagram	23
2.15	Review of simulation models for the decomposition of urea and its by-products	25
2.16	Review of simulation models for the prediction of deposit formation in SCR systems	27
4.1	Test bench setup underbody SCR system	32
4.2	Test bench setup close-coupled type SCR system	33
4.3	Test bench setup surrogate mixing element geometry	34
4.4	Reference mixing element, single blade elements, and optical volume	35
4.5	Reference measurements for the assessment of deposit accumulation	37
4.6	CFD domains of the underbody and close-coupled type SCR systems	39
4.7	Overview of spray characteristics	42
4.8	Schematic overview of common droplet impact regimes	44
4.9	Adapted multi-regime Bai Gosman droplet wall interaction model	45
4.10	Saturation temperature and deposition limit temperatures	46
4.11	Schematic outline of the Nukiyama pool boiling model	48
5.1	Deposit growth on the mixer of the underbody system as a function of time	49
5.2	Deposit locations in the underbody SCR system as a function of the temperature	51
5.3	Wall film preparation in primary impingement areas	52
5.4	Wall film pathways, distribution, and accumulation	53
5.5	Locations of deposit formation as a function of temperature and injection rate	54
5.6	Common deposit formation scenarios at blade edges and faces	55
5.7	Damming and peripheral deposit growth on mixer surfaces	56
5.8	Consecutive steps of deposit formation on mixer surfaces	57
5.9	Prevention of deposit formation in thick liquid films	57

5.10	Impact of edge sharpening on deposit formation at rear blade edges	58
5.11	Deposition limit and permanent wall wetting threshold as a function of temperature . .	59
5.12	Wall wetting and deposit formation on the mixer as a function of the temperature . . .	60
5.13	Critical injection rate for the onset of permanent wall wetting and deposit formation . .	61
5.14	UWS solidification timescales as a function of the temperature	63
5.15	Deposit growth as a function of the temperature	64
5.16	Thermogravimetric analyses of deposit samples and reference samples	65
6.1	Choice of areas used for the assessment of the deposit formation risk	71
6.2	Development of the total wall film mass	71
6.3	Development of the wall film temperature	72
6.4	Wall film mass during the first impingement event and urea concentration	73
6.5	Visualisation of the initial footprint	73
6.6	Visualisation of the wall film dynamics	74
6.7	Visualisation of the wall film trickling velocity	74
6.8	Visualisation of the wall film temperature	75
6.9	Development of the average isocyanic acid concentration in wetted areas	76
6.10	Visualisation of the HNCO concentration above the wall film	76
6.11	Visualisation of the deposit formation risk	78
6.12	Speed up of solid cooling as a function of the solid density	79
6.13	Validation of the deposit formation risk at $T_e = 200\text{ }^\circ\text{C}$ and $\dot{m}_{UWS} = 35\text{ mg/s}$	81
6.14	Validation of the deposit formation risk at $T_e = 240\text{ }^\circ\text{C}$ and $\dot{m}_{UWS} = 35\text{ mg/s}$	82
6.15	Validation of the deposit formation risk at $T_e = 275\text{ }^\circ\text{C}$ and $\dot{m}_{UWS} = 60\text{ mg/s}$ (M1 HC) . .	83
6.16	Validation of the deposit formation risk at $T_e = 275\text{ }^\circ\text{C}$ and $\dot{m}_{UWS} = 35\text{ mg/s}$ (M1 HC) . .	84
6.17	Validation of the deposit formation risk trends at $T_e = 275\text{ }^\circ\text{C}$ and $\dot{m}_{UWS} = 60\text{ mg/s}$. . .	85
6.18	Validation of the deposit formation risk trends at $T_e = 275\text{ }^\circ\text{C}$ and $\dot{m}_{UWS} = 35\text{ mg/s}$. . .	86
6.19	Comparison of solid cooling at $T_e = 275\text{ }^\circ\text{C}$ and $\dot{m}_{UWS} = 60\text{ mg/s}$	87

List of Tables

4.1	Operating conditions for the investigation of deposit formation in SCR systems	33
4.2	Operating conditions for the investigation of deposit formation on a mixing element . .	35
4.3	Operating conditions for the investigation of the deposition limit on a mixing element .	37
4.4	CFD domain grid sizes and SCR catalyst porosity coefficients	40
4.5	Summary of injector characteristics	42
4.6	Modelling approaches for the liquid phase properties	43
4.7	Calibration of the Bai Gosman impingement model	47
4.8	Calibration of the pool boiling model	48
5.1	Deposit mass and yield as a function of the exhaust temperature	50
5.2	Decomposition temperatures of pure reference substances	64
5.3	Formation temperatures and content of a representative set of deposits	65
5.4	Decomposition timescales of pure reference substances as a function of temperature .	67
5.5	Classification of the deposit severity	68
6.1	Calibration of thresholds for the deposit formation risk model	77

Curriculum Vitae

Henrik Smith

born 10th of December 1983 in Berlin, Germany

Academic Career

- 05/2011 - present **Vienna University of Technology, Vienna, Austria**
Institute for Powertrains and Automotive Technology
University Assistant
- 01/2011 - 04/2011 **University of Erlangen-Nuremberg, Erlangen, Germany**
Institute of Fluid Mechanics
Scientific Assistant
- 10/2004 - 12/2010 **University of Erlangen-Nuremberg, Erlangen, Germany**
Diploma in Mechatronics
- 09/1994 - 06/2003 **Deutschhaus Gymnasium, Wuerzburg, Germany**
Allgemeine Hochschulreife

Published Papers

- H. Smith, V. Schimik, K. Gabel, and T. Lauer. Evaluation and Prediction of Deposit Severity in SCR Systems. *SAE International Journal of Engines*, 9(3), 2016, doi:10.4271/2016-01-0970.
- H. Smith, M. Zöchbauer, and T. Lauer. Advanced Spray Impingement Modelling for an Improved Prediction Accuracy of the Ammonia Homogenisation in SCR Systems. *SAE Technical Paper 2015-01-1054*, 2015, doi:10.4271/2015-01-1054.
- M. Zöchbauer, H. Smith, and T. Lauer. Advanced SCR Flow Modeling with a Validated Large Eddy Simulation. *SAE Technical Paper 2015-01-1046*, 2015, doi:10.4271/2015-01-1046.
- H. Smith, M. Mayer, S. Pierson, and T. Lauer. Optical and Numerical Investigations on the Mechanisms of Deposit Formation in SCR Systems. *SAE International Journal of Fuels and Lubricants*, 7(2):525-542, 2014, doi:10.4271/2014-01-1563.
- S. Fischer, H. Smith, T. Lauer, B. Geringer, G. Pessl and C. Krenn. Impact of the Spray-Wall-Interaction-Model on the Prediction of the Ammonia Homogenization in Automotive SCR Systems. In *33rd International Vienna Motor Symposium 26-27 April 2012, Fortschritt-Berichte VDI Reihe 12 Nr. 749, Volume 2: second day*, 2012.

Presentations and Posters

H. Smith, V. Schimik, K. Gabel, and T. Lauer. Evaluation and Prediction of Deposit Severity in SCR Systems. Presentation at the *SAE 2016 World Congress & Exhibition*, 12.04.2016-14.04.2016, Detroit, Michigan, USA.

H. Smith, M. Zöchbauer, and T. Lauer. Advanced Spray Impingement Modelling for an Improved Prediction Accuracy of the Ammonia Homogenisation in SCR Systems. Presentation at the *SAE 2015 World Congress & Exhibition*, 21.04.2015-23.04.2015, Detroit, Michigan, USA.

F. Ross, H. Smith, T. Lauer, and S. Herrmann. Numerical Investigations of Deposit Formation in SCR Systems. Online webinar (invited), 31.03.2015, CD-adapco and Vienna University of Technology.

T. Lauer, H. Smith, and M. Zöchbauer. CFD-Simulation of SCR-Systems with Validated Models. Presentation at the workshop *CFD Simulation for Improving Aftertreatment Devices* (invited), 10.07.2014, Nuremberg, Germany.

T. Lauer, M. Heiß, H. Smith, and M. Zöchbauer. Application of Multi-Component Fluid Models on Pre-Ignitions and SCR-Systems. Presentation at the *STAR-CD Internal Combustion Engines Workshop* (invited), 19.06.2014, Shin-Yokohama, Japan.

H. Smith, T. Lauer, M. Mayer, and S. Pierson. Optical and Numerical Investigations on the Mechanisms of Deposit Formation in SCR Systems. Presentation at the *SAE 2014 World Congress & Exhibition*, 08.04.2014-10.04.2014, Detroit, Michigan, USA.

H. Smith, S. Pierson, and T. Lauer. Simulation of Automotive SCR Systems with STAR-CD - Evaluation of the Deposit Formation Risk. Presentation at the *STAR Global Conference 2014* (invited), 17.03.2014-19.03.2014, Vienna, Austria.

S. Fischer, H. Smith, T. Lauer, B. Geringer, G. Pessl and C. Krenn. Impact of the Spray-Wall-Interaction-Model on the Prediction of the Ammonia Homogenization in Automotive SCR Systems. Poster presentation at the *33rd International Vienna Motor Symposium*, 26.04.2012-27.04.2012, Vienna, Austria.